

Organic Photovoltaics: An Investigation of Interfacial Layers and Space-Charge Effects

A Dissertation Presented to
the Faculty of the Department of Physics
University of Houston

In Partial Fulfillment
of the Requirements for the Degree
Doctor of Philosophy

By

Xin Zhang

December, 2013

Organic Photovoltaics: An Investigation of Interfacial Layers and Space-Charge Effects

Xin Zhang

APPROVED:

Dr. Seamus Curran, Chairman

Dr. Lowell Wood

Dr. Donna Stokes

Dr. Bensaoula Abdelhak

Dr. Mark Clarke

**Dean, College of Natural Sciences and
Mathematics**

Acknowledgement

It has been a long yet interesting journey from the beginning of my graduate life to this finishing point. As the pages of this work reflects years of my research work, my name alone does not reflect the enormous contributions of everyone involved directly and indirectly to the completion of it.

Chronologically, my Ph.D. started back in the fall of 2009. After one year and half of study on the five physics core courses, my real research work began in the winter 2010 when my supervisor Prof. Seamus Curran, shook my hand and welcomed me into his lab group. Thereafter, he offered me with abundant access to equipment, courses, training as well as professional advice. He is a very reasonable advisor and gave me enough freedom in my work while at the same time guiding me in the right direction, which I cannot be more appreciative about. I give my sincere thanks to him, without his supervision I would never have completed my doctoral studies.

I also would like to express my deepest appreciation to Dr. Kang-Shyang (Shawn) Liao, who has given me many valuable pieces of advice from research work to cooking. It has been an honor to work with him and to see how delicate work is done. Dr. Nigel Alley, the Irish guy in the group who is always passionate and offers different views on things. I especially thank him for tolerating my english and his endless patience in correcting it.

Dr. Enrico Andreoli, now busy working at Rice University in transferring carbon dioxide and solving global warming, I wish him and his family every happiness in the future.

I would also like to express my best wishes to my lab mates Dr. Soniya Yambem and Dr. Amrita Haldar, I won't forget the days when we came in to the lab on weekends and worked hard together. And also thank them for the Indian dishes they taught me.

My friends and classmates Feng Chu who is always happy and cheering, I especially thank him for being the spoiler to my movies and save my watching time, and I wish him not party too hard in Iowa; Hongxing He, who helped me a lot and I would not forget his generosity; Also Lin Tang, Ivy Wang, Guoxiong Su, Bo Li, Bibi Jiang and everyone who was involved in my life here I wish them all the best!

Finally I thank my family for their understanding of my very infrequent visits home, for always being so supportive to my academic and life decisions.

Organic Photovoltaics: An Investigation of Interfacial Layers and Space-Charge Effects

An Abstract of a Dissertation

Presented to

the Faculty of the Department of Physics

University of Houston

In Partial Fulfillment

of the Requirements for the Degree

Doctor of Philosophy

By

Xin Zhang

December, 2013

Abstract

The research described in this thesis includes interface study of organic photovoltaics, and the study of the space-charge effect on organic electronics from a photonics perspective.

First, dynamic spin coating was used as a deposition technique in the fabrication of p-n bilayer organic photovoltaics, solvents used in the fabrication were carefully selected to generate different p-n interface morphologies from low level inter-digitated to flat, and it was found that the interface morphology can significantly affect the device performance.

Stability optimization was carried out by using electro-polymerized PEDOT:PSS (EPEDOT:PSS) as a replacement for the spin coated PEDOT:PSS (SPEDOT:PSS) as hole transport layer (HTL). The X-ray photoelectron spectroscopy study shows a decrease of PSS to PEDOT ratio as well as a lower Indium atomic concentration in the electro-polymerized film. The device fabricated with EPEDOT:PSS showed an appreciable improvement in the stability property.

The highly conductive PEDOT:PSS was designed to replace the Indium Tin Oxide (ITO)/PEDOT:PSS junction as the new anode to make the device fully flexible. The ITO-free device showed higher power conversion efficiency than the ITO-based device. However, the light-intensity study suggests that due to the less anode conductivity in the

ITO-free device, more space-charge effects can be observed and in turn causes a higher bimolecular recombination rate in the flexible device.

Using the flexible substrates with alternative anodes, examining their current voltage performance under different light intensity, the correlation of open circuit voltage (V_{OC}) with anode transport property was studied. A simple model on V_{OC} as a function of space charge density and photo-generated charge density was applied and successfully explained how space-charge affects the changing trend of V_{OC} .

Table of Contents

1. Introduction.....	1
1.1 An Overview in World’s Energy Consumption	1
1.2 Organic Photovoltaics	4
1.2.1 Organic Electronics	4
1.2.2 Development in OPVs.....	6
1.2.3 Challenges Associated with OPVs	7
1.3 Organization of Dissertation	9
1.4 References	12
2. Experimental Techniques.....	14
2.1 Material Detail and Preparation	14
2.1.1 Active Layer Material	14
2.1.2 Electrodes	15
2.1.3 Hole Transport Layer	16
2.2 Fabrication Equipment	19
2.2.1 Spin Processing Unit	19
2.2.2 Thermal Evaporation.....	20
2.2.3 Ozone Generator	23
2.3 Fabrication Procedure	24
2.3.1 The Substrate Cleaning	24
2.3.2 The Cleaning of ITO Substrates	24
2.3.3 The Cleaning of PEN Substrates	25
2.4 Fabrication of p-n junction Photo-generation Layer	25
2.5 Fabrication of BHJ Photo-generation Layer	26

2.6	Anode Fabrication for Flexible Devices	28
2.7	Electro-deposition of PEDOT:PSS	29
2.7.1	Theory of Electro-Deposition.....	29
2.7.2	Electro-Polymerization of PEDOT:PSS.....	30
2.8	Device Characterization	32
2.8.1	Ultraviolet Visible Spectroscopy	32
2.8.2	Atomic Force Microscopy.....	34
2.8.3	X-ray Photoelectron Spectroscopy.....	37
2.8.4	I-V Characteristic Measurement	39
2.9	References	41
3.	Theory of Conjugated Materials and Their Properties	43
3.1	Energy Band Theory of Semiconductor	43
3.1.1	Energy Band Theory	43
3.1.2	The Parabolic Band Approximation.....	45
3.1.3	Direct and Indirect Band Gap Semiconductors.....	46
3.2	Fermi Distribution and Quasi-Fermi Distribution.....	49
3.2.1	Intrinsic and Extrinsic Semiconductors.....	49
3.2.2	Density of States.....	49
3.2.3	Carrier Densities and Fermi Energy in Equilibrium	50
3.2.4	Quasi-Fermi Energy	52
3.3	Atomic and Molecular Orbitals.....	54
3.3.1	Chemical Bonds	54
3.3.2	Atomic Orbitals	55
3.3.3	Molecular Orbitals.....	56
3.3.4	Orbital Hybridization	57
3.4	Conductivity in Conjugated Polymers	60

3.5	Excitons and Optical Spectroscopic Properties of Conjugated Polymer	63
3.5.1	Quasi-particles in Organic Semiconductors	63
3.6	Photon Absorption and Emission Process.....	74
3.6.1	The Jablonski Diagram.....	74
3.7	Optical Spectrum.....	76
3.7.1	Solar Radiation and the Solar Spectrum	76
3.7.2	Black Body Radiation	76
3.8	Organic Photovoltaic Operation.....	78
3.8.1	Transport Equations in Solar Cells ³⁶	80
3.8.2	Series and Shunt Resistance in OPV Devices	83
3.8.3	Current-Voltage Characteristics	85
3.9	Characterization and Principle Parameters	88
3.10	Electron-Hole Pair Generation and Photocurrent.....	89
3.10.1	Photo-generation Rate	89
3.10.2	Carrier Generation by Thermal Excitation.....	91
3.11	Charge Recombination	92
3.11.1	Recombination Mechanisms	92
3.12	Interface and Band Alignment	96
3.12.1	Interfacial Electronic Structure inside an Organic Solid.....	96
3.12.2	Parameters Related to the Interfacial Electronic Structure	97
3.12.3	Current Flow at Junction Interfaces	98
3.12.4	Organic-Metal Interface	102
3.12.5	Organic-Organic Interface.....	106
3.12.6	p-n Junction under Forward Bias or under Illumination	110
3.12.7	p-n Junction under Reversed Bias.....	112
3.13	References	112

4. Interface Study between P3HT:PCBM and ITO/PEDOT:PSS for Organic Photovoltaics.....	116
4.1 Introduction.....	116
4.2 The Study of Donor/Acceptor Interface Morphology using P-N Junction Planerized OPVs	117
4.2.1 Background	117
4.2.2 UV-Visible Absorption Spectroscopy.....	120
4.2.3 Atomic Force Microscopy.....	123
4.2.4 Device Performance	126
4.3 Electro-polymerized PEDOT:PSS as Hole Transport Layer	128
4.3.1 PEDOT:PSS as Hole Transport Layer	128
4.3.2 J-V Characteristics of OPV devices with Buffer Layer of SPEDOT:PSS and EPEDOT:PSS	130
4.3.3 Stability Study of ITO Electrodes with EPEDOT:PSS as HTL.....	131
4.3.4 XPS study of the Spin Coated and Electro-Polymerized PEDOT:PSS on ITO	133
4.4 Conclusion.....	137
4.5 Reference.....	139
5. Investigation of Recombination Dynamics for ITO-free and ITO-based OPVs by Illumination Dependence Study.....	142
5.1 Introduction	142
5.1.1 Background	142
5.1.2 Issues Associated with using ITO-based Flexible OPV.....	143
5.1.3 The Process in Developing ITO-free Flexible OPV Devices.....	144
5.2 Recombination Mechanisms in ITO-based Standard and ITO-free Flexible device	145
5.2.1 Generation and Recombination Mechanisms in OPV.....	145
5.2.2 Light Dependence study of ITO-free Flexible Device.....	152
5.2.3 Light Dependence study of ITO-based Standard Device.....	157

5.3	Discussion of Voc Comparison in ITO-based Standard and ITO-free Flexible Device.....	160
5.3.1	Energy Shift in Vacuum Level.....	160
5.3.2	Energy Level Alignment at ITO/PEDOT:PSS/Organic Interface.....	162
5.3.3	Energy Level Alignment at P3HT:PCBM/Cathode Interface.....	164
5.3.4	Voc Comparison in ITO-based Standard and ITO-free Flexible Device	166
5.4	Conclusion.....	167
5.5	Reference.....	168
6.	Anode Conductivity Dependence Study of ITO-free Flexible OPVs under Space-Charge-Limited-Current Condition.....	171
6.1	Introduction	171
6.2	Space-Charge-Limited Current	172
6.2.1	Space charge and Space-Charge-Limited Current	172
6.2.2	Characteristics of Space-Charge-Limited Current in OPVs	175
6.3	Optical, Transport, and Electronic Properties of Modified PEDOT:PSS	176
6.3.1	UV-visible Spectra of Pristine and Modified PEDOT:PSS	176
6.3.2	Conductivity of Modified PEDOT:PSS with Different Thicknesses.	177
6.3.3	Work Function of Pristine and Modified PEDOT:PSS.....	179
6.4	Light-Intensity Study of OPVs under the Effect of Space-Charge-Limited Current.....	180
6.4.1	J-V Characteristics of the Flexible OPV Device with Different Thicknesses of Modified PEDOT:PSS Anode.....	180
6.4.2	Light-Intensity Study of the OPV Device under Short Circuit Current Condition.....	183
6.4.3	Light-Intensity Study of the OPV Devices under Open Circuit Voltage Condition.....	185
6.4.4	Light-Intensity Study of the OPV Devices for Fill Factor and Efficiency	194
6.5	Conclusion.....	195

6.6	References	197
7.	Conclusions.....	200
7.1	P3HT:PCBM Interfaces	200
7.2	Replacement and Modification of the Anode and Hole Transport Layer	201
7.2.1	Replacement with Electropolymerized PEDOT:PSS.....	201
7.2.2	Replacement with Highly Conductive PEDOT:PSS.....	202
7.3	Space-Charge effects in OPV's.....	203
7.4	References	204

1. Introduction

1.1 An Overview in World's Energy Consumption

Global demand for energy has been continuously rising over the past few decades. Since 1990, the world energy consumption has increased by 25%, and it is forecast to double within another 20 years. As can be seen in Figure 1-1 for the statistic charts released by U.S. Energy Information Administration in 2011¹, in which the slow economy recovery from the 2008 worldwide recession is responsible for the monotonic increase in the energy consumption growth in OECD (Organization for Economic Co-operation and Development) nations; while for the two non-OECD members which were among the least affected countries from the recession, China and India contribute to the largest growth in the total world energy use. By the year of 2012, together they counted for about 26.4% percent of the world total energy, surpassing United States by 49.3% and the demand is still in robust growth.

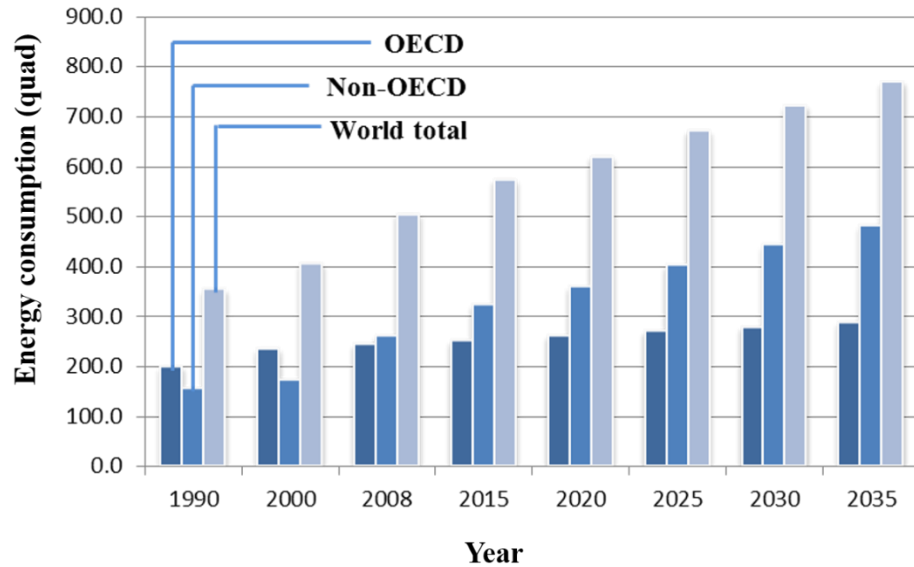


Figure 1-1. Past and projected world energy consumptions (in quadrillion btu). Diagram was drawn according to the data from U.S. Energy Information Administration, 2011¹

The energy supply by power source worldwide in 2012 on average was oil 33.1%, gas 23.9%, coal 29.9%, nuclear energy 4.5%, hydro-electricity 6.7% and all the renewable energy including biomass, solar, geothermal power and wind only takes 1.9% as shown in Figure 1-2. The traditional energy sources such as oil, gas and coal still take the dominating role in the energy market as they together account for almost 87% of all the energy consumed. This number is even higher in non-OECD countries. Developed countries, especially those in Europe, have a significant fraction of renewables in their energy supply structure, non-OECD countries still rely heavily on the fossil fuels especially coal. In China coal usage has met almost 70% of its total consumption and in India is also as high as 52.9% while in United State this value is less than 20%².

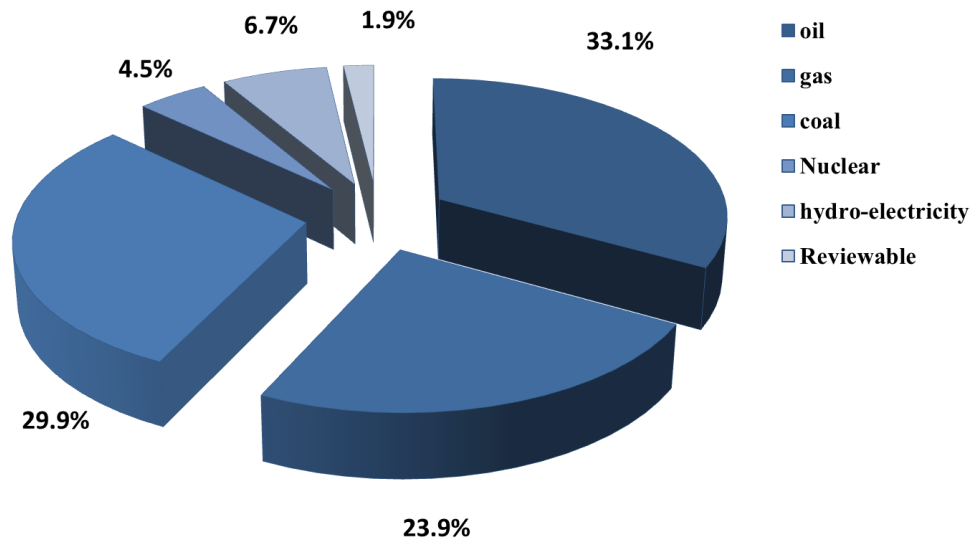


Figure 1-2. World energy consumption by source. Diagram drawn with the data released by BP company².

Along with the growing reliance on coal due to its relatively cheap price compared to the other fossil fuels, environmental pollution now is becoming the largest issue. The Kyoto Protocol to the United Nations Framework Convention on Climate Change adopted in 1997 has set a binding limitation in the carbon dioxide emission operated with legal force. Although it is signed by 191 states, the regulation only sets binding targets for developed countries in their commitment period, while developing countries are still allowed to have emission growth in accordance with their development needs. Moreover, as the biggest carbon dioxide contributor, United States has not ratified the Protocol. The long term effectiveness of the Kyoto Protocol is debatable.

Given expectations that the world oil prices will remain relatively high in the near future, it has been realized by many countries that the renewable energy will become an excellent alternative for energy supply. In United States, the fiscal year 2014 budget plan released on April 2013 established the goal of increasing clean technology investments by 40% over current levels to \$6.2 billion while cutting oil imports in half by 2020 relative to 2008 levels. In India, a target of adding about 30,000 MW from various renewable energy sources was fixed for the 12th Plan period from 2012 to 2017 in December 2012 and it still remains on track. In 2012, \$65 billion were plowed into Chinese wind farms, solar panel arrays, and other clean energy projects, making it the world's top destination for green energy investments, which in total has reached \$269 billion for the year spending worldwide³. The emerging market in renewable energy will make it the fastest growing energy in the near future.

1.2 Organic Photovoltaics

1.2.1 Organic Electronics

Organic electronics based on organic materials are realized by the application of organic conductors or conjugated polymers. The π -conjugation – a system with alternating single and double bond which allows for a high atomic orbital overlapping and delocalization of the charges on the molecule, is the reason for the charge transport property in the carbon based organic conducting material. In contrast to the traditional inorganic conductors such as copper or silicon, conjugated organic materials are lighter, more flexible, and less

expensive, which enable them to act as an desirable alternative in many applications that cannot be accomplished by inorganic materials.

The unique properties of organic conductive material were studied by Henry Letherby as early as 1862. The aniline in sulfuric acid showed a partly conductive property after being anodic oxidized. Later the pace of development in conducting organic material gathered momentum after polycyclic aromatic compounds formed with halogens were found to have charge transfer ability⁴. A breakthrough was made by Heeger et al.⁵ in 1977, they modified the polyacetylene from insulating to high conducting by doping with halogen. The electrical conductivities of the conducting polymer today can range from that typical of insulators (less than 1 S/cm) to almost that of a good metal (10^4 S/cm). Some common used conjugated polymers are polyacetylene, polyphenylene, polypyrrole, polythiophene and polyaniline. Their conductivities are shown in Figure 1-3.

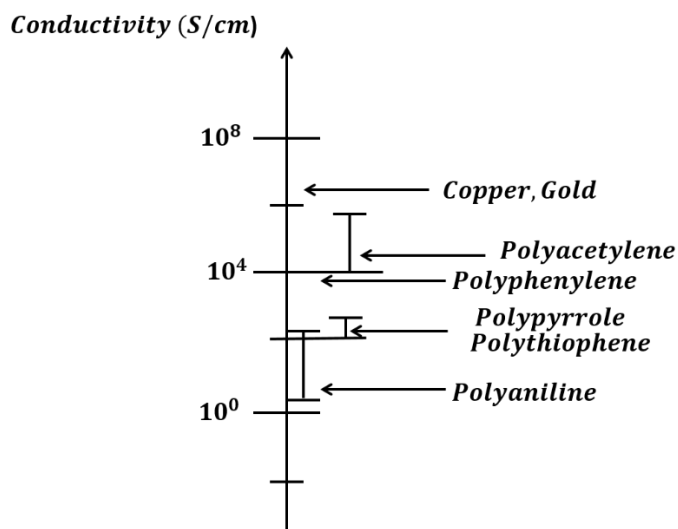


Figure 1-3. Electric conductivity for some typical conjugated polymers. Diagram redrawn from Ref. 6⁶.

The application of organic material as a semiconductor into electronics started to emerge after the development of organic light emitting diodes (OLEDs), using small molecules of 8-hydroxyquinoline aluminum (Alq_3) in 1987 by Tang et al.⁷ The organic material played the role of organic semiconductor in their work. The fast pace of the success in the electroluminescent devices also stimulated the development of other organic electronics. Today there are mainly three divisions in field of organic electronics: OLEDs, organic field effect transistors (OFETs) and organic photovoltaics (OPVs). Among which OLEDs is by far the most advanced developed in the field of organic electronics with many of its devices be launched into the market, while OPVs still has a long way to go in catching up with the inorganic photovoltaics (IPVs) counterparts.

1.2.2 Development in OPVs

OPV is a very exciting field of renewable energy source and has been a field of pronounced growth ever since the photovoltaic effect was observed in the phthalocyanine based single junction solar cell in 1958⁸. Although the power efficiencies of OPVs are still lagging behind of IPVs, which already has industrialized products with efficiencies normally ~17%, the advantages of organic semiconductors, such as their being lightweight, their solution processable fabrication, material flexibility and low cost have been the strong driving force that makes OPVs a very attractive market for investment.

The development of OPVs has been through three stages distinguished by the device structures. In the earliest stage after 1958, devices with efficiencies far below 1% were fabricated with a single but thick layer of polymer semiconductor inserting between two electrodes. The photoactive layer was usually several hundred nanometers' thickness and

the efficiency was very low. The second stage began when the first successful photoactive organic device was made with an efficiency of 1% by Tang in 1986⁹ with a p-n junction structure, the bilayer device was consisted of two contacting organic semiconductor, referred as a donor and an acceptor. The discovery of C₆₀ in 1985¹⁰ also made a boost in the OPVs development. The high electron affinity and fast electron transfer of C₆₀ have made it a good electron acceptor in photovoltaic cells. Sariciftci et al.¹¹ fabricated a bilayer device based on C₆₀ and poly(2-methoxy-5-(2-ethylhexyloxy)-1,4-phenylenevinylene) (MEH-PPV) and achieved the device with a high fill factor of 0.48 and a power conversion efficiency of 0.04% under monochromatic illumination.

The major breakthrough in this field was made when the concept of bulk-heterojunction (BHJ) was introduced, which is still heavily used till today. In 1995 Yu et al.¹² fabricated a cell with the blend of MEH-PPV and C₆₀ which yielded a power conversion efficiency of 2.9% under monochromatic illumination. Later, new polymer materials were developed and poly (3-hexylthiophene-2,5-diyl) (P3HT) replaced the once widely used MEH-PPV as a new donor material. In 2005, a high efficiency of 5.2 % was fabricated using P3HT as donor and a C₆₀ derivative phenyl-C61-butyric acid methyl ester (PCBM)¹³ as acceptor material. Nowadays, with the new improved materials and device structures as tandem cells, OPV device with efficiencies as high as 8.3% was reported¹⁴.

1.2.3 Challenges Associated with OPVs

Despite the attractive properties of organic semiconductor, OPV still has some challenges to overcome. In photovoltaic field, the ability to precisely engineer each layer of the OPV

device is of paramount importance to achieve high efficiencies. However, due to a late start up of the development when traditional silicon solar cell already reported device with 6% efficiency¹⁵, the OPV research is immature in many aspects. For an idealized device, the materials need to be chosen so that the electronic, transport and optical properties are closely matched to each other. This has to be carefully managed for the performance to be optimum.

The most widely used and studied OPV material combination is P3HT/PCBM, the P3HT layer has an absorption peak at around 550 nm¹⁶ and which matches very well with the solar spectrum, and the PCBM is a very fast electron transfer acceptor material. Nevertheless, for the device modification, a trade-off between the absorption efficiency with exciton separation efficiency needs to be made. The short exciton diffusion length (~10 nm)¹⁷ and low charge mobility in P3HT have confined the thickness of the solar cell to be ultra-thin (<100 nm); however, a thin layer will result in a low absorption efficiency; Therefore, for a typical standard P3HT/PCBM OPVs device, the absorption efficiency remains as low as ~ 20%¹⁸, compared with an amorphous silicon solar cell of 50%¹⁹.

Another trade-off for the short exciton diffusion length of P3HT is made with charge collection efficiency. The widely used BHJ structure for OPVs devices is an excellent structure because the blending nature can create enough donor/acceptor interfaces where excitons can diffuse to and separate into charge carriers before recombine to ground states; conversely, this mixing structure prevents the formation of a consistent percolation

pathway for the charge carriers traveling from the generation site to electrodes which in turn decreases the charge collection efficiency. The internal quantum efficiency is usually less than 50%²⁰, which is again much lower than the value for IPVs of ~ 80%²¹. In this view the p-n junction structure will be a better structure to be built on compared with BHJ, efforts then can be simply devoted to either increase the excitation diffusion length or the interface contacting area.

The replacement of indium tin oxide (ITO) electrodes is another challenge to be confronted. ITO is the most common transparent conductive material which has been widely used in flat panel industry. But the ITO substrate is very brittle and fragile, and this prevents the OPVs to be fabricated into flexible shapes. In addition, ITO is unstable under acid environment. The indium and tin ions migrate into the surrounding organic layers and impair the OPVs device performance. There is a huge amount of work being done to find an ideal replacement electrode for ITO

1.3 Organization of Dissertation

The subsequent chapters are devoted to the study of device structure and dynamics of OPVs. They are structured in the following way:

Chapter 2: Experimental Section

This chapter is concerned with the experimental apparatus associated with the thesis work. All the materials used are detailed and the device fabrication and characterization processes are described. Apparatus used in these processes are presented with in depth

schematic diagrams showing their working mechanism. The detailed device fabrication methods as well as pre-treatment or post-treatment are illustrated step by step.

Chapter 3: Theoretical Background

This chapter involves the main chemical and physical theory background for OPVs. It is divided into five small sections, sequentially talking about forming of the conjugating system and the energy level in the materials; the quasi-particles along with its optical absorptions, the basics equations and parameters associated with OPVs, the generation and recombination mechanisms within the device and the interfaces between layers.

Chapter 4: Interfaces in OPVs

This chapter is divided into two different small sections. The first half deals with the donor/acceptor interface correlated with device performance in the photoactive layer adopting a bilayer structure. Modifications in interface morphology to the p-n junction OPV devices are detailed. The correlation between the results from characterization techniques (Ultraviolet visible spectroscopy, atomic force microscopy) and the device performances are discussed at the end of the section.

The second half of this chapter is focused on the anode/hole transport layer interface in the anode junction of the OPVs device. The comparison between OPV device performance using electro-polymerized and spin coated PEDOT:PSS as HTL is presented. Degradation study of OPVs device with electro-polymerized PEDOT:PSS compared with reported results for devices with spin coated poly(3,4-ethylenedioxythiophene)-poly(styrenesulfonate) (PEDOT:PSS) is discussed. Finally, the

X-ray photoelectron spectroscopy for the study of etching effects within these two types of anode junction is discussed in correlation with the device degradation study.

Chapter 5: Investigation of Recombination Dynamics for ITO-free and ITO-based OPVs by Illumination Study

The common issues associated with ITO and flexible OPV devices using inorganic anodes are presented. The replacement of ITO with highly conductive PEDOT:PSS for a fully flexible OPV device is shown to be viable. Light dependence study for recombination mechanism in both ITO-free flexible and ITO-based standard device is individually discussed. At the end of the chapter, a discussion about reported interface band alignment between some common used materials and an analysis about open circuit voltage difference between the two devices are given.

Chapter 6: Anode Conductivity Dependence study of ITO-free flexible OPVs under Space-Charge-Limited Current Condition

The optical, transport and electronic properties of two highly conductive PEDOT:PSS films with different thicknesses deposited on Polyethylene naphthalate (PEN) are presented in the beginning of the chapter. The light-intensity responses of these two devices are shown to be different. Fittings of the principle parameters as a function of light intensity are presented and used to explain the anode conductivity dependence of the device performance under the condition of space-charge-limited current.

Chapter 7: Conclusions

In this chapter a brief summary and overview of the thesis work is presented. Future work and directions are also discussed.

1.4 References

- 1 <http://www.eia.gov/forecasts/ieo/world.cfm>.
- 2 <http://www.bp.com/en/global/corporate/about-bp/statistical-review-of-world-energy-2013.html>.
- 3 <http://money.cnn.com/2013/04/17/news/economy/china-green-energy/index.html>.
- 4 H. Naarmann, in *Ullmann's Encyclopedia of Industrial Chemistry* (Wiley-VCH Verlag GmbH & Co. KGaA, 2000).
- 5 A. J. Heeger, *The Journal of Physical Chemistry B* **105**, 8475 (2001).
- 6 H. S. Nalwa, *Advanced Functional Molecules and Polymers* (Gordon and Breach Science Publishers, 2001).
- 7 C. W. Tang and S. A. VanSlyke, *Applied Physics Letters* **51**, 913 (1987).
- 8 D. Kearns and M. Calvin, *The Journal of Chemical Physics* **29**, 950 (1958).
- 9 C. W. Tang, *Applied Physics Letters* **48**, 183 (1986).
- 10 H. W. Kroto, A. W. Allaf, and S. P. Balm, *Chemical Reviews* **91**, 1213 (1991).
- 11 N. S. Sariciftci, L. Smilowitz, A. J. Heeger, and F. Wudl, *Science* **258**, 1474 (1992).
- 12 G. Yu, J. Gao, J. C. Hummelen, F. Wudl, and A. J. Heeger, *Science* **270**, 1789 (1995).
- 13 M. Reyes-Reyes, K. Kim, J. Dewald, R. López-Sandoval, A. Avadhanula, S. Curran, and D. L. Carroll, *Organic Letters* **7**, 5749 (2005).
- 14 <http://www.businesswire.com/news/home/20101129005301/en/Konarka%E2%80%99s-Power-Plastic-Achieves-World-Record-8.3>.

- 15 K. A. Tsokos, *Physics for the Ib Diploma* (Cambridge University Press, 2008).
- 16 T.-A. Chen, X. Wu, and R. D. Rieke, *J. Am. Chem. Soc.* **117**, 233 (1995).
- 17 P. E. Shaw, A. Ruseckas, and I. D. W. Samuel, *Advanced Materials* **20**, 3516
(2008).
- 18 G. Chidichimo and L. Filippelli, *International Journal of Photoenergy* **2010**
(2010).
- 19 M. Solano, M. Faryad, A. S. Hall, T. E. Mallouk, P. B. Monk, and A. Lakhtakia,
Appl. Opt. **52**, 966 (2013).
- 20 J. Piris, T. E. Dykstra, A. A. Bakulin, P. H. M. v. Loosdrecht, W. Knulst, M. T.
Trinh, J. M. Schins, and L. D. A. Siebbeles, *The Journal of Physical Chemistry C*
113, 14500 (2009).
- 21 K.-H. Yang and J.-Y. Yang, *Solar Energy* **85**, 419 (2011).

2. Experimental Techniques

2.1 Material Detail and Preparation

2.1.1 Active Layer Material

P-type conjugated polymer

The main P-type material used in this dissertation is Poly(3-hexylthiophene-2,5-diyl), (P3HT) (98 % regioregular), purchased from Sigma-Aldrich. It has an average molecular weight $\sim 87,000$ and the highest occupied molecular orbit (HOMO) and lowest unoccupied molecular orbit (LUMO) level are ~ 5.0 eV and ~ 3.0 eV, respectively. Different concentrations of P3HT are dissolved in chlorobenzene and stirred at 300 rpm on a 55 °C hot plate for 24 h before use.

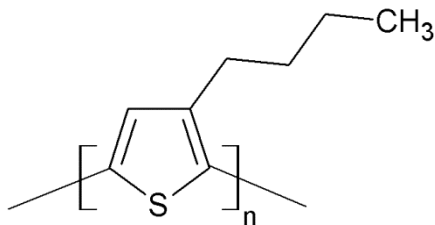


Figure 2-1. Structure of P3HT.

N-type conjugated polymer

The N-type material used in this dissertation is a functionalized fullerene 1-(3-methoxycarbonyl) propyl-1-phenyl-[6,6]-methanofullerene (PCBM) (>99%), purchased

from Sigma-Aldrich. It has a HOMO level of 6.1 eV and LUMO level of 3.7 eV. The P3HT:PCBM ratio used for the preparation of photoactive layer was 1:0.66 in this dissertation.

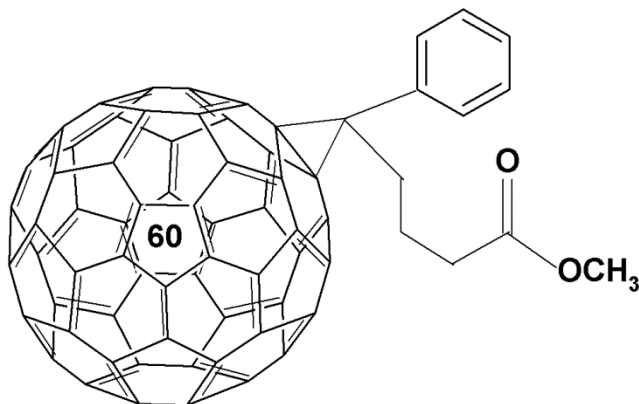


Figure 2-2. Structure of PCBM.

2.1.2 Electrodes

Indium Tin Oxide

The anode substrate used in the standard device is indium tin oxide (ITO) sourced from Sigma-Aldrich in the form of coated glass slides. The sheet resistance for the ITO slides is 8 – 12 $\Omega/square$ and the optical transparency at 500 nm is around 85 %.

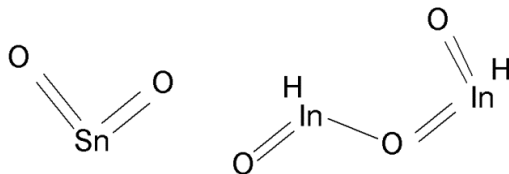


Figure 2-3. Chemical structure of Indium tin oxide. Diagram redrawn from Ref. 1¹

Highly Conductive PEDOT:PSS

A highly conductive polymer anode is prepared by adding 5% dimethyl sulfoxide (DMSO) to the Poly(3,4-ethylenedioxythiophene)-poly(styrenesulfonate) (PEDOT:PSS) solution. It is stirred for 3 hours before use.

Aluminum

Aluminum (Al) is widely used as the cathode electrode in the photovoltaic field due to its moderately low work function of ~ 4.2 eV. In this dissertation, Al is used exclusively throughout this work as the cathode material for the organic photovoltaic (OPV) devices. It is deposited by thermal evaporation at low pressures $\sim 10^{-6}$ mbar.

2.1.3 Hole Transport Layer

PEDOT:PSS

The hole transport layer (HTL) used for the standard device referred to in this dissertation is PEDOT:PSS. There are mainly two kinds of methods for the HTL deposition. For spin coating the aqueous PEDOT:PSS solution is used as purchased from Sigma-Aldrich, under the name of Clevios PH1000. It has a weight concentration of 1.2% and conductivity 1.0 S/cm.

Poly(sodium *r*-styrene sulfonate) ($M_w \sim 70,000$)

The electrolyte PSSNa used in the electro-deposition of PEDOT:PSS has a molecular weight $\sim 70,000$, and is purchased from Sigma-Aldrich.

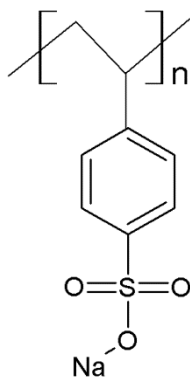


Figure 2-6. Structure of PSSNa.

EDOT

The monomer EDOT used in the electro-polymerization of the PEDOT:PSS anode film is purchased from Sigma-Aldrich with a purity of 97 %.

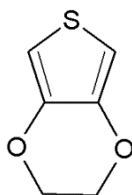


Figure 2-7. Structure of EDOT monomer.

2.2 Fabrication Equipment

2.2.1 Spin Processing Unit

Spin coating is a method used to deposit uniform thin films onto flat substrates. It is a low cost, solution processing procedure and is widely used in micro-fabrication techniques. This deposition method has importance use in photolithography where very thin films of photoresist about 1 μm thick has to be deposited on to silicon wafers³. A certain amount of solution is deposited onto the substrate, which is then rotated at a high spin speed to radially spread the fluid by centrifugal forces. In this deposition technique, it is possible to achieve layers as thin as tens of nanometers with relative ease. The thickness of the film is basically controlled by the spin speed: generally the higher the angular speed of the spinner, the thinner the deposited layer will be. The solvent used for spin coating is usually volatile and will evaporate during processing. Thus, boiling point of the solvent will be another parameter that affects the film thickness in spin coating.

There are mainly two ways to apply the spin coating technique. In static spin coating, a certain amount of solution is deposited onto the substrate before the spin starts. In contrast, in dynamic spin coating, the solution is dispersed on the top of the substrate while the substrate is being spun around.

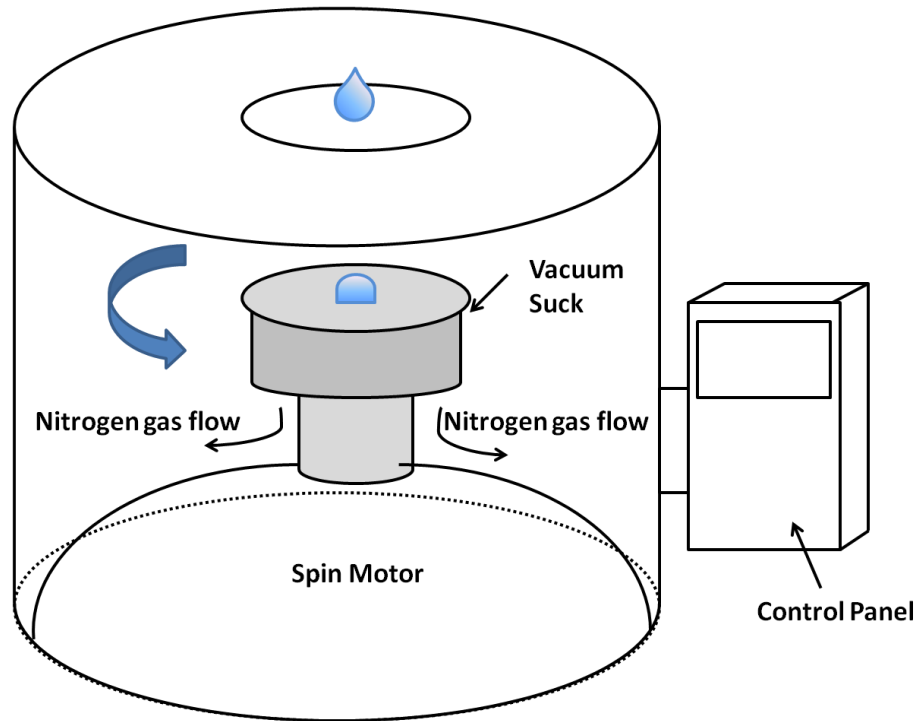


Figure 2-8. Diagram of a spin processing unit.

The spin coater used in the lab is a Laurell WS-650-8 spin coater as is shown in Figure 2-8. It has a deposition chamber, where an inert environment can be achieved by connecting the chamber with a nitrogen supply during deposition. The chamber can accommodate up to 200 mm and 7" by 7" sample substrates. A vacuum pump is connected with the sample holder to help keep the sample in place during high spin speed. The spin coater features a spin speed range from 0 to 12,000 rpm and can be set on the control panel along with other parameters, such as acceleration rate and spin time.

2.2.2 Thermal Evaporation

Thermal evaporation is a deposition process which can provide uniform films with thickness ranging from a few nanometers to several microns. The metal electrodes such

as gold (Au), silver (Ag) and chromium (Cr) are capable of being deposited on to the substrates through thermal evaporation. Figure 2-9 and Figure 2-10 shows the schematics of a custom built thermal evaporator used in our lab. It is mainly composed of an evaporation chamber, a pumping unit and a controlled current source.

The evaporation chamber is where the thermal evaporation process takes place (Figure 2-9). It has a sample stage for mounting the sample holder, with each sample placed symmetrically with respect to the evaporation center to make sure the film formation is consistent under the same parameters, such as thickness and evaporation speed. The shutter is placed above the evaporation center in the early stage of the evaporation to avoid the impurity particles from deposited on to the sample; it can be shifted to the side freely once the deposition begins through an electrical powered motor from outside. The desired metal ingot is put in a tungsten filament boat at the evaporation center. Two copper bars holding the tungsten are connected to a current feeding source (ZUP20-40 – TDK lambda) outside reaching up to 40 A. At high currents, the evaporation basket can reach temperatures as high as 1800 °C by resistive heating, and this process melts the metal ingot inside and realizes the evaporation. By increasing current in controlled manner, the evaporation can be controlled with a proper evaporation rate and thickness of the film. Once the evaporation is done, the deposition chamber is vented with nitrogen to prevent the sample from exposed to ambient environment and degraded. The evaporation is usually operated with pressure lower than 10^{-5} mbar.

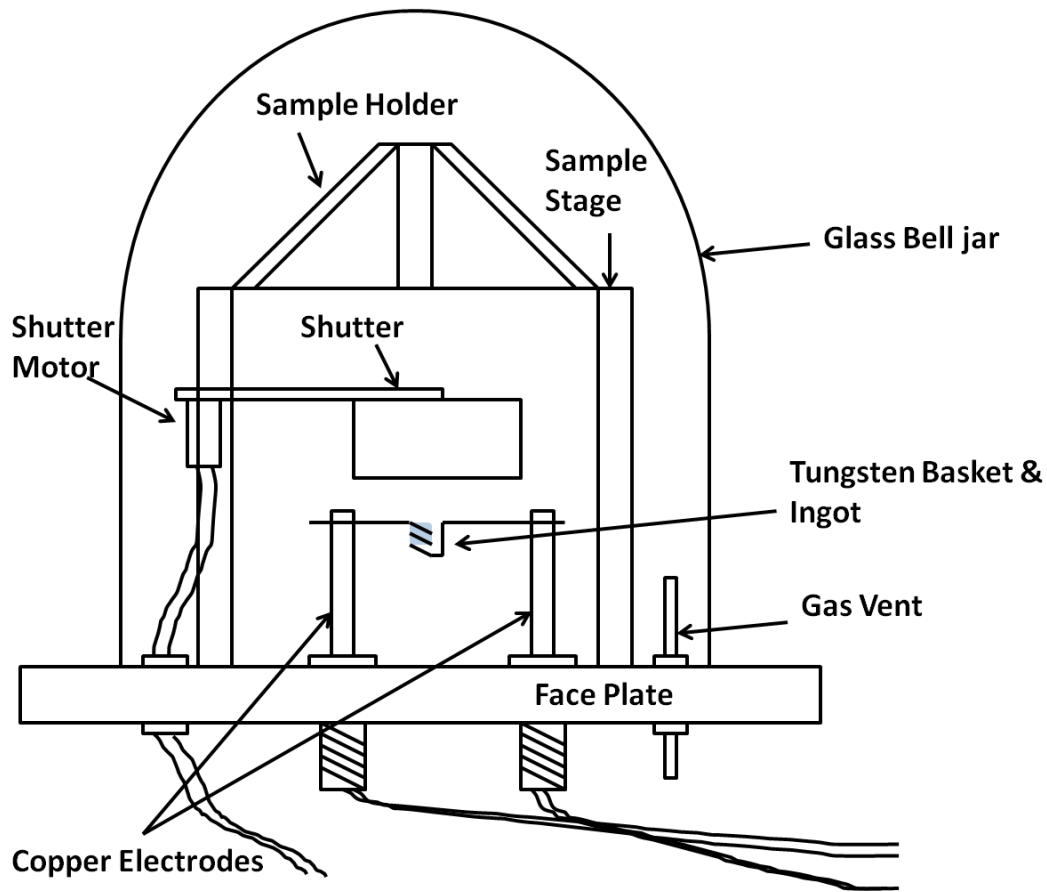


Figure 2-9. Custom built thermal evaporator system - bell jar configuration diagram.

The pumping unit is a combined roughing pump system (HiCube 80 Eco –Pfeiffer Vacuum) and turbo-molecular system with a spin frequency up to 1500 Hz (Figure 2-10). A 48-h run time can get the pressure in the evaporation system to as low as 10^{-6} mbar. A gate valve is built in line to control the connection status between the evaporation chamber and the pump, when the evaporation is finished, the valve is closed to let the nitrogen get into the evaporation chamber and release the glass bell jar. The gate valve can sustain up to a 10^{-4} times difference in pressure.

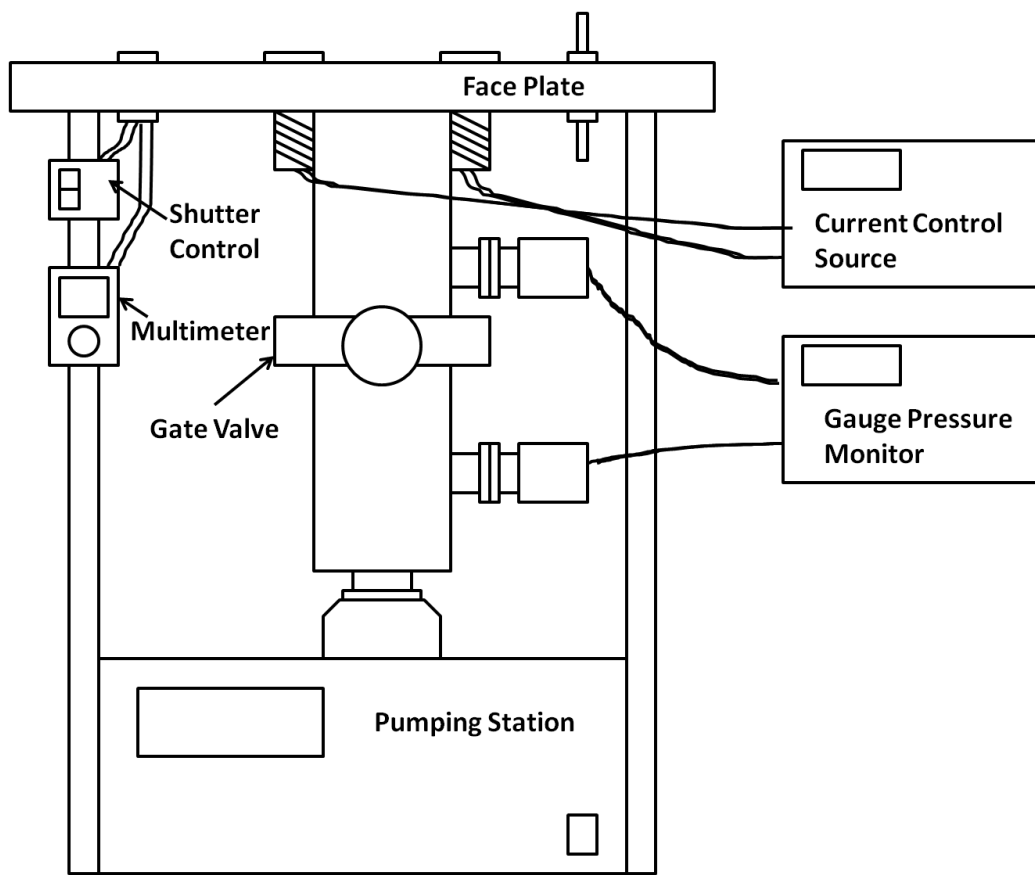


Figure 2-10. Diagram of the evaporation system components below the bell jar.

2.2.3 Ozone Generator

The Ultraviolet (UV)-O₃ treatment apparatus used in the experiment is Novascan PSD (Figure 2-11). In the UV ozone process, the UV light ionizes the oxygen in the ambient air and creates ozone, which then reacts with water in the air and generates hydroxyl radicals. The reacting process is shown in the chemical equations below. The double bond in the ITO is susceptible to the hydroxyl radicals and will help to form a hydrophilic surface for the PEDOT:PSS layer to adhere to.

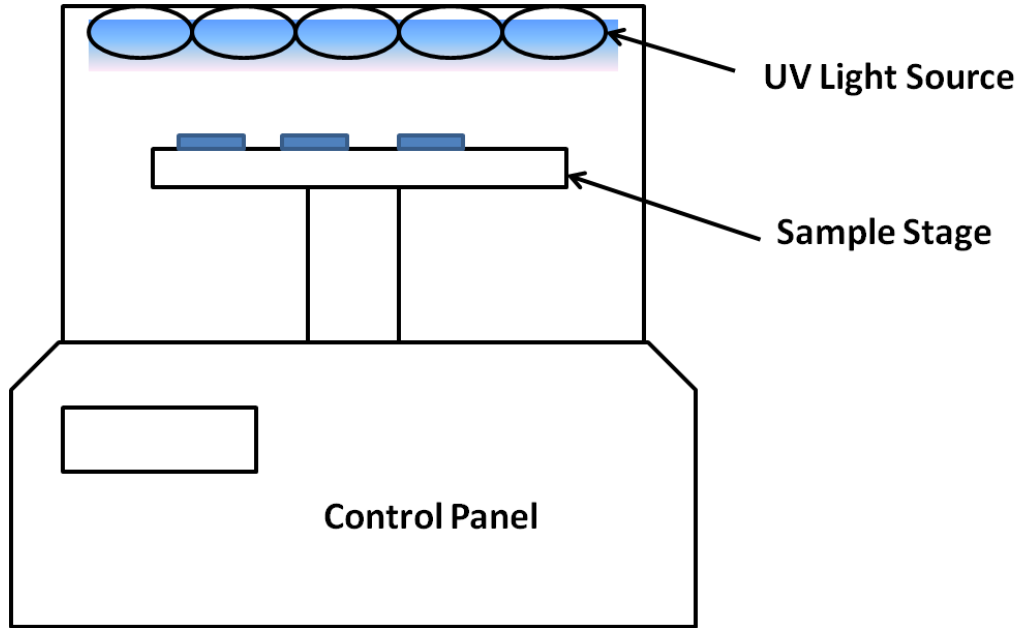
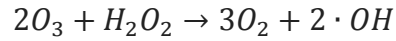
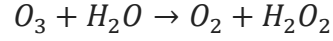


Figure 2-11. Diagram of the Novascan PSD ozone treatment system.

2.3 Fabrication Procedure

2.3.1 The Substrate Cleaning

2.3.2 The Cleaning of ITO Substrates

The pristine ITO substrate used for the device was first partially protected from etching using scotch tape. The exposed ITO was then dusted with Zinc powder and etched away using an 18 % hydrogen chloride (HCl) (aq) for 10 seconds. The patterned slides were

then rinsed with excess water and sonicated sequentially with 1.5 % Micro-90, de-ionized water ($\times 2$) and isopropanol each for 15 minutes at 60 °C. After drying with nitrogen, the ITO substrates were treated with ozone plasma for 10 minutes before the deposition of PEDOT:PSS.

2.3.3 The Cleaning of PEN Substrates

The flexible substrates Polyethylene Naphthalate (PEN) were first cut into desired shapes of 75 mm \times 25 mm and then soaked in isopropanol for 30 minutes to dissolve all the organic residues on the films. They were then sonicated sequentially in 1.5% Micro-90, de-ionized water ($\times 2$) and isopropanol each for 15 minutes at 60 °C. After drying with nitrogen, the PEN substrates were treated with ozone plasma for 30 minutes before the deposition of modified PEDOT:PSS. The longer ozone treating time for PEN substrates result in a more uniform organic layer.

2.4 Fabrication of p-n junction Photo-generation Layer

The p-n junction OPVs in the dissertation have a structure of ITO/PEDOT:PSS/P3HT/PCBM/Al. The PEDOT:PSS (Clevios PH-1000, H. C. Starck) layer was spin-coated at 3000 rpm. All substrates were then dried in an 80 °C oven for 1 hour before the P3HT (in anhydrous chlorobenzene, Aldrich) layer and PCBM (5g/L, PCBM in dichloromethane, chloroform and chlorobenzene respectively, Aldrich) layer were subsequently deposited on the substrates. The P3HT solution was spin coated onto the substrates with a spin speed of 1500 rpm while the PCBM layer was dynamically deposited by applying a small drop of solution on top of the P3HT layer under a high spin

speed (6000 rpm). After the coating of each layer, the slides were first solvent annealed for 20 minutes then dried in an 80 °C oven for 30 minutes. The procedure for the fabrication of the other layers will be the same as in the ITO standard device. Figure 2-12 shows a schematic diagram for the geometry of the p-n junction OPVs device.

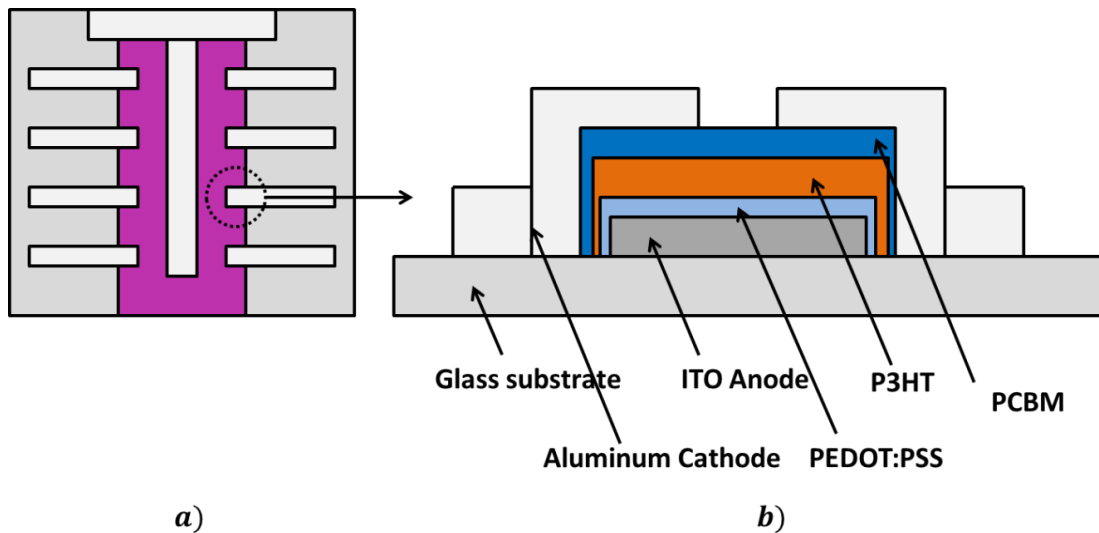


Figure 2-12. Schematic diagram of a p-n junction OPV device. a) Front view of the distribution of the devices on the substrates; b) intersection view of different layers in the ITO standard OPV.

2.5 Fabrication of BHJ Photo-generation Layer

The ITO standard device referred to this dissertation has a bulk-heterojunction (BHJ) structure of ITO/PEDOT:PSS/P3HT:PCBM/Al with a cell area $\sim 1 \text{ mm}^2$. The fabrication process for the ITO standard device is the same as that for the p-n junction OPV, except the way photoactive layer is deposited. In the ITO standard device, the photoactive layer

was spin coated with a spin speed of 1500 rpm using the bulk solution containing both P3HT:PCBM (1:0.66) instead of deposited separately. The films were solvent annealed for 20 minutes under a saturated chlorobenzene vapor environment and dried in an 80 °C oven for 30 minutes. Patterned Al electrodes were thermally evaporated (at a pressure $\sim 8 \times 10^{-6}$ mbar) on top of the PCBM layers using a custom made shadow mask. All devices were encapsulated with glass slides using a UV curable resin under a nitrogen atmosphere (less than 20% relative humidity) before characterization. Figure 2-13 shows a schematic diagram for the geometry of the ITO standard device.

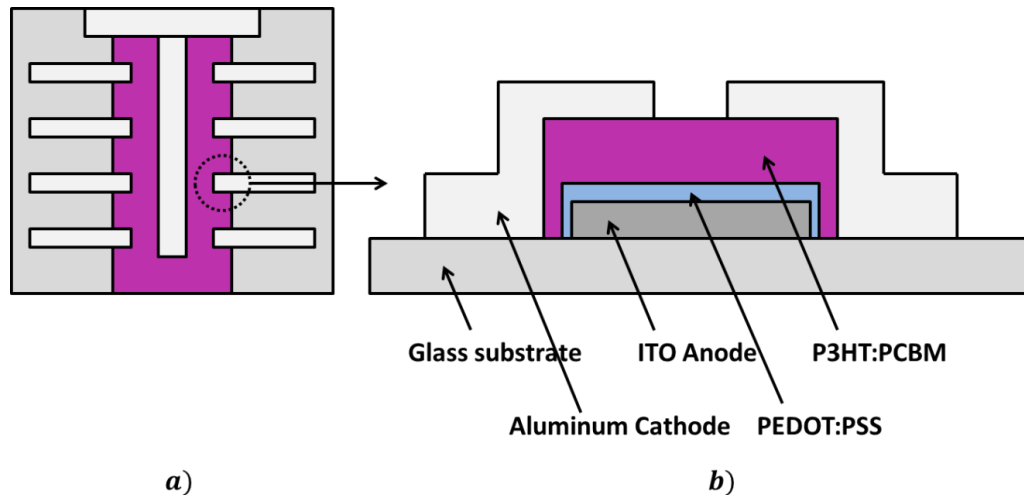


Figure 2-13. Schematic diagram of an ITO standard OPV device with a bulk heterojunction photo-generation layer. a) Front view of the distribution of the devices on the substrates; b) intersection view of different layers in the ITO standard OPV.

2.6 Anode Fabrication for Flexible Devices

The flexible OPV referred to in this dissertation has a structure of PEN substrate/modified PEDOT:PSS/P3HT:PCBM/Al. The highly conductive PEDOT:PSS formulation was prepared by adding 5% (v/v) DMSO into the aqueous PEDOT:PSS dispersion. After being stirred at room temperature for 3 hours, it was then filtered through a 0.20 μm polyethersulfone (PES) membrane and spin coated onto the pretreated PEN films. The PEDOT:PSS films were immediately annealed on a hotplate at 120 $^{\circ}\text{C}$ for 5 minutes in ambient atmosphere and then dried at an 80 $^{\circ}\text{C}$ oven for 30 minutes. The procedure for the fabrication of the other layers will be the same as in the ITO standard device. Figure 2-14 shows a schematic diagram for the geometry of the p-n junction OPVs device.

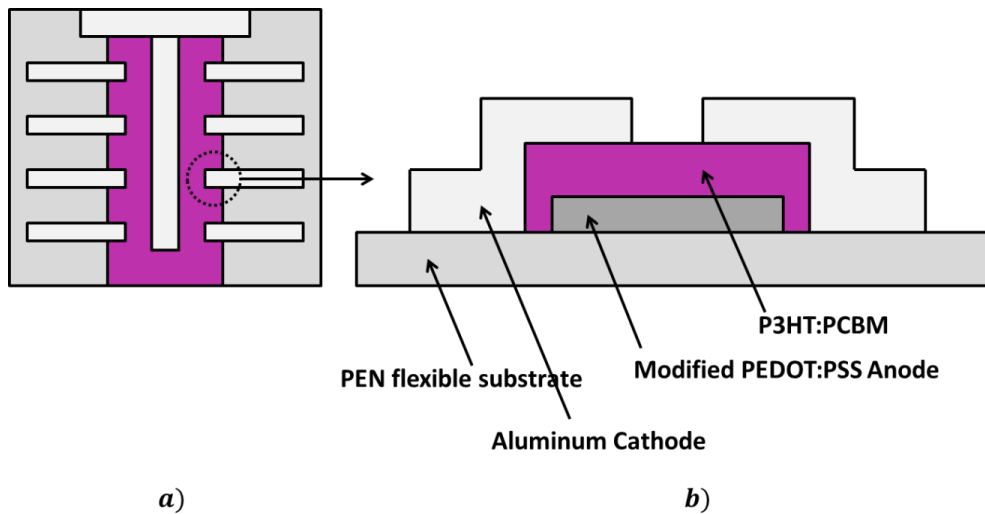


Figure 2-14. Schematic diagram of a flexible device with modified PEDOT:PSS as anode. a) Front view of the distribution of the devices on the substrates; b) intersection view of different layers in the device.

2.7 Electro-deposition of PEDOT:PSS

2.7.1 Theory of Electro-Deposition

Electro-polymerization is a branch of electro-chemistry where the chemical reaction takes place in the conducting electrolyte at the interface of two electrodes. As seen in Figure 2-15, the anode electrode undergoes oxidation reaction and the electrons travel from anode through the external circuit to the cathode causing reduction at the electrode. In the internal circuit, the electrons transfer in the opposite direction from cathode to anode. The electrochemical cell voltage between the anode and the cathode is referred to as the electromotive force or *emf*, and it is equal to the difference in the reduction potential of the two electrodes as⁴

$$emf = E_{red}(cathode) - E_{red}(anode) \quad (2.7.1)$$

While the reduction/oxidation potential of each electrode is affected by numerous factors such as temperature, pressure, and reactant concentrations, which can be expressed using the Nernst equation as⁴

$$E_{red} = E_{red}^{\ominus} - \frac{RT}{zF} \ln Q \quad (2.7.2)$$

where E_{red}^{\ominus} is the standard reduction potential, R is the universal gas constant, T is temperature, F is the Faraday constant, and Q is the reaction quotient that is expressed as the ratio of the reductant over oxidant chemical activity. The standard electrode potential is calculated by setting the standard hydrogen electrode as 0. The other standard electrode

potentials are thus calculated depending on the relative value to this standard hydrogen electrode. The oxidation potential of a particular electrode is just the negative of the reduction potential. When two electrodes are put together to form an electro-deposition system, the one that has a smaller oxidation potential will be the anode and the undergo oxidation while the other side will be the cathode and undergo reduction.

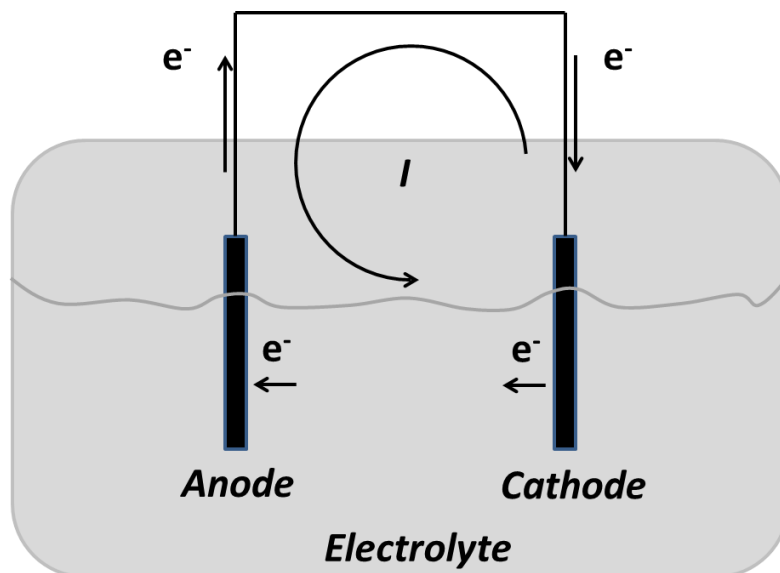


Figure 2-15. Schematic drawing of an electro-deposition system.

2.7.2 Electro-Polymerization of PEDOT:PSS

The electro-polymerization of PEDOT:PSS is achieved using a Keithley 2400 source meter in 4 wire remote sensing mode, The HI/LO (input/output) of the Keithley 2400 source meter are connected to the working and counter electrodes, respectively; and the HI/LO (4wire sense) are connected to the working and reference electrodes, respectively, as shown in Figure 2-16. The reference electrode used in the experiment is Ag/AgCl

BASI m2-2021, the counter electrode is a platinum disk. The voltage recorded by the source meter will thus be the potential difference between the working electrode and the reference electrode with a constant potential.

After the pretreatment of ITO slides, they will be used as the working electrode for the electro-polymerization of PEDOT with PSS (electrolyte is a 0.1 M EDOT/100 mM PSS solution, filtered with Corning PES 0.20 μ m before use). The thicknesses of the electro-polymerized films are controlled by changing the applied currents and the time of electro-deposition. After the fabrication, the films are rinsed with enough amount of ASTM (American Society for Testing and Materials) type purified water to wash away the excess electrolyte before dried in air at 80 °C for 1 hour.

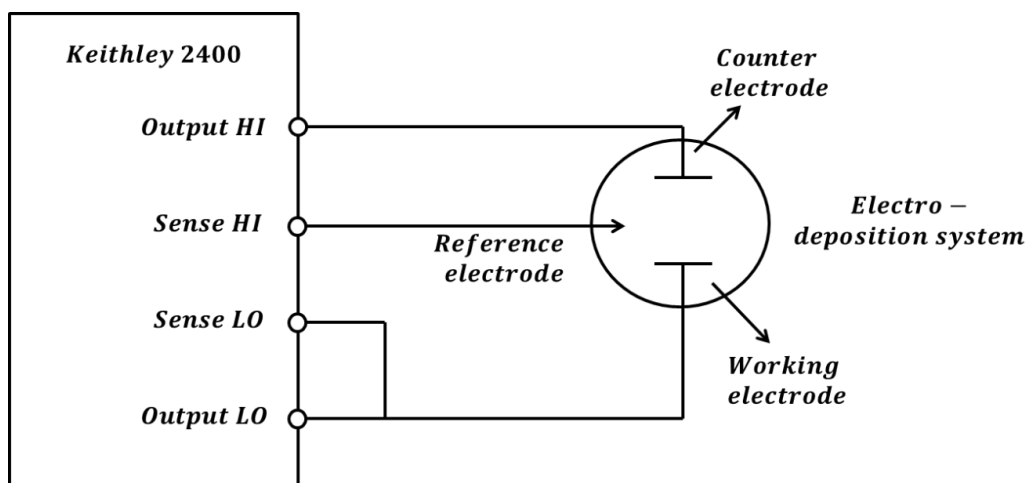


Figure 2-16. Schematic drawing of the Keithley source meter unit (SMU) working as a Potentiostat. Diagram redrawn from Ref. 5⁵.

2.8 Device Characterization

2.8.1 Ultraviolet Visible Spectroscopy

Ultraviolet visible spectroscopy (UV-visible) is a technique to measure the absorption or transmission under ultraviolet/visible radiation of a sample. It is achieved by directing ultraviolet and visible light to the sample and analyzing the emerging light. There are six types of electron transitions in a molecule as shown in Figure 2-18, $\sigma - \sigma^*$, $\sigma - \pi^*$, $\pi - \sigma^*$, $\pi - \pi^*$, $n - \sigma^*$ and $n - \pi^*$ transitions, and only the transitions with energy smaller than the radiation energy can occur. When ultraviolet and visible light with wavelength ranging from 200 nm to 800 nm is applied, the two lowest energy transitions - the $n \rightarrow \pi^*$ and the $\pi \rightarrow \pi^*$ transitions can be achieved. The electrons in those transitions are corresponding to the outer valence electrons in the molecular orbital, and the excitation can also be referred as from the HOMO to the LUMO.

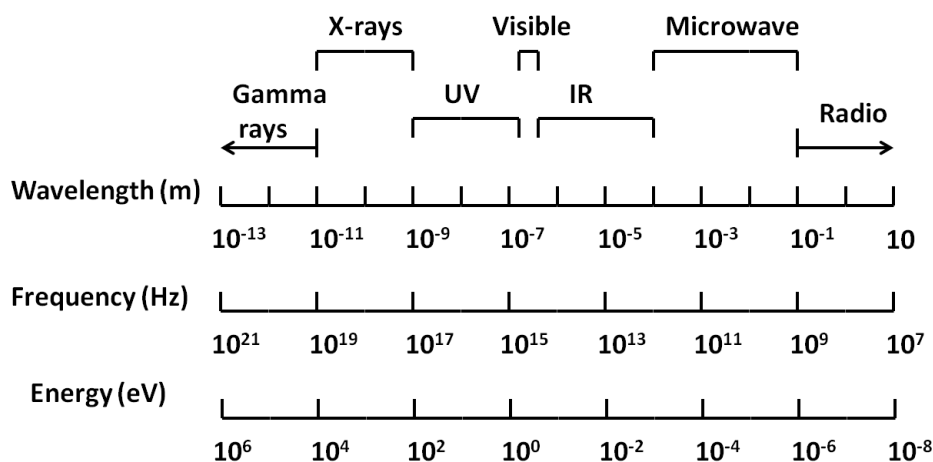


Figure 2-17. The electromagnetic spectrum. Diagram redrawn from Ref. 6⁶.

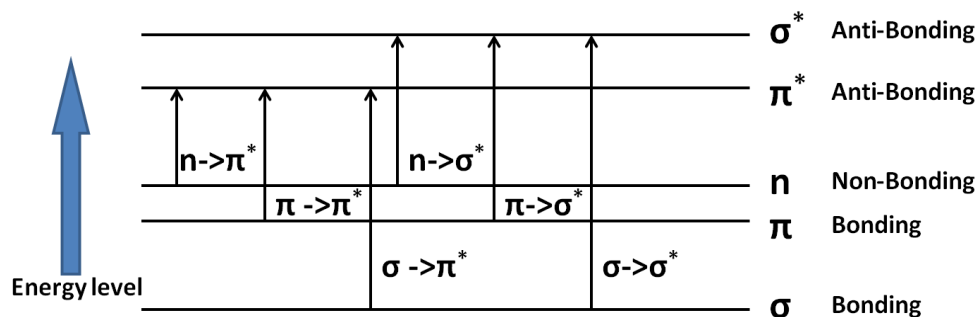


Figure 2-18. Electronic transitions occur in organic molecules. Diagram redrawn from Ref. 6 6.

The UV-visible spectrum measurement is very essential in the study of conjugated polymer films. Different materials have different absorption peaks in the UV-visible spectrum and by comparing spectra between materials or to the solar spectrum, one could adjust film thickness or deposition concentration, modify band gap of the conjugated material, check the crystallinity of the film using different processing methods and conditions.

The UV-visible equipment used for the measurements in this dissertation is an Ocean Optics HR2000+ high resolution spectrometer with a Mikropack PH-2000-BAL deuterium-halogen light. The experiment setup is shown in the schematic drawing in Figure 2-19.

The data were recorded and processed using a computer connected to the spectrometer with the manufacturer supplied software package 'Spectra Suite'. The light transmitted through the sample is collected through the optical fiber and passed into the spectrometer. Both liquid and solid state samples can be used in the measurement system.

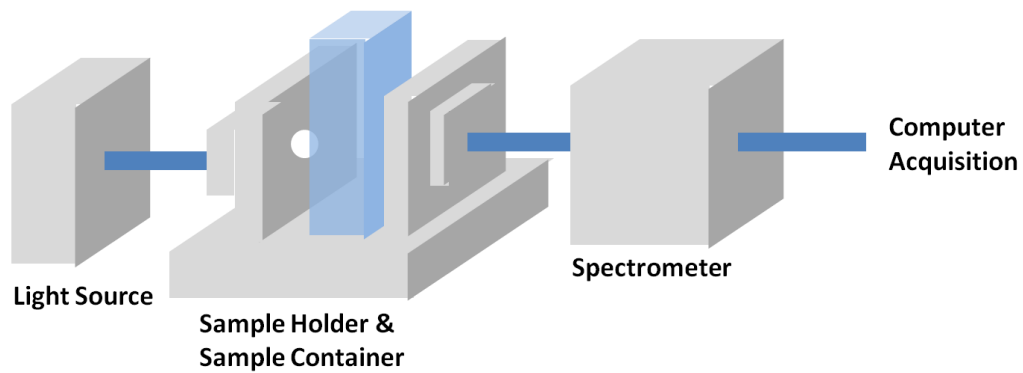


Figure 2-19. Schematic draw of UV-vis spectrum measuring system.

2.8.2 Atomic Force Microscopy

The atomic force microscope (AFM) is a scanning probe microscopy tool that is used to take images detailing the 3-D surface morphology of the materials on the order of fractions of nanometers. It uses a cantilever with a sharp tip as its probe to scan over the surface of the materials. By detecting the deflection or the change in oscillation amplitude/frequency/phase of the cantilever caused by the force interaction between the material surface and the cantilever tip, which can be mechanical contact force, van der Waals force, electrostatic force, and magnetic force, etc., we can get the topography of the sample.

There are mainly two types of measurement modes which depend on the distance of the tip and the specimen: surface-static and dynamic modes. The static mode is also called the contact mode in which the tip is in contact with the sample and stays in the region where the overall force is repulsive. The tip deflection is recorded as the feedback signal and to build the topography of the sample during scanning. This mode will not be able to

detect a liquid layer on top of the rigid surface. For the dynamic mode, the tip is oscillating above the sample surface with its fundamental resonance frequency instead of getting in direct contact of the sample. The change of the surface morphology will lead to a change in the tip to sample interaction force which will in term affect the oscillation amplitude, phase and resonance frequency. With the feedback signal the height of the tip will be adjusted allowing the software to construct a 3-D image of the sample surface. Depending on the resonance amplitude, the dynamic mode can be divided into non-contact mode and tapping mode. The non-contact mode usually has oscillation amplitude less than 20 nm while tip in the tapping mode usually oscillates with the amplitude greater than 20 nm, typically 20 nm to 200 nm, depending on the application. Figure 2-20 shows a schematic draw of the AFM in the dynamic mode.

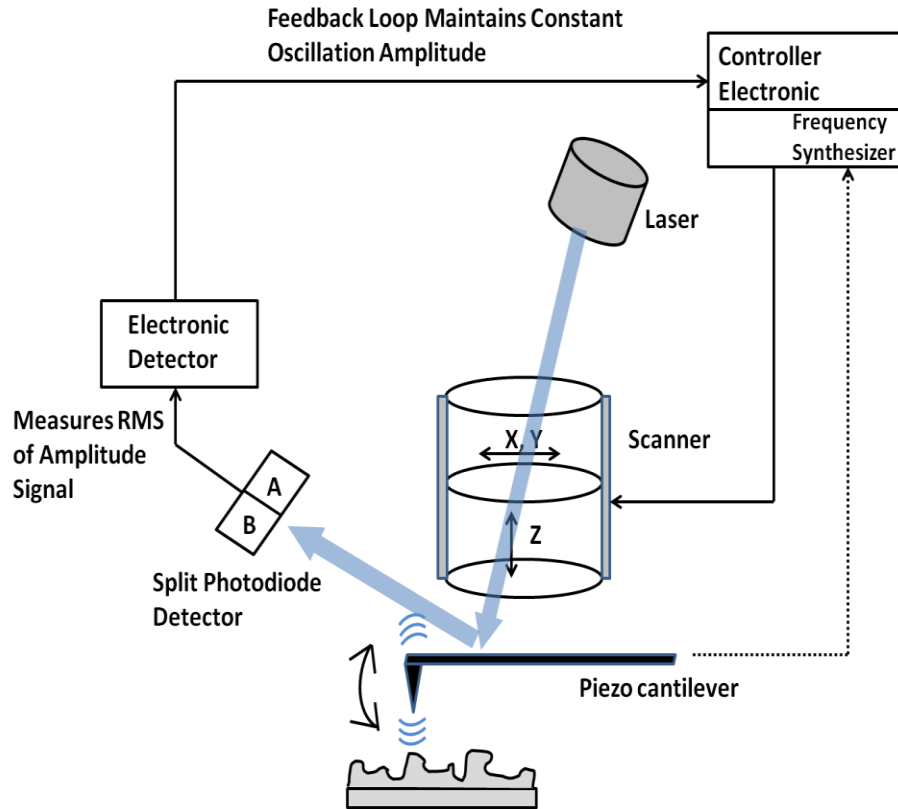


Figure 2-20. Schematic drawing of an AFM system.

The detection of the cantilever deflection is commonly realized by the beam deflection method as shown in Figure 2-21. In this method a laser light is shone by a solid state diode on to the back of the cantilever, after reflection it is collected by a position sensitive detector (PSD) with two closely spaced photodiodes. The deflection of the cantilever results in the deviation of the laser light so that one of the photodiode will collect more light than the other one, producing a signal directly related to the cantilever deflection. The signal will be collected by a differential amplifier and then be processed by the software to give the height of the tip.

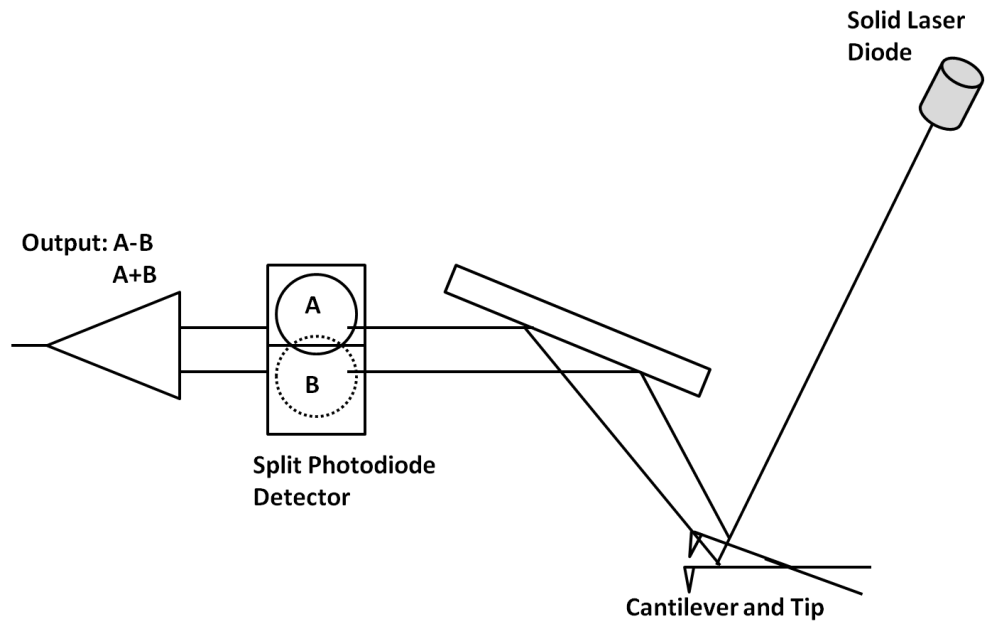


Figure 2-21. A schematic of “beam deflection” detection. Diagram is redrawn from Ref. 7⁷

The AFM equipment used for the measurement in this dissertation is a DI 3000 Nanscopy IIIA AFM. The tapping mode is mainly used in the measurement of the polymer surfaces. Silicon probes with spring constant 20 -100 N/m and resonant frequency in the range of 200 - 400 kHz are purchased and used. The cantilever length is $\sim 125 \mu\text{m}$ and the tip radius is $\sim 5 - 10 \text{ nm}$.

2.8.3 X-ray Photoelectron Spectroscopy

X-ray photoelectron spectroscopy (XPS) is a technique used to measure the elemental composition, empirical formula, electronic state and chemical state of the elements in a material. The spectrum is obtained by applying an X-ray beam to the material and measuring the kinetic energy and number of electrons that escape out from the materials surface. The binding energy of a certain element can be obtained by calculating the

energy difference between the incident photon and the escaped electrons and it is determined as

$$E_{binding} = E_{photon} - (E_{kinetic} - \phi) \quad (2.8.1)$$

in which $E_{binding}$ is the binding energy of the element, E_{photon} is the energy of the incident X-ray photon, $E_{kinetic}$ is the kinetic energy of the escaped electron and ϕ is the work function of the spectrometer. The XPS spectrum plots out the number of electrons detected as a function of the binding energy of the electrons. Thus, in the spectrum, the peaks will show all the electron configurations that exist in the material, and the height of these peaks will correspond to the proportion of the element with a certain chemical states. The XPS normally detects concentration limits up to 1000 ppm.

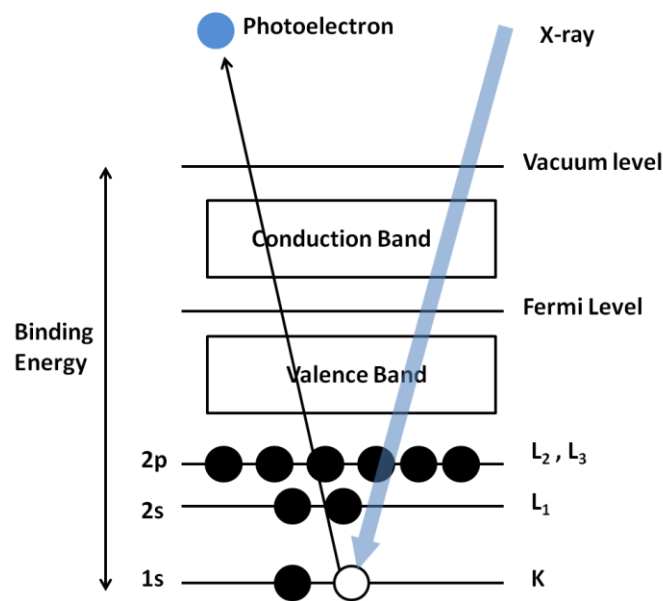


Figure 2-22. A schematic for the principle of the X-ray photoelectron spectroscopy.

The XPS basically is composed of a source of X-rays, a sample stage, an ultra-high vacuum (UHV) system, an electron collection lens, an electron energy analyzer, an electron detector system, sample mounts, sample introduction chamber, sample stage manipulator and Mu-metal magnetic field shielding. Some of the XPS equipment loaded with ion beam etching system will be able to do depth profile measurement of the material since the XPS measurement will usually detect the material compositions within the surface thickness of 1 to 10 nm. The UHV system is a requirement because in XPS, the measuring of the kinetic energy of the electron is very critical, and scattering between the electrons and the gas molecules has to be avoided. The X-ray source normally used is a monochromatic aluminum K-alpha X-rays produced by diffracting and focusing a beam of X-rays to a crystal with a certain orientation.

The XPS equipment used for all measurements in this dissertation is a Physical Electronics Model 5700 XPS instrument. The X-ray source used is a monochromatic Al- K_{α} X-ray with a photon energy of 1486.6 eV.

2.8.4 I-V Characteristic Measurement

The Keithley 2400 sourcemeter is used both in the electrochemical polymerization and electrical characterizations.

The photovoltaic current-voltage (I-V) Characterization is done using a Keithley 2400 sourcemeter inside a nitrogen filled gloved box with the relative humidity under 12 %. The light source is an Abet LS 150 Xenon Arc Lamp coupled with an AM 1.5 filter. When different light intensities are required, ITO slides are applied in front of the light

source to tailor the intensity. Light intensity is calibrated with an Oriel 91150 V Solar Reference Si Cell certified by the National Renewable Energy Laboratory (NREL) before each measurement.

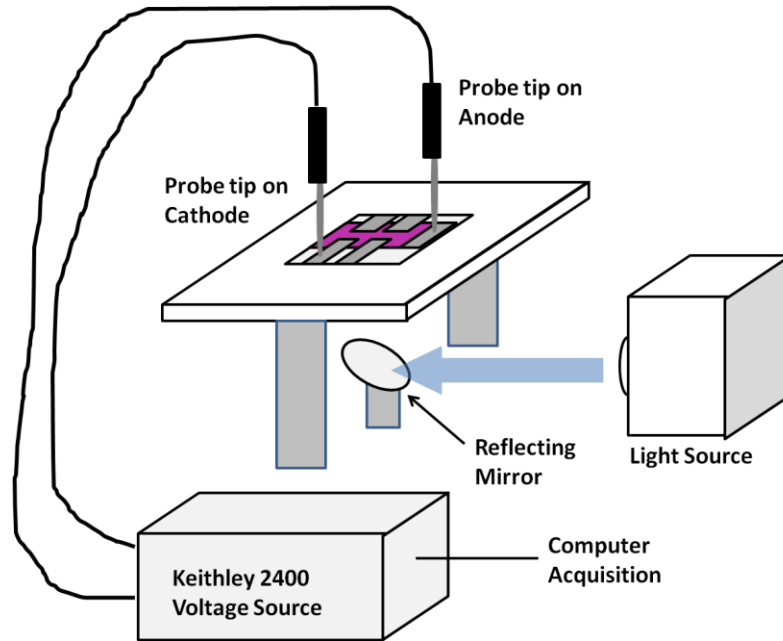


Figure 2-23. A schematic of the experimental set up for I-V measurements of a flat OPV device.

There are mainly two ways of operating the IV testing unit depending on how the light is to be incident onto the OPV device. The flat OPV device requires the light to be incident normal to the device and will use the standard measurement as shown in Figure 2-23; while the vertical device requires light to be incident from the side to measure angular dependence of performance. A schematic diagram in Figure 2-24 illustrates the setup for the measurement of the vertical device. The light will get in from the ‘window’ parallel to the device where no material is deposited and reaching the photo-generating layer by reflection and re-reflection inside the trap formed by the aluminum mirror. The device is

mounted on a sample stand, which can rotate around the center axis. The calibrated base at the bottom of the axis will record the angle of the incident light during rotation. The probing is done with two flat clips. Device areas of the photovoltaics devices are measured using a Leitz ERGOLUX microscope.

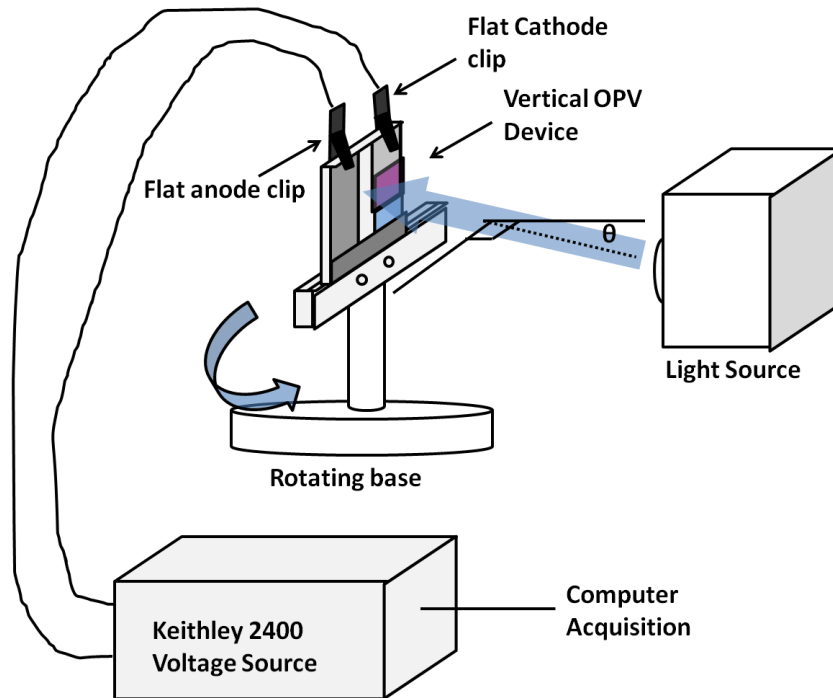


Figure 2-24. A schematic of the experimental set up for I-V measurements of a vertical OPV device

2.9 References

- <http://pubchem.ncbi.nlm.nih.gov/summary/summary.cgi?cid=16217324>.
- <http://www.sigmaaldrich.com/materials-science/organic-electronics/agfa-opv.html>.
- S. H. Middleman, A. K., *Process engineering analysis in semiconductor device fabrication* (McGraw-Hill (New York), 1993).

4 J. T. Stock, M. V. Orna, A. C. S. D. o. t. H. o. Chemistry, A. C. S. D. o. A.
Chemistry, and A. C. S. Meeting, *Electrochemistry, past and present* (American
Chemical Society, 1989).

5 <http://forum.keithley.com/phpBB3/viewtopic.php?f=13&t=13480>.

6 [http://www2.chemistry.msu.edu/faculty/reusch/VirtTxtJml/Spectrpy/UV-
Vis/spectrum.htm](http://www2.chemistry.msu.edu/faculty/reusch/VirtTxtJml/Spectrpy/UV-
Vis/spectrum.htm).

7 *Scanning Probe Microscopy Training Notebook, Version 3.0, Digital Instruments,
Veeco Metrology Group.*

3. Theory of Conjugated Materials and Their Properties

3.1 Energy Band Theory of Semiconductor

3.1.1 Energy Band Theory

When two identical atoms are brought closer together, their wave functions will start to overlap. As a result of the Pauli Exclusion Principle, where two identical electrons cannot share the same electronic state, the two atomic states will split into two different energy states with different binding energies. When more atoms are put together, there will be a further splitting of energy levels. The energy interval between each level becomes smaller and finally the energy levels will be nearly continuous and form an energy band.

Due to the boundary conditions of the Brillouin zone, there will be gaps between certain bands. The lowest energy band that doesn't have any electrons occupied at a temperature of 0 K is called the conduction band (CB). The highest energy band in which all energy states are occupied by electrons at 0 K is the valence band (VB). Conductors such as metals are the materials in which the VB and the CB overlap to some extent. There will be no energy gap between the two bands and the electrons can move from VB to CB easily and introduce conduction. Insulators on the other hand, typically have energy gaps exceeding 3 eV, making it very difficult for the electrons to get to the CB and generate any electric current. The semiconductors are materials with a slightly smaller band gap

than insulators, usually in the range of 0.1 to 3eV. Pure semiconductors have a poor conductivity. Electronic band structures for different materials are shown in Figure 3-1.

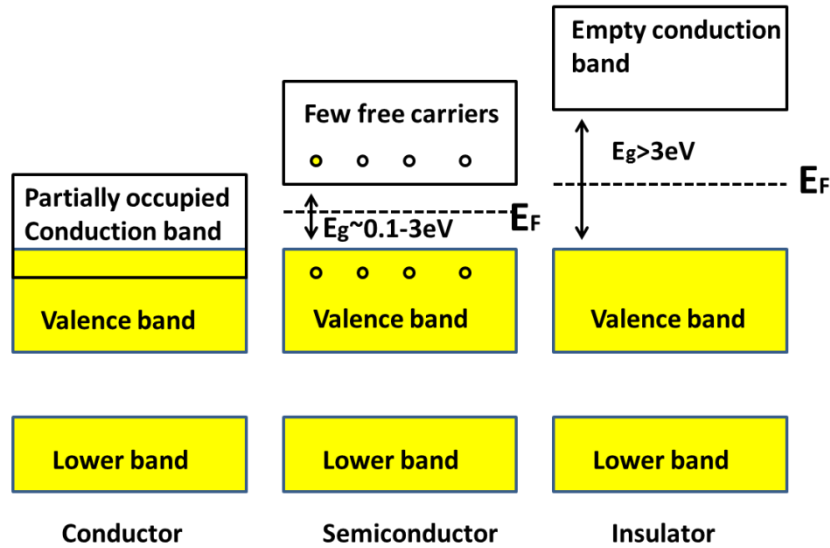


Figure 3-1. Electronic band structures for conductors, semiconductors and Insulators, diagram redrawn and adapted from ¹

Band theory was introduced when R. de L. Kronig and W. G. Penney developed a one dimensional model for the electron interaction in a periodic potential in 1931². In the model, an infinite one dimensional array of finite potential wells with the dimension of the lattice constant were used to simulate the electron environment. Forbidden energy levels around the Brillouin zone boundary were observed in their theory. In band theory, the individual energy levels become irrelevant and only the band diagram for the entire crystal will be discussed. The entire band structure will be summarized by two discrete

levels as mentioned before, the CB and the VB. The Schrödinger equation for the electrons in the crystal may be written as³

$$\left\{ -\frac{\hbar^2}{2m} \nabla^2 + V(r) \right\} \Psi_k = \varepsilon(k) \Psi_k \quad (3.1.1)$$

in which $V(r)$ is the periodic potential energy seen by an electron from the lattice; $\varepsilon(k)$ is the energy of the electron; m is the electron mass. Due to the periodicity of the potential energy, the solution Ψ_k to this equation can be written in the form of Bloch waves as

$$\Psi_k(r) = e^{ikr} u_k(r) \quad (3.1.2)$$

where $u_k(r)$ is the Bloch lattice function and $\Psi_k(r)$ is the Bloch wavefunction which will have periodicity throughout the crystal. Plenty of models have been applied in studying the band structures in the solid materials. As for metals, the electronic structures are typically calculated with the nearly free electron model which assumes that electrons can move almost freely through the crystal lattice; while in the study of polymer semiconductors or conductors, the tight binding approximation is frequently applied. The most frequently used band theories for semiconductors are the orthogonalized plane wave method⁴ and the pseudo-potential method⁵.

3.1.2 The Parabolic Band Approximation

At times when we discuss the electric phenomena in semiconductor, only the charges located near the maximum of the VB and the minimum of the CB are of interest, this is due to the fact that after vibration relaxation that is where the free moving charge carriers will be found. Near the minimum of the CB and the maximum of the valance band we

can use parabolic functions obtained from a Taylor expansion to approximate the energy band as⁶

$$E_{e,h}(\vec{k}) = E_{e,h}(0) \pm \frac{\hbar^2 \vec{k}^2}{2m^*} \quad (3.1.3)$$

in which $E_{e,h}(0)$ is the minimum energy in CB and maximum energy in VB, respectively; m^* is the effective mass for electron which takes in account the electron mass as well as the effect of internal force between the electron and other particles in the semiconductor material. It is defined as:

$$m^* = \hbar^2 \left[\frac{d^2 E_{e,h}(\vec{k})}{d\vec{k}^2} \right]^{-1} \quad (3.1.4)$$

The effective mass of the charge carriers will depend on the curvature of the energy band.

3.1.3 Direct and Indirect Band Gap Semiconductors

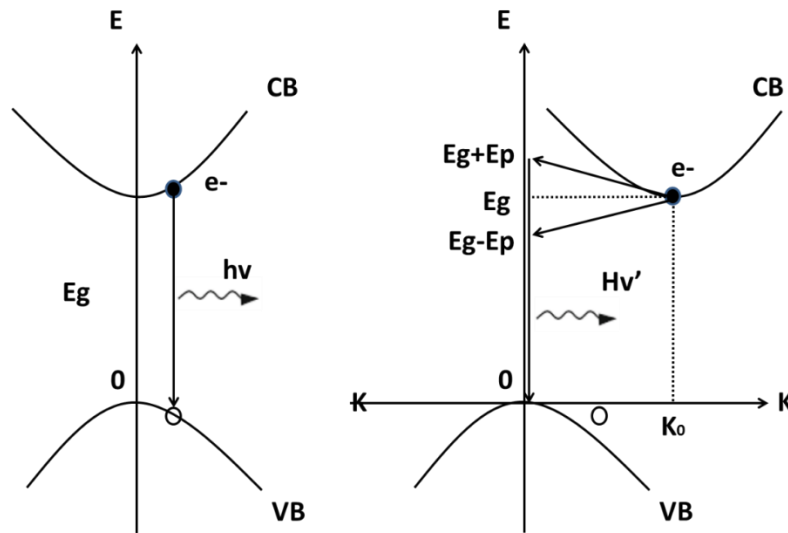


Figure 3-2. Electron transition in direct (left) and indirect (right) semiconductors, diagram redrawn from Ref. 7⁷.

The energy band diagram is plotted as a function of crystal momentum (k -vector) as shown in Table 3-2. If the minimum energy of the CB is achieved with the same k -vector of the maximum energy in the VB, the semiconductor is said to have a direct band gap; otherwise it has an indirect band gap. For the excitation of the electrons from VB to CB, both conservation of energy and crystal momentum needs to be achieved, thus it will be much easier for it occur in a direct band gap semiconductor where the electron momentum doesn't change; while for an indirect band gap semiconductor, not only does a photon with energy larger or equal to the band gap have to be absorbed by the material, but also a phonon in order to keep balance with the electron momentum shift. The involvement of the phonon makes the radiative process much less likely to occur within a particular time interval. The absorbance of a direct band gap semiconductor can be hundreds of times higher than that of one possessing an indirect band gap. This is the reason why a thick silicon film has to be fabricated in the solar device as a compromise of its low light absorbance. The Table 3-1 shows the band gap information of some inorganic semiconductors.

	Material	Direct/Indirect bandgap	Band Gap energy at 300 K (eV)
Elements	C (diamond)	Indirect	5.47
	Ge	Indirect	0.66
	Si	Indirect	1.12
	Sn (grey)	Direct	0.08
Groups III-V Compunds	GaAs	Direct	1.42
	InAs	Direct	0.36
	InSb	Direct	0.17
	GaP	Indirect	2.26
	GaN	Direct	3.36
	InN	Direct	0.70
Groups IV-IV Compunds	α -SiC	Indirect	2.99
Groups II-VI Compunds	ZnO	Direct	3.35
	CdSe	Direct	1.7
	ZnS	Direct	3.68

Table 3-1. Band gap value for some inorganic semiconductor materials. Table rebuilt from Ref. 8⁸.

3.2 Fermi Distribution and Quasi-Fermi Distribution

3.2.1 Intrinsic and Extrinsic Semiconductors

When an electron is excited from the VB to the CB, a hole is left in the VB. When no impurities are doped into the semiconductor and the electron density equals the hole density, it is called an intrinsic semiconductor. We will identify the electron and hole densities as n and p , respectively. When semiconductors are doped with materials that are added to provide free carriers, it is called an extrinsic semiconductor. The dopant giving additional electrons to the CB are called donors, and the donor energy level is below the CB within an interval $\sim kT$. Thus the electrons in the donor energy level may jump to the CB due to thermal activation, leaving an ionized positive charge in the donor energy level. Similarly, an acceptor energy level will stay around the thermal energy $\sim kT$ higher than that of VB, thus the electrons in the valance band can jump to the impurity energy level. The semiconductor with ionized donor will be called n-type and the one with acceptor impurity will be called p-type.

3.2.2 Density of States

The number of occupied conduction energy states due to thermal excitation is given as⁹:

$$n = \int_{E_c}^{E_{top}} g(E)F(E)dE \quad (3.2.1)$$

where E_c is the energy at the bottom of the CB and E_{top} is the energy at the highest level of the CB; $F(E)$ is the possibility that the energy E is occupied by an electron and will be Fermi distribution; $g(E)$ is the density of states defined as the number of states with

energy less than E . By calculating the number of states within the volume with radius k we write

$$N = 2 \times \frac{4}{3} \pi k^3 / \left(\frac{2\pi}{l} \right)^3 = \frac{k^3 l^3}{3\pi^2} \quad (3.2.2)$$

$$\frac{dN}{dE} = \frac{dN}{dk} \frac{dk}{dE} = \left(\frac{l}{\pi} \right)^3 \pi k^2 \frac{dk}{dE} \quad (3.2.3)$$

Using the parabolic approximation we can write the energy of the electrons as

$$E(k) = \frac{\hbar^2 k^2}{2m^*} \quad (3.2.4)$$

So density of states $g(E)$ per unit volume is

$$g(E) = \frac{1}{l^3} \frac{dN}{dE} = \frac{8\pi\sqrt{2}}{h^3} m^{*3/2} \sqrt{E} \quad (3.2.5)$$

3.2.3 Carrier Densities and Fermi Energy in Equilibrium

If the Fermi energy level is more than $3kT$ away from either side of the band edge, we call the semiconductor non-degenerate. In this case, the Fermi distribution can be simplified to a Maxwell-Boltzmann distribution. After integrating on Equation (3.2.1) we can get¹⁰

$$n = N_C e^{\frac{E_i - E_C}{k_B T}} = p = N_V e^{\frac{E_V - E_i}{k_B T}} \quad (3.2.6)$$

where N_C and N_V are the effective density of states for the CB and the VB, respectively.

They are expressed in the form of

$$N_C = 2\left(\frac{2\pi m_e^* k_B T}{h^2}\right)^{3/2} \quad (3.2.7)$$

and

$$N_V = 2\left(\frac{2\pi m_p^* k_B T}{h^2}\right)^{3/2} \quad (3.2.8)$$

The effective mass for the electrons and holes are

$$m_e^* = \hbar^2 \left[\frac{d^2 E_c(\vec{k})}{d\vec{k}^2} \right]^{-1} \quad (3.2.9)$$

and

$$m_h^* = -\hbar^2 \left[\frac{d^2 E_v(\vec{k})}{d\vec{k}^2} \right]^{-1} \quad (3.2.10)$$

And the Fermi level in intrinsic semiconductor E_i equals

$$E_i = \frac{E_C + E_V}{2} + \frac{1}{2} k_B T \ln \frac{N_V}{N_C} \quad (3.2.11)$$

It mostly lies in the middle between the CB and the VB. We can also have the mass action law as

$$np = n_i^2 = N_C N_V e^{\frac{-E_g}{k_B T}} \quad (3.2.12)$$

in which n_i is the intrinsic carrier density and is equal to the density of electrons which are thermally excited into the CB of a pure semiconductor; E_g is the band gap energy.

3.2.4 Quasi-Fermi Energy

When a disturbance is introduced to the semiconductor such as the exposure to light with photon energy larger than semiconductor band gap, the electrical injection of electrons through an applied electric bias or the doping to the material, the density of the charge carriers in the semiconductor will be higher than the equilibrium values, in which case we cannot apply the Fermi Dirac equilibrium distribution function in solving the carrier densities any longer and the relationship of $n = p = n_i$ will no longer stand. However, we could assume that the electrons and holes can each achieves a quasi-thermal equilibrium, after which all the electrons in the CB share a common electron quasi-Fermi level E_{F_n} and the holes in the VB shares a hole quasi-Fermi level E_{F_p} , with analogy to Equations (3.2.6), we can write⁹

$$n = N_C e^{\frac{E_{F_n} - E_C}{kT}} \quad (3.2.13)$$

and

$$p = N_V e^{\frac{E_V - E_{F_p}}{kT}} \quad (3.2.14)$$

Looking at the charge density in terms of n_i instead of density of states we write

$$n = n_i e^{\frac{E_{F_n} - E_i}{kT}} \quad (3.2.15)$$

and

$$p = n_i e^{\frac{E_i - E_{F_p}}{kT}} \quad (3.2.16)$$

where E_i and n_i are the Fermi level and the equilibrium charge density in intrinsic semiconductor, respectively. Rearrange these two equations we can write out the Fermi level in quasi-thermal equilibrium⁹ or in extrinsic semiconductor¹⁰ as

$$E_{F_n} = E_i + kT \ln \frac{n}{n_i} \quad (3.2.17)$$

and

$$E_F = E_i - kT \ln \frac{p}{n_i} \quad (3.2.18)$$

where n and p will be the total majority electron and hole densities in the semiconductor, respectively. From the two equations, it is clear that the Fermi energy will shift upward to the CB in n-type semiconductor and downward to the VB in p-type semiconductor, as shown in Figure 3-3.

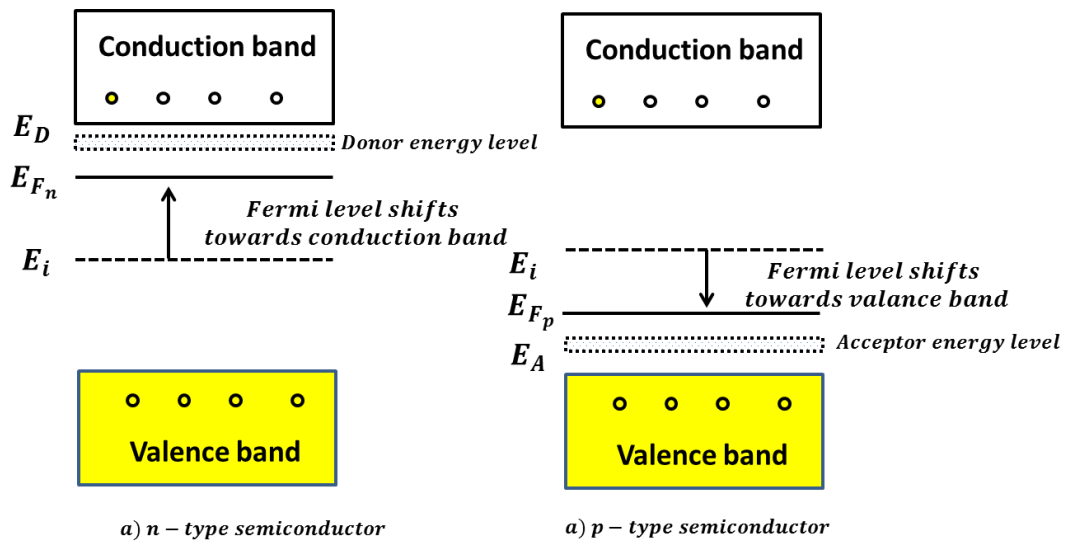


Figure 3-3. Energy band diagrams in extrinsic semiconductors, diagrams redrawn from Ref. 11¹¹.

The difference in quasi-Fermi levels is the difference in chemical potentials (the same as Fermi level) $\Delta\mu$. The mass action law is now written as

$$np = n_i^2 e^{\Delta\mu/kT} \quad (3.2.19)$$

where

$$\Delta\mu = E_{F_n} - E_{F_p} \quad (3.2.20)$$

3.3 Atomic and Molecular Orbitals

3.3.1 Chemical Bonds

There are roughly four types of bonding found in solids: the ionic bond, the metallic bond, the covalent bond, and the van der Waals interactions. The nature of the bonding force yields material properties that are very different evidenced in the difference between inorganic photovoltaics and organic photovoltaics.

The covalent bond is realized by two neighboring atoms sharing two or more electrons; the bonding can have a polar character, which results in a much lower melting points and poor electrical conductivity. The metallic bond is also formed by Columbic force, where the electrons are delocalized throughout the solid. The solids with metallic bonds have quite high electrical conductivity and reflectivity. The ionic bond is formed by the columbic attraction between ions and the charges, it tends to have relatively high melting points and the solids are rather brittle. Ionic conductivity is observed above the melting point. The bonds in conjugated molecules are covalent and van der Waals forces.

3.3.2 Atomic Orbitals

An atomic orbital (AO) is a wave function used to describe the possibility of finding an electron at any position around the atom's nucleus. Each orbital has three quantum numbers n , l and m , in which n represents the radius of the orbital, l represents angular momentum, and m the spin vector. All variables are integers and there is a relationship between l and n : l can be any integer within the range of $0 \leq l \leq (n - 1)$. With respect to different numbers $l=0,1,2$ and 3 , the orbitals can be named as s orbital, p orbital, d orbital and f orbital respectively. Each set of quantum number (n, l, m) corresponds to an AO and can hold a maximum electron number of 2 with two different spin vectors ($m = \pm 1$). The shape of the orbital will be determined by angular quantum number l and is defined as the region inside which the probability density $|\Psi(r, \theta, \varphi)|^2$ of finding the electron will be a certain value. The shapes of the single s-orbital ($l=0$) and three p-orbitals are shown in Figure 3-4.

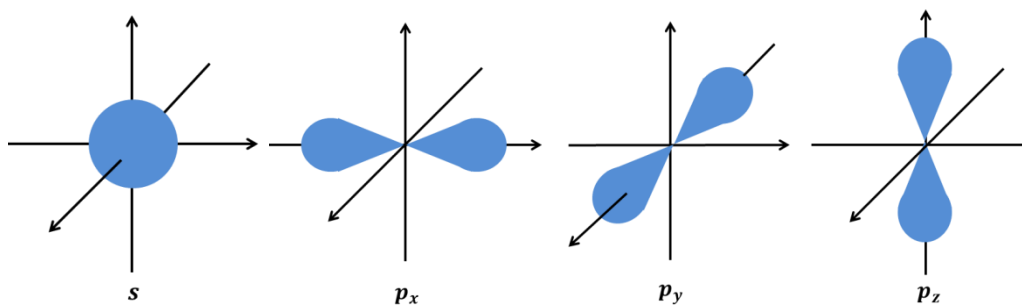


Figure 3-4. Schematic drawing of s and p AO.

3.3.3 Molecular Orbitals

Similar to the AO, the molecular orbital (MO) is the wavefunction used to describe the probability of finding an electron, only it is at any region encompassing more than one nucleus and is around the whole molecule. The MOs are formed by the overlap of two AOs or hybrid orbitals from each atom of the molecule, in the way calculated by the linear combination of atomic orbitals (LCAO), which was introduced in 1929 by Sir John Lennard-Jones¹². The number of MOs formed will be equal to the number of AOs being combined to form the molecule, such that if two AOs ψ_a and ψ_b are put together, two MOs will be formed with the wavefunctions written as:

$$\Psi = C_a\psi_a + C_b\psi_b \quad (3.3.1)$$

$$\Psi^* = C_a\psi_a - C_b\psi_b \quad (3.3.2)$$

where Ψ and Ψ^* are the molecular wavefunctions for the bonding and anti-bonding MOs, respectively. The bonding MOs are constructive interactions and are lower in energy than the AOs that combine to produce them; while the anti-bonding MOs are destructive interactions and are higher in energy than the AOs as shown in Figure 3-5. There is also the third type of MOs called non-bonding MO, in which the electrons will not form MOs due to the lack of compatible symmetries of the AOs. The HOMO and LUMO level doesn't necessarily correspond to the bonding and anti-bonding molecule level. A very basic example of the combination of two AOs is the covalent σ -bond created between two hydrogen atoms in the formation of MOs for the hydrogen molecule (H_2) as shown in Figure 3-5.

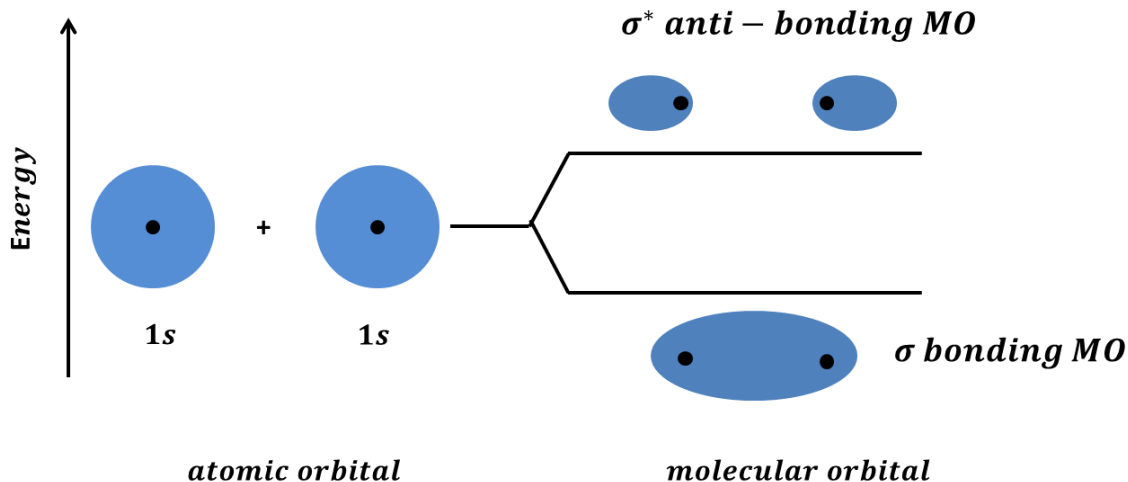


Figure 3-5. An energy level diagram showing two 1s AOs combining into two molecular orbital in H_2 .
Diagram redrawn from Ref. 13¹³.

3.3.4 Orbital Hybridization

The electronic configuration of the carbon atom is $1s^2 2s^2 2p^2$, there are four electrons in the most outer electronic level: two paired s-orbital electrons and two unpaired p-orbital electrons. A carbon may have an alternate electron configuration resulting from AO hybridization, where the new configuration will help to have more stable bond with other atoms. The hybridization of the AOs is the mixing of a number of different orbitals to the same energy level and create a corresponding number of hybrid orbitals.

There are three types of hybridization (sp^3 , sp^2 , sp) in carbon atoms depending on the number of the $2p$ orbitals that are involved in the hybridization ($n=3, 2, 1$). When the $2s$ -orbital mixes with three $2p$ orbitals (p_x, p_y, p_z) to form 4 equivalent degenerate orbitals, it is called sp^3 hybridization. The 4 hybridized orbitals will form a tetrahedral geometry

around the atom, with the bond angle approximately equaling to 109.5° . Such as the C-H bonds found in methane (Figure 3-6). The four identical hybridized orbitals form four σ bonds with four hydrogen $1s$ orbitals.

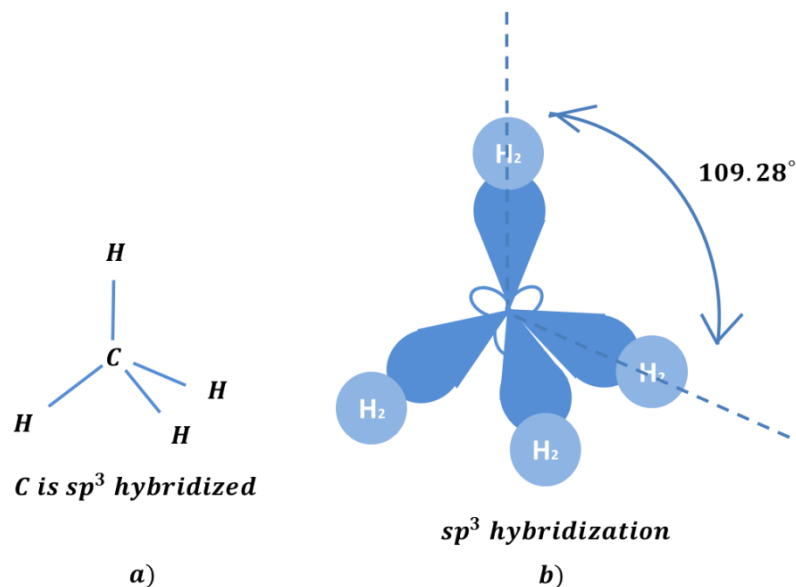


Figure 3-6. a) Molecular structure of methane; b) Three dimensional representations of four sp^3 hybrid orbitals in methane. Diagrams redrawn from Ref. 14 ¹⁴.

When the $2s$ AO is mixed with two $2p$ AOs to form three degenerate orbitals, the $2s$ -orbital will mix with two of the three once mutually orthogonal atomic p -orbitals while the other one stays unchanged. It is called the sp^2 hybridization. The molecular geometry with sp^2 hybridization shows a coplanar geometry; the bond angle is 120° apart from each other with the p_z orbital perpendicular to the plane. A typical molecule found with this structure is benzene, and all aromatic derivatives as seen in Figure 3-7. The overlapping p_z orbitals allow the delocalization of the π electrons over the whole molecule and lower the overall energy of the molecule.

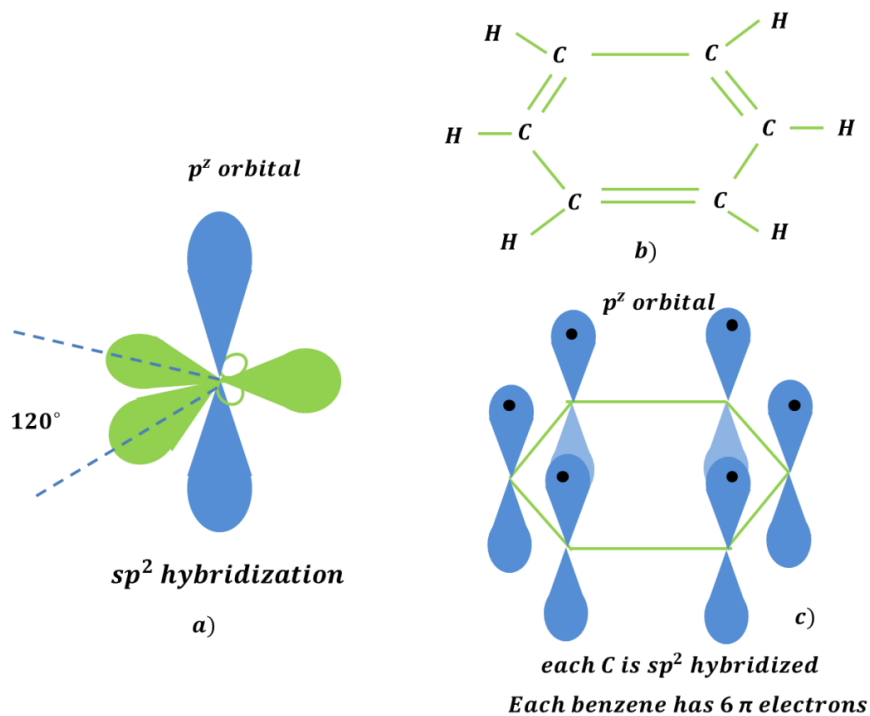


Figure 3-7. a) Three dimensional representation of a sp^2 hybridized C; b) molecular structure of benzene; c) bond formation in benzene. Diagrams redrawn from Ref. 14¹⁴.

An sp hybrid orbital is formed when the $2s$ -orbital is promoted to mix with one $2p$ -orbital. The two new hybridized orbitals are oriented at 180° to each other forming two σ bonds. The two remaining p -orbitals will then form π bonds perpendicular to the molecular axis. A typical example of this kind is an acetylene (C_2H_2) in which the triple bond is composed of one hybridized σ bond and two pairs of overlapped p -orbitals (Figure 3-8).

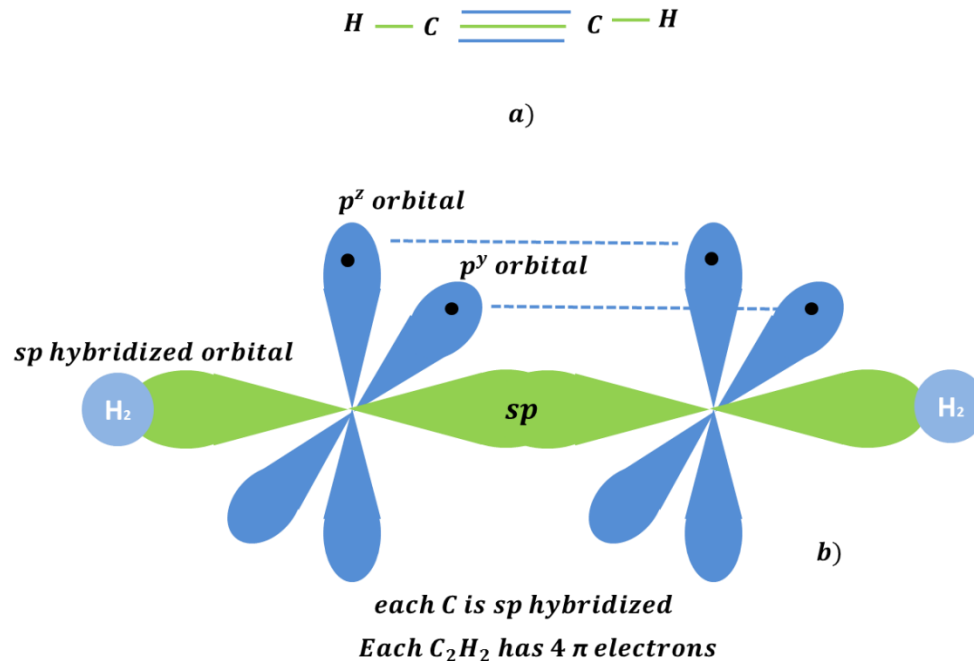


Figure 3-8. a) molecular structure of C₂H₂; b) bond formation in C₂H₂. Diagrams redrawn from Ref. 14¹⁴.

3.4 Conductivity in Conjugated Polymers

Unlike the charge carriers in crystallized inorganic semiconductors, which can travel almost freely through the material, the electrons and holes in organic materials will be more constrained and less delocalized. Organic conductors after crystallization are aggregated in units, with each unit as a polymer of a long conjugated back bone like a chain. Each polymer unit has specific molecular energy levels, with HOMO as the highest occupied MO and LUMO as the lowest unoccupied MO. Electrons/holes can travel on this conjugated polymer chain very rapidly. However, if the electrons/holes need to get from one unit to another, the conduction has to be accomplished by hopping.

In organic materials, not only does temperature but also the binding energy from different atomic sites will affect the mobilities.

Numerous models have been introduced to interpret the charge carrier mobility in organic conductors. The Nearest neighbor hopping (NNH) process is the earliest hopping model brought up by Kasuya and Koide in 1958¹⁵. This model assumed that the electrons will be localized and the hopping among different sites will most probably happen between the nearest neighbors due to the large transfer integral between these sites. The expression of mobility in this model is written as

$$\mu \propto \exp\left(-W/kT\right) \quad (3.4.1)$$

where W is the energy separation. In 1968, Mott introduced another kind of conducting model—the variable range hopping¹⁶. In this model, Mott introduced a fourth parameter into the hopping space—energy. He mentioned that the hopping probability will not only depend on the spatial parameters anymore, but also an energy separation. With the existence of the energy variable in the hopping space, the hopping probability will increase with a factor of $\exp\left(-\frac{W}{kT}\right)$, and the electrons might hop to sites further away in space but closer in energy. The jumping frequency is written in the form as

$$p = v_{ph} \exp\left(-2\alpha R - \frac{W}{kT}\right) \quad (3.4.2)$$

in which v_{ph} is the hopping frequency and α the decay rate of the wavefunction; R is the special distance between two sites and W is the energy separation. Using Miller and

Abraham conductance, he successfully described the observed temperature dependence of charge mobility as

$$\log\mu \sim T^{-1/4} \quad (3.4.3)$$

Mobility values for some organic conductors can be seen in Table 3-2¹⁷.

Material		Mobility (m ² /Vs)
p-type	Polythiophene ¹⁸	3×10^{-9}
	Polyacetylene	10^{-8}
	Phtalocyanine	2×10^{-6}
	Pentacene	1.5×10^{-4}
n-type	C ₆₀	$8 \times 10^{-6} - 3 \times 10^{-5}$
	C ₆₀ (0.9) /C ₇₀ (0.1)	10^{-8}
	PTCDA	$10^{-8} - 10^{-9}$
	PCBM ¹⁹	3×10^{-7}

Table 3-2. Electron and hole mobilities for some organic semiconductors. Table rearranged from Ref. 17¹⁷.

3.5 Excitons and Optical Spectroscopic Properties of Conjugated Polymer

3.5.1 Quasi-particles in Organic Semiconductors

3.5.1.1 Doping in Conjugated Polymer

Most linear conjugated polymers such as polyacetylene or polyparaphenylene with a π system along the polymer chain are often semiconductors or insulators; however, it was discovered that an increase in conductivity can be achieved by applying redox chemistry to these intrinsically insulating polymers²⁰. This chemical treatment is also called “doping” analogous to the doping in inorganic semiconductors. However, instead of applying additives into the inorganic semiconductors, the “doping” in organic polymers is the process of oxidation or reduction of a polymer system. The use of an oxidizing agent to the polymer corresponds to p-type doping; while the use of a reducing agent corresponds to n-type doping.

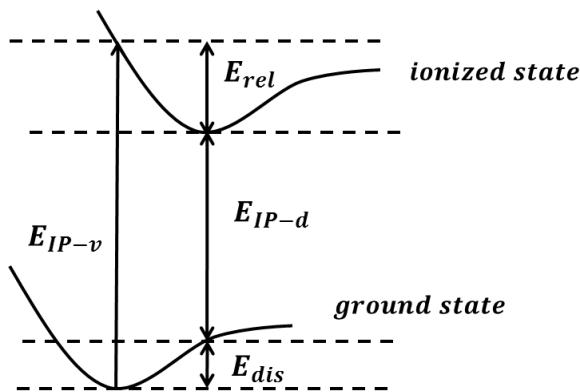


Figure 3-9. Illustration of the energies involved in a molecular ionization process. Diagram redrawn from Ref. 21²¹.

For organic molecules, it is usually the case that the molecule or electron geometry in equilibrium ionized state is different than that of the ground state. As shown in Figure 3-9, the lowest energy in the ionized state of the molecule is shifted away to a different k -vector from where ground state achieved its minimum energy. A vertical Franck-Condon like ionization is processed with an excitation energy of E_{IP-v} , after that a geometry relaxation happens with a release of energy E_{rel} . However, this process can also be achieved by a molecule which first distorts to the equilibrium ionized geometry when it is still in the ground state, and then process the excitation directly to the equilibrium ionized state with an excitation energy of E_{IP-d} . The distortion energy required by the molecule is E_{dis} . In the one-electron energy level of the molecule, the distortion will correspond to an upward shift $\Delta\varepsilon$ of the HOMO level and a downward shift of the LUMO level.

3.5.1.2 Polarons

As mentioned above, after the addition/reduction of one electron from an organic polymer, it is energetically favorable to localize the charge on the polymer chain and have a local distortion around the charge. This radical ion associated with the lattice distortion is called a polaron, and the formation of the polaron will introduce an energy level $\Delta\varepsilon$ below/above the LUMO/HOMO level called the polaron energy level, as shown in Figure 3-10 (The figure shows a positive polaron formed by the extraction of an electron from the semiconductor). The relaxation energy E_{rel} is also called the polaron binding energy, and is measured to be in the order of 0.05 eV in polyamide (PA), 0.03 eV in poly(p-phenylene) (PPP) and 0.12 eV in Polypyrrole (PPy)²¹. When the doping continues and more polarons are formed in the polymer, polaron band will be formed and

thus the conductivity goes up. To introduce an electron polaron, an electron will be taken from the donor or from photoexcitation, and is added to the upper polaron level. To introduce a hole polaron, an electron from the lower polaron level will go to the acceptor or a hole will be created by photoexcitation²². The evolution of the band structure from that in a pristine polymer to polaron bands merged with the VB and CB is shown in Figure 3-10.

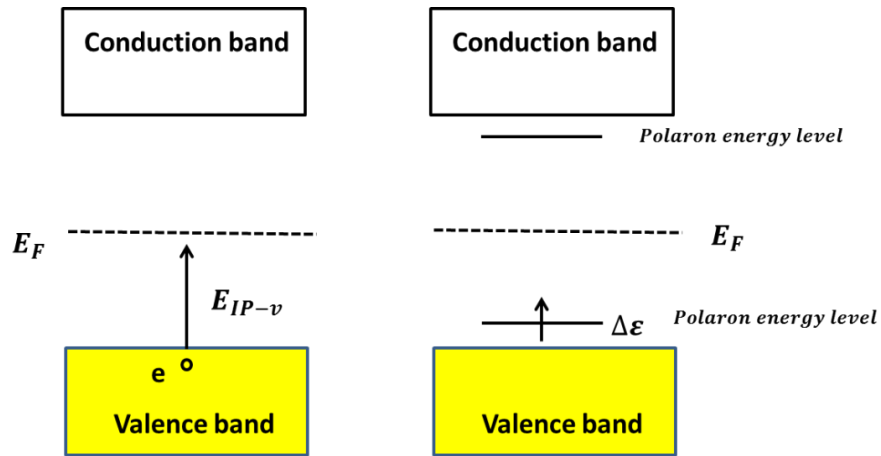


Figure 3-10. Band structure of a polymer chain without (left) and with (right) a p+ polaron level. Diagram redrawn from Ref. 21²¹.

3.5.1.3 Bipolarons

Bipolarons are formed at heavy doping levels. A bipolaron is the radical ion and the lattice distortion in the polymer chain when a second electron is added or removed from the existing polaron. The formation of a bipolaron implies a strong lattice distortion as the interaction of the bipolaron with the lattice needs to be larger than the coulomb repulsion between the two charges to make the structure stable. Thus, in the electronic band structure, the energy level of a bipolaron will be further away from the band edges

than the one in polaron, as shown in Figure 3-11. The bipolaron binding energy E_{rel}^{bip} will be larger than that of two polarons for about 0.45 eV as measured in PPy and 0.34 eV in PPP²¹. Hence one bipolaron is thermodynamically more stable than two polarons in the polymer. In case of positive (negative) charges, the polaron levels are empty (fully occupied) and the bipolaron is a spinless quasi-particle. Therefore, there is no optical transition between the lower and the upper bipolaron levels.

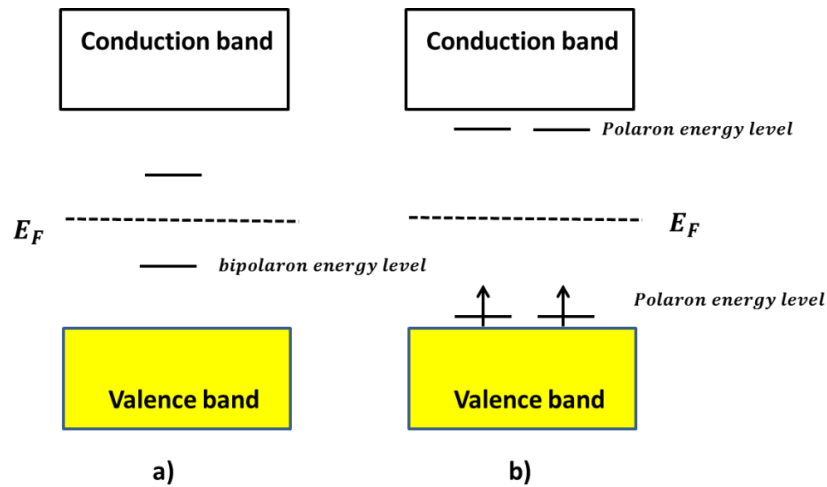


Figure 3-11. Band structure of a polymer chain with a) a p+ bipolaron and b) two p+ polarons.

Diagram redrawn from Ref. 21²¹.

3.5.1.4 Solitons

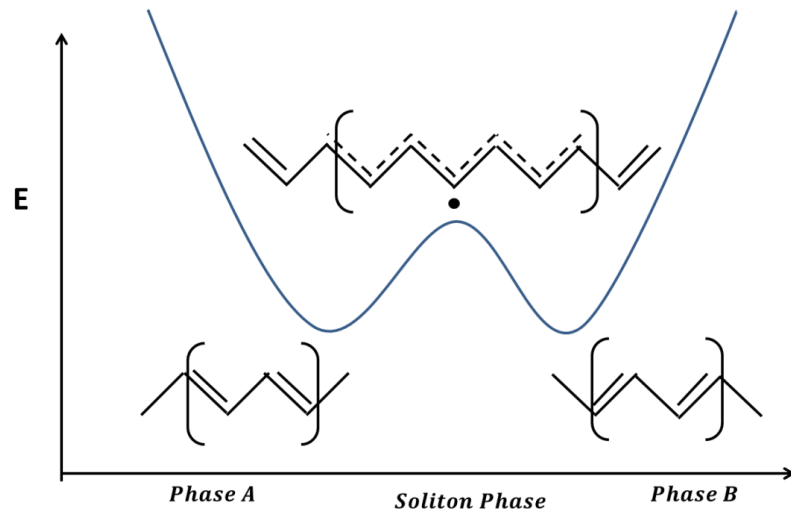


Figure 3-12. The energy curve for an infinite trans-polyacetylene chain with three different configuration structures. Diagram redrawn from Ref. 17¹⁷.

If a polymer has two possible geometric structures corresponding to the same total energy, it then possesses a degenerate ground state. A typical polymer in this case is Polyacetylene. As the result of the energy degeneracy, a bipolaron formed in this type of polymer can be easily separated as there is no increase in distortion energy for this process. The two different structures with the same energy level will be distributed on different segments that are separated by the charge; in this case, the charge associated with a boundary is called a soliton. The presence of the soliton will lead to the appearance of a localized electronic level at mid-gap between CB and VB, which will be half occupied for a neutral soliton formed with odd number of conjugated carbons in the system and empty/full occupied for a positively/negatively charged soliton²³. A charge delocalization is also found around the soliton.

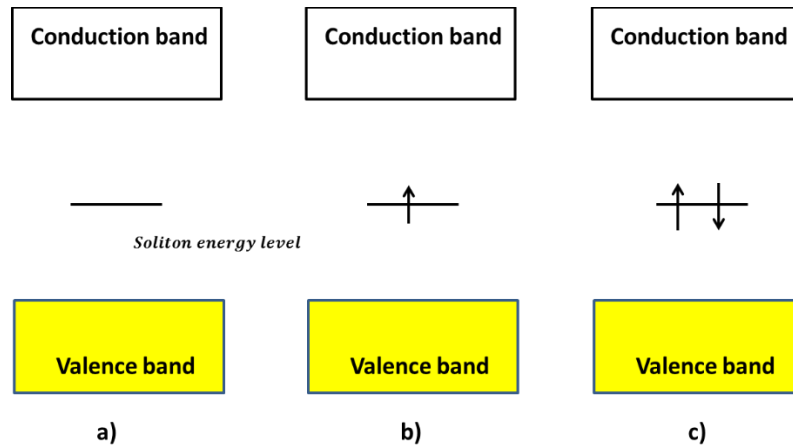


Figure 3-13. Band structure for a trans-polyacetylene chain containing a) a positively charged b) neutral c) negatively charged soliton. Diagrams redrawn from Ref. 17¹⁷.

3.5.1.5 Excitons

3.5.1.5.1 Wannier Excitons

In semiconductors with high dielectric constant, excitons with radius of the order of ten times the lattice constant can be found, this type of exciton is called a Wannier or a Wannier-Mott exciton. Wannier excitons are mostly found in inorganic systems, where the electron-hole interaction energy is small (a few meV typically).

Considering the coulomb potential between the electron and hole pair as

$$U(r) = -\frac{e^2}{4\pi\epsilon_0\epsilon r} \tag{3.5.1}$$

where r is the distance between the electron and hole; ϵ is the dielectric constant of the material, typically $\epsilon \geq 10$ for inorganic semiconductors²⁴. Taking Coulombic interaction

as the only force between the electron-hole pair, we can apply the Bohr model of the hydrogen atom to the free Wannier exciton and solve for the binding energy level of the electron-hole pair. Before applying the hydrogen electron model, a number of adjustments are required; unlike the real hydrogen atomic system, which is composed of a very heavy nucleus and a negligible electron, the electron-hole system is formed by two quasi-particles with comparable masses. Additionally, the Coulomb force between the electron and hole in a Wannier exciton will be largely screened by the dielectric constant. In this case, an effective mass is used to replace the proton mass in the hydrogen atom

$$m_r = \frac{m_e^* m_h^*}{m_e^* + m_h^*} \quad (3.5.2)$$

After including a dielectric constant ε in the energy level expression,²⁵ the binding energy of a Wannier exciton can be written as

$$E_{X(n)} = \frac{m_r/m_0}{\varepsilon^2} \frac{1}{n^2} Ry(H) = \frac{E_X}{n^2} \quad (3.5.3)$$

in which m_0 is the free electron mass and $Ry(H) = 13.6 \text{ eV}$ refers to the ground state of the hydrogen atom, also known as Rydberg binding energy; m_e^* (m_h^*) is the electron (hole) effective mass; E_X is the binding energy at ground level and n is the energy level. Comparing the two binding energies E_X and $Ry(H)$, it is clear that the Wannier exciton binding energy is around three orders of magnitude smaller than the hydrogen binding energy.

The free Wannier exciton can move throughout the lattice. Taking the assumption that it has kinetic energy of

$$E_{kin} = \frac{\hbar^2 K^2}{2(m_e + m_h)} \quad (3.5.4)$$

The total energy of a Wannier exciton in the lattice as ²⁵ may be expressed as

$$\begin{aligned} E_{(n)}(K) &= E_g - E_{X(n)} + E_{kin} \\ &= E_g - \frac{(m_r/m_0) Ry(H)}{\epsilon^2 n^2} + \frac{\hbar^2 K^2}{2(m_e + m_h)} \end{aligned} \quad (3.5.5)$$

where K is the exciton wave vector; E_g is energy band gap of the lattice between CB and the ground state of the ideal pure crystal. The exciton energy level is depicted in Figure 3-14.

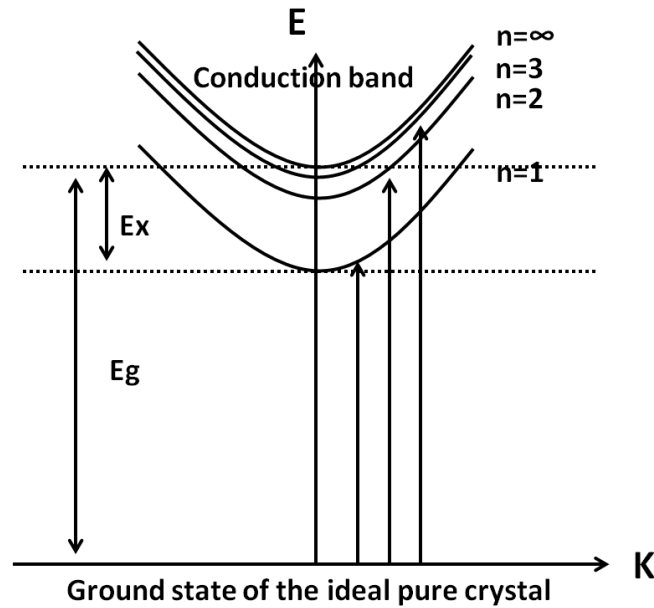


Figure 3-14. Excitation energy of an e-h pair in a Wannier exciton as a function of translational wave vector K , optical absorption transitions are also marked. Diagram redrawn from Ref. 25 ²⁵.

3.5.1.5.2 Frenkel Excitons

In 1931 the concept of excitation waves in crystals was introduced and the term “exciton” was invented by a Russian theorist Yakov Frenkel to explain the photoemission lines observed in the spectra of organic molecular crystals²⁶. Later the Frenkel exciton was used to represent excitons with strong coulomb interactions between the excited electron and the hole in the semiconducting material with a small dielectric constant. The binding energy of the exciton is approximately 100~300 meV and its radius is small while the electron-hole pair resides on the same molecular site. Frenkel excitons are typically found in organic molecular crystals composed of benzene rings such as anthracene and naphthacene.

If we consider the system as a linear crystal lattice with N identical molecules, each with one spinless electron, the periodic Eigen-functions of electrons can be written in a Bloch state²⁷ as

$$\Psi_K = N^{-1/2} \sum_m [\exp(iKR_m)]\phi_m \quad (3.5.6)$$

here the expression of Eigen-functions Ψ_K satisfies the normalization condition; ϕ_m is the Slater determinant of the electronic configuration when only the electron in the m^{th} molecule at R_m is excited. K is the wave vector. We take the interactions between molecules as perturbation and apply the tight-binding model for a one electron Bloch state, the eigen-values corresponding to the N split states can be written as²⁸

$$E(K) = E_n + \delta\omega_n + 2\beta \cos(kd) \quad (3.5.7)$$

in which E_n is the energy of the excited atomic level, $\delta\omega_n = \delta\epsilon - \delta\omega_{n0}$ where $\delta\epsilon$ is the change in the cohesive energy per molecule and $\delta\omega_{n0}$ is the shift of the center of the exciton band on the n^{th} energy level. β is the interaction between neighboring atoms, d is the nearest neighbor separation. A scheme illustrating this energy state splitting and the energy level shifts parameters is shown in Figure 3-15.

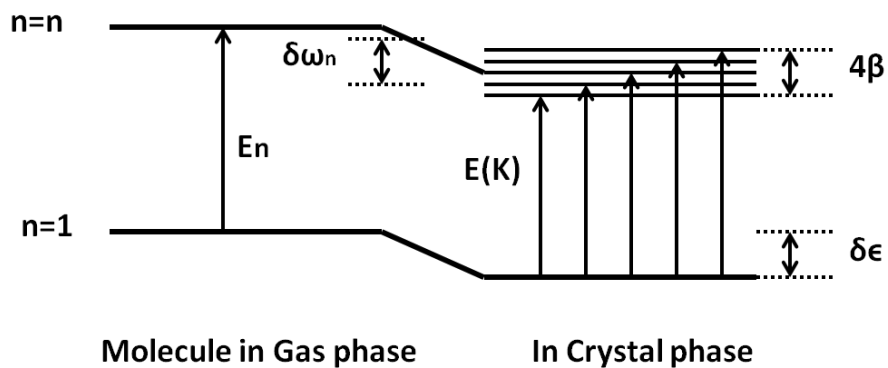


Figure 3-15. Energy level scheme illustrating shifts in ground and excited states for the crystal phase relative to the vapor phase. Diagram redrawn from Ref. 28²⁸.

3.5.1.5.3 Charge-transfer States

When the exciton radius is in between the size of Wannier and Frenkel exciton, it is called an ionic exciton, a term introduced by Lyons in 1967 or charge transfer excitons²⁸. The spatial extent of this state will be around one or two lattice constants and can be found either in organic or inorganic crystals.

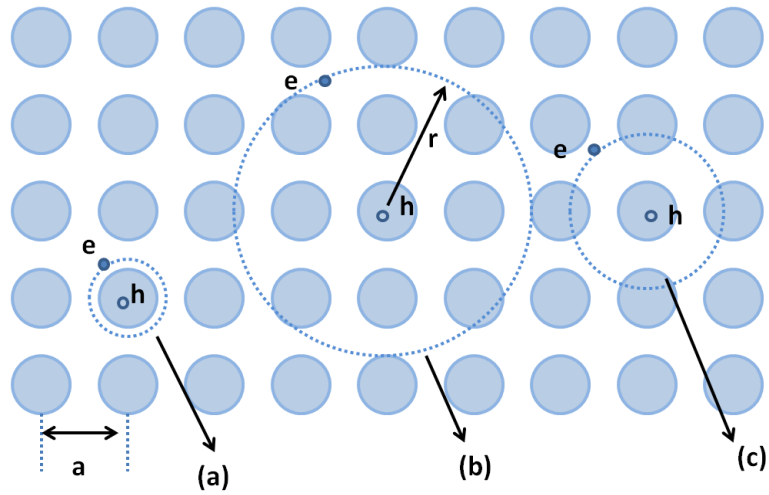


Figure 3-16. The correlating range of the three types of exciton in the crystal with the lattice constant a . (a) Frenkel exciton. (b) The Wannier-Mott exciton in which r is the radius of the exciton. (c) The intermediate charge-transfer exciton. Diagram redrawn from Ref. 28²⁸.

3.6 Photon Absorption and Emission Process

3.6.1 The Jablonski Diagram

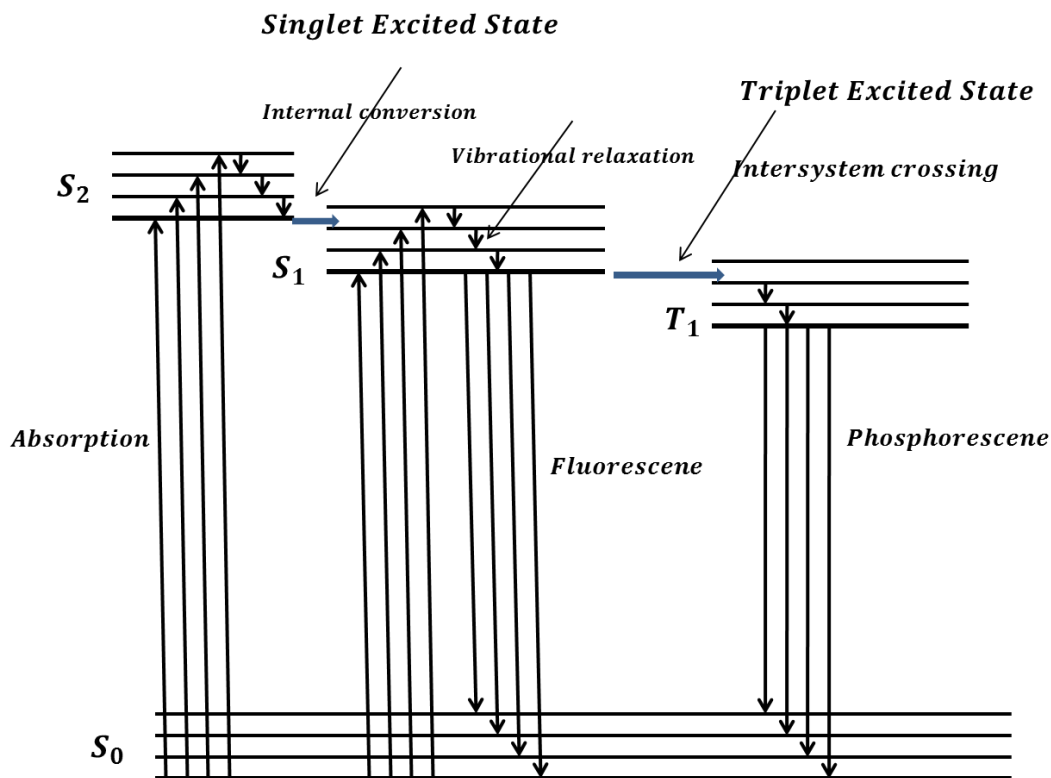


Figure 3-17. The Jablonski diagram for electronic transitions in different energy states. Diagram redrawn from Ref. 29²⁹.

The processes of light emission and absorption between electronic states of a molecule are usually illustrated by Jablonski diagrams as shown in Figure 3-17, named after Alexander Jablonski, the father of fluorescence spectroscopy. In the diagram, the electronic states are grouped by spin multiplicity with height of the line representing different energy values. S_0 , S_1 and S_2 are three different electronic levels of singlet states

and T₁ indicates the first triplet state; each set of these states is split into different vibrational levels and the ground states of each energy set are depicted by bold lines. The emission usually happens from S₀ ground state to some higher vibrational level of either S₁ or S₂. These excited states will rapidly relax to the ground level of S₁ or S₂ state. This process is called vibrational relaxation. The energy change of the relaxation will be transfer to the molecule vibration and finally be lost as heat. The vibrational relaxation happens very fast ($<10^{-12}$ s)³⁰ and usually occurs prior to fluorescent emission. Due to the relaxation of the excess vibrational energy, the wavelength of the emitted light will usually be longer than the absorbed light and will show in the spectra as a Stokes shift. Molecules in the S₁ state can also undergo a spin conversion to the first triplet state T₁ through intersystem crossing if the vibrational levels of these two electronic states overlap. Transitions between T₁ to S₁ are forbidden and have a much smaller emission rate as well as a slower decay scale. Table 3-3 shows some transfer rates for electronic processes.

Energy transfer	Rate (seconds)
Absorption	10^{-15} to 10^{-14}
Fluorescent emission	10^{-10} to 10^{-5}
Phosphorescent emission	10^{-4} to hours
Vibrational relaxation	$<10^{-12}$

Table 3-3. Energy transfer rate for difference electronic processes. Diagram rearranged from³¹.

3.7 Optical Spectrum

3.7.1 Solar Radiation and the Solar Spectrum

The solar spectral distribution outside the earth is called the Air Mass Zero or AM0, its power density is integrated over the whole spectrum and is around 1.3661kW/m²; after the sun light passes through the earth's atmosphere, due to the scattering and absorption effect by molecules in the atmosphere, the sunlight will be diffused and attenuated. The standard solar spectrum used to simulate the real solar spectrum and characterize photovoltaics is called the AM1.5, of which the power intensity corresponds to 1000W/m². Figure 3-18 shows the spectrum for AM0, AM1.5 and black body radiation. The top axis in the graph is the photon energy calculated through the wavelength of the light by Planck's law

$$E = \frac{hc}{\lambda} \quad (3.7.1)$$

3.7.2 Black Body Radiation

The black body radiation is the electromagnetic radiation emitted by an opaque or non-reflective body at a certain temperature in thermodynamic equilibrium with the environment. Max Planck derived a mathematical expression to describe the energy density distribution of the radiation in 1900, written as³²

$$E(\lambda, T) = \frac{2\pi hc^2}{\lambda^5 [\exp\left(\frac{hc}{\lambda k_B T}\right) - 1]} \quad (3.7.2)$$

where k_B the Boltzmann's constant; λ is the wavelength and $E(\lambda, T)$ is the energy distribution per unit area per unit wavelength. The total emissive power is obtained by the integration of this energy distribution over the whole spectrum from 0 to infinity yields

$$E = \sigma T^4 \quad (3.7.3)$$

where σ is the Stefan-Boltzmann constant; E is the emission energy per unit area. The solar spectrum AM0 can be well simulated by the black body radiation at 6000K. The black body radiation spectrum can be seen in Figure 3-18.

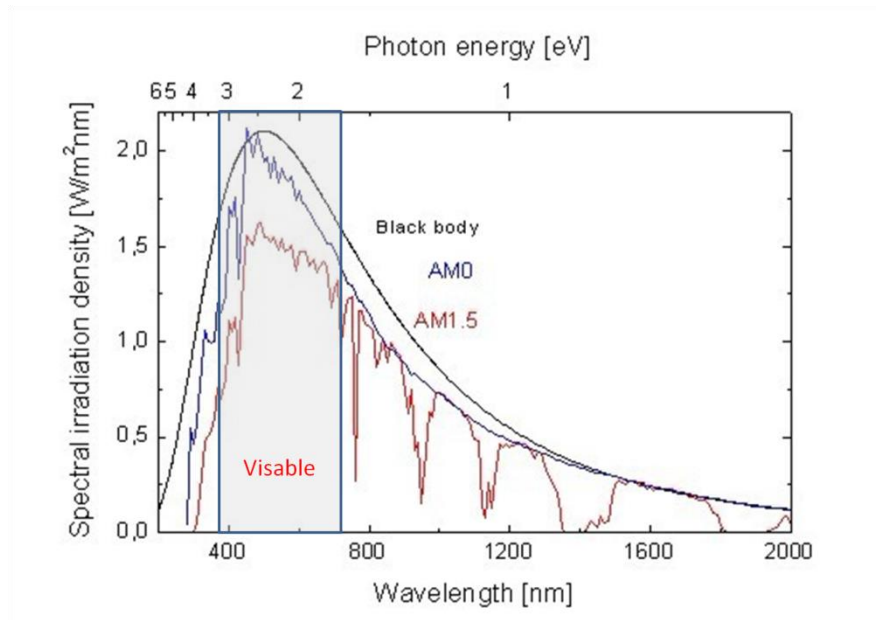


Figure 3-18. Comparison of spectral irradiation densities for black body radiation (black line), AM0 irradiation (red line) and AM 1.5 irradiation (blue line). Diagram modified from³³.

3.8 Organic Photovoltaic Operation

The working mechanism of photovoltaics is to capture light and transform it into electricity. The entire process can be divided into five sequential steps:

1. Light absorption in the photoactive layer and generation of a singlet exciton. The efficiency of this step η_A is defined as the proportion of the photons absorbed by the device to the incident photons shining on the device. The absorption rate for the incident photon with energy smaller than the band gap of the conjugating semiconductor is 0.
2. The exciton diffuses to the interface of donor and acceptor material. Diffusion efficiency is defined as η_{DF} , and is the proportion of excitons transferred to the interfaces of donor/acceptor material before recombination. This parameter is closely related to exciton diffusion length and lifetime.
3. The exciton dissociates into a free electron and hole at the interface of donor and acceptor material driven by the potential difference on HOMO/LUMO energy band of the two conjugating materials. The efficiency of exciton dissociation η_{DS} is related the number of excitons successfully disassociated to electrons/holes at the interfaces. A well matched donor/acceptor energy band will lead to high dissociation efficiency.
4. Charge carriers travel through junctions towards electrodes. The corresponding charge transfer efficiency η_{CT} links to the crystallinity and electronic properties of the conjugating polymer.
5. Charge carriers are collected at the electrodes. The charge collection efficiency η_{CC} relates to how well the band level matches between electrodes and the contacting polymer layer. The whole procedure is shown in Figure 3-19.

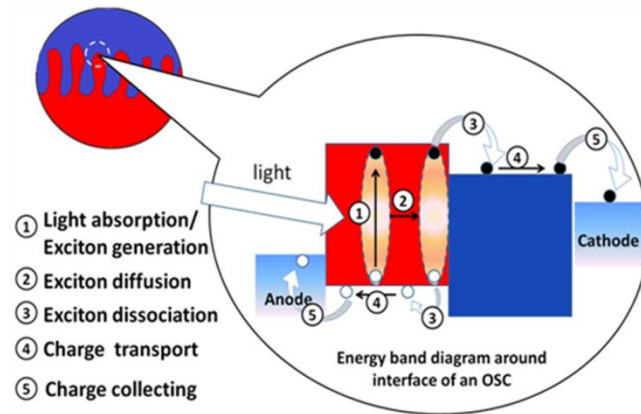


Figure 3-19. Schematic drawing of the five sequential steps converting light into photocurrent. Diagram redrawn from Ref. 34³⁴.

The external quantum efficiency (EQE) is defined as the ratio of the number of charges collected by the electrodes to the number of photons shining on the device of a particular wavelength. Written as

$$\eta_{EQE} = \frac{\text{electrons/sec}}{\text{photons/sec}} \quad (3.8.1)$$

At some wavelength with the photon energy more than twice the band energy the EQE might be greater than 100%; while at other wavelength where photon energy is lower than band energy the EQE is 0. The device's EQE is integrated over the whole solar spectrum. The EQE will drop from the ideal value due to recombination effects when the charge carriers are not able to form an external circuit, and it is calculated as³⁵

$$\eta_{EQE} = \eta_A \eta_{DF} \eta_{DS} \eta_{CT} \eta_{CC} \quad (3.8.2)$$

It can also be written as

$$\eta_{EQE} = \eta_A \eta_{IQE} \quad (3.8.3)$$

where η_{IQE} is the internal quantum efficiency (IQE), which can be obtained from the EQE by only considering the light already absorbed into the device. It is the ratio of the number of charges collected by the electrodes to the number of photons absorbed by the device and can be calculated by correcting EQE with transmission and reflection of the photovoltaic cell. The concept of quantum efficiency is also helpful in analyzing properties among different photodiodes.

3.8.1 Transport Equations in Solar Cells³⁶

There are two kinds of motion in the semiconductor for charges—drift and diffusion. Drift is the motion caused by an electric field. When an applied field is added onto a uniformly doped semiconductor, the energy band of the semiconductor will bend upward in the direction of the applied electric field. The electrons will move toward the direction with higher electric potential while the holes heading the opposite way. The drift velocity is proportional to the electric field as

$$v_d = \mu E = \mu \nabla \phi \quad (3.8.4)$$

in which μ is the carrier mobility and ϕ is the electrostatic potential. The current densities then can be written as

$$J_p^{drift} = qp v_{d,p} = qp \mu_p E = qp \mu_p \nabla \phi \quad (3.8.5)$$

and

$$J_n^{drift} = qnv_{d,n} = qn\mu_n E = qn\mu_n \nabla\phi \quad (3.8.6)$$

p and n in the equation represent the hole and electron density, respectively. v is the carrier moving velocity.

If the charge carriers move from the region of high to low concentration by random thermal motion, it is called diffusion. The diffusion current densities can be written as

$$J_p^{diff} = -qD_p \nabla p \quad (3.8.7)$$

and

$$J_n^{diff} = qD_n \nabla n \quad (3.8.8)$$

where D_n and D_p are the electron and hole diffusion coefficients, respectively. If we apply the Einstein-Smoluchowski relation for Brownian motion of

$$D = \frac{k_B \mu T}{q} \quad (3.8.9)$$

We then get the total hole and electron currents as

$$J_p = J_p^{drift} + J_p^{diff} = qp\mu_p \nabla\phi - k_B \mu_p T \nabla p \quad (3.8.10)$$

and

$$J_n = J_n^{drift} + J_n^{diff} = qn\mu_n \nabla\phi + k_B \mu_n T \nabla n \quad (3.8.11)$$

When the equilibrium status is achieved, the hole and electron current density is 0. This corresponds to the situation in a photovoltaic device when the external electric field reaches the open circuit voltage (V_{OC}) and the current is 0.

The built in voltage V_{bi} may be calculated as

$$\int_{-x_p}^{x_N} E dx = - \int_{-x_p}^{x_N} \frac{d\phi}{dx} dx = \phi(-x_p) - \phi(x_N) = V_{bi} \quad (3.8.12)$$

where x_N and x_p are the positions at the edge of depletion region in acceptor and donor material, respectively; V_{bi} is the built in voltage. If we replace E with the expression from Equation (3.8.10) and use $J_p = 0$ we get

$$E = \frac{k_B T}{q} \frac{1}{p_0} \frac{dp_0}{dx} \quad (3.8.13)$$

where p_0 is the hole density at equilibrium. Under illumination we include the photogenerated voltage V then the built in voltage may be expressed as

$$\begin{aligned} V - V_{bi} &= - \int_{-x_p}^{x_N} E dx = - \int_{-x_p}^{x_N} \frac{k_B T}{q} \frac{1}{p} \frac{dp}{dx} dx \\ &= - \frac{k_B T}{q} \int_{p_0(-x_p)}^{p_0(x_N)} \frac{dp_0}{p_0} \\ &= - \frac{k_B T}{q} \ln \left[\frac{p_0(x_N)}{p_0(-x_p)} \right] \end{aligned} \quad (3.8.14)$$

Using

$$p_0(x_N) = n_i^2/n \quad (3.8.15)$$

$$p_0(-x_p) = p \quad (3.8.16)$$

then

$$V = V_{bi} - \frac{k_B T}{q} \ln \left[\frac{np}{n_i^2} \right] \quad (3.8.17)$$

Equation (3.8.17) shows the how charge carriers affect the photovoltage generated in photovoltaic device.

3.8.2 Series and Shunt Resistance in OPV Devices

The parasitic resistance mainly affects the fill factor (FF) as well as the efficiency of the photovoltaic. The equivalent series resistance (R_s) refers to different factors that reduce the net charge reaching electrodes such as low charge carrier mobility and short exciton diffusion length. It is the sum of the resistances due to all the components that come in the path of the current, including the resistance in photo-generation layer, the organic layer/electrode contact and the electrodes. The equivalent shunt resistance (R_{sh}) refers to the leakage current in the device that is not generated through the photovoltaic effect. The leakage can occur through charge tunneling when the two electrodes stay too close or the electrodes are connected through a direct/indirect conducting path. In order to maximize the FF in the device, it is desirable to have the values of R_s to be as low as possible while R_{sh} the higher the better. The effect of the R_s and R_{sh} on the performance of the photovoltaic device are shown in Figure 3-20.

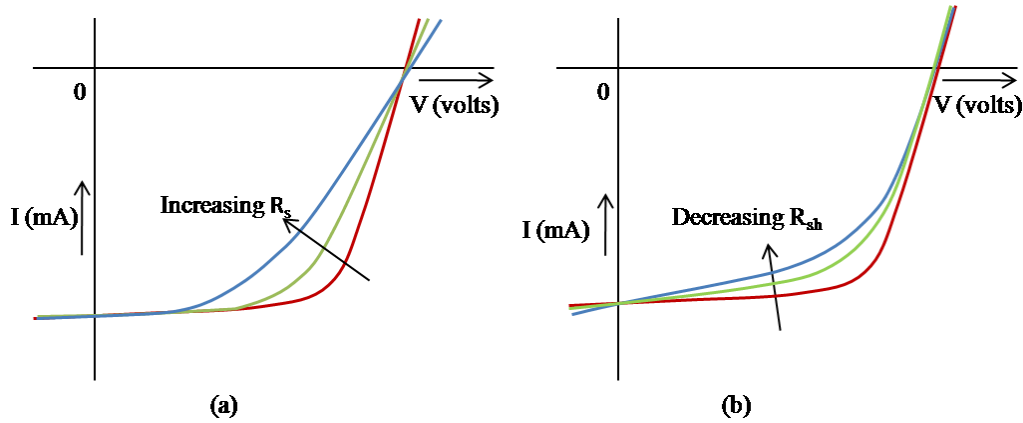


Figure 3-20. The effect of changing a) R_s and b) R_{sh} on an illuminated photovoltaic device. Diagram redrawn from Ref. 34 ³⁴.

Since the effect of R_s is negligible near open circuit conditions, the slope of the IV curve around that region will indicate the value of R_{sh} . Applying Lambert's W function and after some simplification, one can get the expression³⁷ of R_{sh} as

$$\frac{dV}{dI} \Big|_{I=I_{sc}, V=0} \approx R_{sh} \quad (3.8.18)$$

Similarly, the slope at short circuit current (J_{sc}) refers to the value of R_s as

$$\frac{dV}{dI} \Big|_{I=0, V=V_{oc}} \approx R_s \quad (3.8.19)$$

Figure 3-20 shows the IV curve under the effect of changing R_s and R_{sh} values. There are numerous methods developed to calculate the value of R_s and R_{sh} with more precision, which can be extracted by simulating the IV curve either with³⁷ or without illumination³⁸.

3.8.3 Current-Voltage Characteristics

3.8.3.1 Equivalent Circuits and Resistance

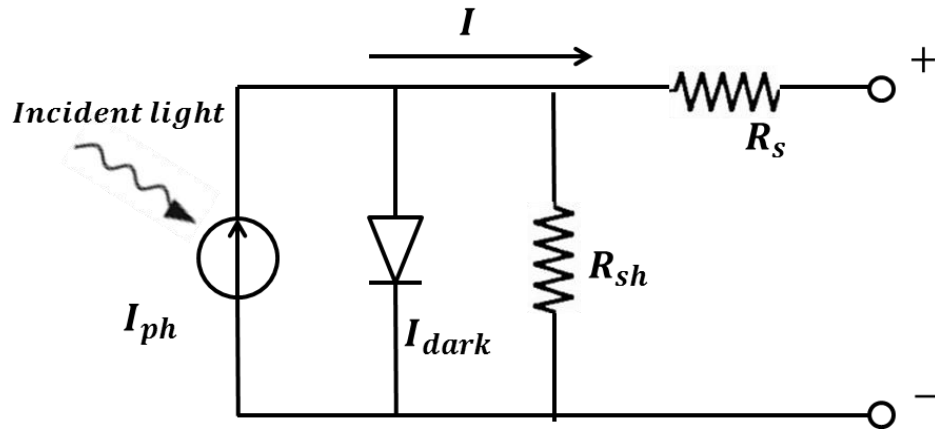


Figure 3-21. Equivalent circuit of a p-n junction solar cell. Diagram redrawn from Ref. 34³⁴

In the dark, the photovoltaic device may be considered as a standard diode. While under illumination, it can be modeled as a current source with the current density proportional to the solar irradiation intensity falling on it. Thus for an ideal photovoltaic the current source and the diode are connected in parallel, with the direction of the current in the two components pointing in the opposite direction. However, for a practical photovoltaic device, optical and electrical losses exist in the system. The R_s and R_{sh} are incorporated the equivalent circuit diagram shown in Figure 3-21.

3.8.3.2 I-V Characteristics for the Solar Photovoltaic Device

From the equivalent circuit we can write out the net current flow through the photovoltaic

\vec{I} as

$$I = I_P - I_D I_{sh} \quad (3.8.20)$$

where I_P is the photogenerated current; I_D is the diode current and I_{sh} is the shunt current. We define the direction of photocurrent as positive. And the voltage across the output terminal V is expressed as

$$V = V_j + IR_s \quad (3.8.21)$$

where V_j is the voltage across both diode and the shunt resistor R_{sh} . The Shockley diode equation is used to give the characteristic of an ideal diode and it is written as

$$I_D = I_0 \left[\exp\left(\frac{qV_j}{nkT}\right) - 1 \right] \quad (3.8.22)$$

where I_0 is the reverse saturation current caused by the diffusion of minority carriers from neutral regions to the depletion, it is in the reverse direction of diode built in voltage and is almost independent of the reverse voltage³⁹; n is the diode ideal factor; k is the Boltzmann's constant and T is the temperature. At room temperature $T = 25^\circ\text{C}$, $\frac{kT}{q} \approx 0.0259\text{V}$. The reverse saturated current is given by³⁹

$$I_0 = I_{oh} + I_{oe} = A \left(\frac{qn_i^2}{p} v_{dh} f_h + \frac{qn_i^2}{n} v_{de} f_e \right) \quad (3.8.23)$$

where v_{dh} and v_{de} are the hole and electron diffusion velocity, respectively; f_h and f_e are hyperbolic functions of the recombination velocities, diffusion length and the undepleted n and p layer thicknesses; A is the device area.

The photogenerated current can be written as⁴⁰

$$I_P = A \int_0^\infty qF(\lambda)[1 - r(\lambda)]IQE(\lambda)d\lambda \quad (3.8.24)$$

where $F(\lambda)$ is the photon flux density of the incident light; $r(\lambda)$ is the light reflectivity of the material at wavelength λ ; $IQE(\lambda)$ is the internal quantum efficiency.

The current flow through the shunt resistor R_{sh} can be written out using ohm's law as

$$I_{sh} = \frac{V_j}{R_{sh}} = \frac{V - IR_s}{R_{sh}} \quad (3.8.25)$$

Applying the Shockley diode equation and the shunt current into the net current density equation, then

$$I = I_p - I_0 \left[\exp\left(\frac{q(V - IR_s)}{nkT}\right) - 1 \right] + \frac{V - IR_s}{R_{sh}} \quad (3.8.26)$$

This equation involves I on both sides and the parameters of I_0 , n and resistance can't be measured directly, however, those parameters may be calculated using numerical methods after some simplification under certain conditions.

Open circuit condition: $I = 0$, the voltage across the output terminal is called the V_{oc} , for an ideal cell

$$V_{oc} \approx \frac{nkT}{q} \ln\left(\frac{I_p}{I_0} + 1\right) \quad (3.8.27)$$

Short circuit condition: $V = 0$, the current flow through the output terminal is called the I_{sc} , assume it is an ideal cell, we can write

$$I_{sc} \approx I_p \quad (3.8.28)$$

3.9 Characterization and Principle Parameters

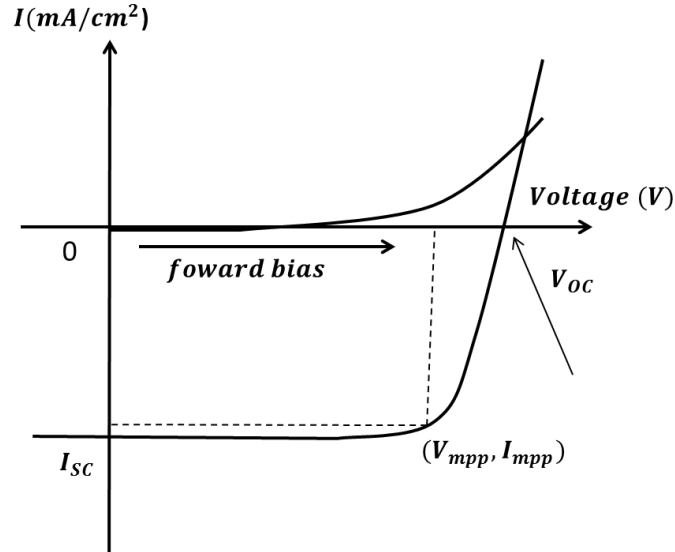


Figure 3-22. I-V characteristic curve of an OPV device displaying the principle parameters.

The IV curve of a diode is a typical way to characterize the performance of a solar device which is shown in Figure 3-22. On the curve with illumination, principle parameters are marked such as short circuit current density (J_{sc}), V_{oc} and the point with maximum power output (J_{mpp} , V_{mpp}). The FF is a key parameter in evaluating the performance of the solar cells, and it is defined as the ratio of the maximum power output to the product of the J_{sc} and the V_{oc}

$$FF = \frac{J_{mpp} \times V_{mpp}}{J_{sc} \times V_{oc}} \quad (3.9.1)$$

A high FF indicates a low R_s and a R_{sh} close to infinity, in this way there will be less energy loss inside the device. The variation in FF can be significant with photovoltaic

devices fabricated using different materials: the inorganic commercial solar cells usually have a $FF > 0.7$, such as a GaAs cell with a FF approaching 0.89; while for OPVs the FF is usually around 0.4 – 0.6.

The most important parameter for measuring performance is called the power conversion efficiency (PCE), which is the percentage of power that can be extracted for a given amount incident light. It can be calculated with the ratio of maximum power output to the incident optical power as

$$\eta_{PCE} = \frac{P_{out}}{P_{in}} = FF \frac{J_{SC} V_{OC}}{P_{in}} \quad (3.9.2)$$

3.10 Electron-Hole Pair Generation and Photocurrent

3.10.1 Photo-generation Rate

When light with photon energy larger than the band gap of the semiconductor is shining on the material, the electron will be excited to from the VB to the CB, leaving a hole behind. The creation of the electron-hole pair through this process is called the fundamental absorption and is the most essential to the operation of the photovoltaic device. The extra photon energy that is not large enough for excitation or exceeds the band gap will be transferred to charge momentum or crystal momentum through scattering.

A macroscopic absorption coefficient $\alpha(E,x)$ is used to describe how the light intensity is attenuated through the material. For example, a beam of photons with energy E and intensity I_0 pass through a certain material, a fraction of the light intensity $I(x)$ will be absorbed with a factor of $e^{-\alpha(E,x)dx}$

$$\frac{dI}{dx} = -\alpha(E,x)I \quad (3.10.1)$$

Integrating over the depth x of the material with a non-uniform $\alpha(E,x)$ yields⁹

$$I(x) = I(0) e^{-\int_0^x \alpha(E,x')dx'} \quad (3.10.2)$$

where $I(x)$ and $I(0)$ are the light intensity at depth of x and the surface of the material, respectively. For uniform α , Equation (3.10.2) reduces to the Beer-Lambert law

$$I(x) = I(0) e^{-\alpha x} \quad (3.10.3)$$

The α here will be the imaginary part of the refractive index $Im(n_s)$ with a relationship of

$$\alpha = \frac{4\pi Im(n_s)}{\lambda} \quad (3.10.4)$$

where λ is the wavelength of the incident light; n_s is the refractive index of the material. Because the photo-generation rate is determined by the number of the photons absorbed instead of the energy of the photons, the generation rate can be written as the product of the photon flux at a certain depth and the absorption rate as

$$g(E,x) = (1 - R(E))\alpha(E,x)b_s(E)e^{-\int_0^x \alpha(E,x')dx'} \quad (3.10.5)$$

where $R(E)$ is the reflectivity and $b_s(E)$ the incident flux at the surface of the material. The total generation rate at depth x can be calculated by summing over the photon energies as

$$G(x) = \int_0^{\infty} g(E, x) dE \quad (3.10.6)$$

The charge carrier will be mainly generated through band to band, although there are also other types of generation processes as trap-assisted generation and Auger generation. The charge recombination is an inverse of the generation process, and it is symbolized by R . The continuity equation for the charge carriers in the device will is given by

$$\frac{\partial n}{\partial t} = \frac{1}{q} \nabla \cdot \vec{J}_n + (G_n - R_n) \quad (3.10.7)$$

and

$$\frac{\partial p}{\partial t} = \frac{1}{q} \nabla \cdot \vec{J}_p + (G_p - R_p) \quad (3.10.8)$$

where p and n are the carrier densities and J_p and J_n are current densities of holes and electrons, respectively.

3.10.2 Carrier Generation by Thermal Excitation

When temperature is at absolute zero, the electrons in the material occupy the energy levels up to the Fermi level, and no thermal excitation will occur. As the temperature increases, the molecules in the material start to gain some vibrational kinetic energy and part of which will be passed to the electrons, promoting them to a higher energy level. The excitation of the electron in this way is called thermal generation. In thermal equilibrium, the rate of thermal generation $G_{n/p}^{th}$ should balance with the rate of the thermal recombination rate $R_{n/p}^{th}$ as

$$G_{n/p}^{th} = R_{n/p}^{th} \quad (3.10.9)$$

The thermal energy kT ($\sim 0.0256\text{eV}$), at room temperature, will be much smaller than the band gap energy of the semiconductor which is in the scale of 0.1eV to 3eV , thus it is very difficult to produce charge carriers in the semiconductor by thermal generation and it will not be considered as a contribution to the generation rate.

3.11 Charge Recombination

3.11.1 Recombination Mechanisms

Recombination is an exact inverse process of carrier generation. The electrons in the CB combine with holes in the VB. Non-radiative recombination is the case when the energy is given off through heat or to other electrons and radiative recombination is where the energy is emitted in the form of photons. There are mainly three kinds of recombination.

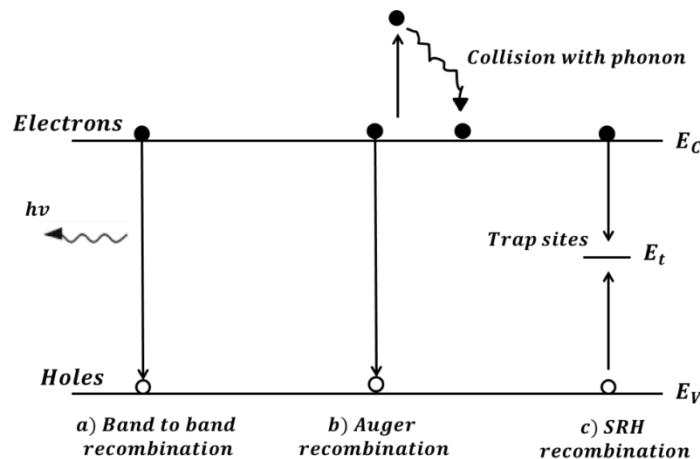


Figure 3-23. Various carrier recombination mechanisms in solar photovoltaics. Diagram redrawn from Ref. 34 ³⁴.

3.11.1.1 Band to Band Recombination⁹

Band to band recombination is the process in which the electron combines with a hole in a lower energy band and they are said to annihilate each other with the emission of a photon; it is the exact reverse of the radiative absorption process. Band to band recombination resulting from optical generation of the spontaneous and stimulated emission is an unavoidable process due to the essential physical process in the semiconductor. Using Langevin recombination, the recombination rate is expressed as

$$R_{rad} = \gamma(np - n_i^2) \quad (3.11.1)$$

in which n and p are the charge carrier densities for electron and hole, respectively. γ is the Langevin prefactor

$$\gamma = \frac{q}{\epsilon}(\mu_n + \mu_p) \quad (3.11.2)$$

where ϵ is the material dielectric constant; μ_n and μ_p are the electron and hole mobility, respectively; n_i is the intrinsic charge density.

3.11.1.2 Auger recombination

Auger recombination is the process in which the energy released during a band to band recombination is transferred to an electron or hole as kinetic energy which is then subsequently lost to the lattice through collisions with phonons as shown in Figure 3-23 (b). It is a non-radiative recombination process as the energy is not released as photons. In Auger process, an electron with two holes or two electrons with one hole are involved, thus in analogy with the expression used in the band to band recombination, Auger recombination rate involved with two electrons and one hole can be written as

$$R_{Auger} = A_p(n^2p - n_0^2p_0) \quad (3.11.3)$$

For the recombination involved with two holes and one electron

$$R_{Auger} = A_n(np^2 - p_0^2n_0) \quad (3.11.4)$$

where n_0 and p_0 are the majority electron and hole densities in equilibrium; A_p and A_n are the recombination coefficients; and we have used mass action law

$$n_0p_0 = n_i^2 = npe^{\Delta\mu/k_B T} \quad (3.11.5)$$

3.11.1.3 Shockley-Read-Hall recombination

Trap assisted recombination, also referred to as Shockley-Read-Hall (SRH) recombination occurs when the electrons/holes fall into a trap generated by the impurities in the semiconductor as shown in Figure 3-23 (c). The energy level of this impurity traps stays in-between the band gap. The recombination process will be completed when a charge with opposite polarity jumps into the trap before the first carrier is released.

The recombination rate in this case will be mainly affected by the impurity. Suppose we have a semiconductor with a trap density N_t and the energy state of the trap is E_t , the SRH recombination rate can be written as

$$R_{SRH} = \frac{np - n_i^2}{\tau_{n,SRH}(p + p_t) + \tau_{p,SRH}(n + n_t)} \quad (3.11.6)$$

The auxiliary variables p_t and n_t are the densities when the charge carrier (holes/electrons) Fermi level is equal to the trap level as

$$p_t = n_i e^{(E_i - E_t)/k_B T} \quad (3.11.7)$$

and

$$n_t = p_i e^{(E_t - E_i)/k_B T} \quad (3.11.8)$$

E_i is the quasi-Fermi level in the semiconductor; $\tau_{n,SRH}$ and $\tau_{p,SRH}$ are the electron and hole lifetime captured in the trap, respectively. They are defined as

$$\tau_{n,SRH} = \frac{1}{B_n N_t} \quad (3.11.9)$$

$$\tau_{p,SRH} = \frac{1}{B_p N_t} \quad (3.11.10)$$

B_n and B_p are the recombination coefficient for electrons and holes in the trap, respectively. In a semiconductor with one carrier density far more excess to the other carrier density, the simplified expression is

$$R_{SRH} = B_n N_t (n - n_0) \quad (3.11.11)$$

for the p type material and

$$R_{SRH} = B_p N_t (p - p_0) \quad (3.11.12)$$

for the n type material. In the one carrier dominant semiconductor the recombination rate will be affected mainly by the trap and the minority carrier density. However, the SRH recombination will be largest when the two charge carrier densities are of the same magnitude.

3.11.1.4 Surface Recombination

Recombination at interfaces and surfaces has a significant impact on the recombination as defects are more likely to occur in those areas. At surface areas the neighboring atoms are no longer continuous and impurity molecules such as oxygen or water molecules are attached, causing a large amount of trap sites; also at interfaces between different crystal regions, crystal defects due to broken bonds or extrinsic impurities are found. The surface recombination can be treated the same way as SRH recombination, only instead of using densities per unit volume, in surface recombination we discuss with densities per unit area.

3.12 Interface and Band Alignment

3.12.1 Interfacial Electronic Structure inside an Organic Solid

The band energy structures in the organic molecules discussed in the previous sections are assumed to be parabolic, in which various atomic molecules are formed. The electrons in the potential well occupy up to the HOMO level. When carbon atoms are linked together to form a polymer chain, the deep AOs stay in that potential-well while the ones in the upper part merge to form a MO. The electrons in the MOs can delocalize over the whole π conjugating system as shown in Figure 3-24(b). When the polymer molecules are put together to form a polymer crystal, the molecules will interact with each other by the weak van der Waals force, merging the very upper levels of the MOs while the lower HOMO and LUMO levels will still stay in each polymer chain, as seen in Figure 3-24(c).

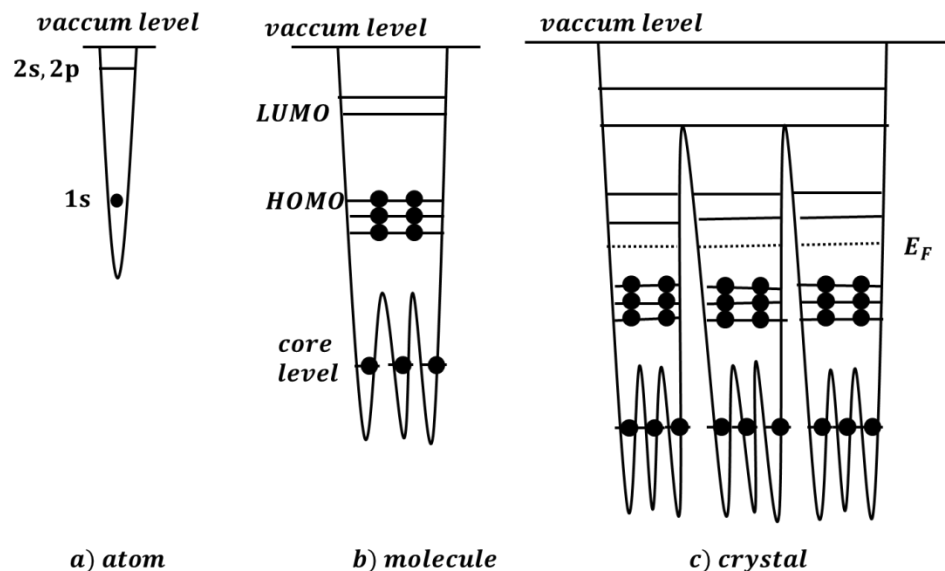


Figure 3-24. Electronic structure represented with potential wells for a) atom; b) polyatomic molecule; c) Organic solid. Diagram redrawn from Ref. 41⁴¹.

3.12.2 Parameters Related to the Interfacial Electronic Structure

A simplified diagram for electronic structure is shown in Figure 3-25. The top most level of the potential well will be called the vacuum level (VL); the energy separation from the LUMO level to the VL is called the electron affinity (A_g), defined as the amount of energy released when an electron is added to a neutral atom or molecules to form a negative ion; the energy separation from the HOMO level to the VL is the gas phase ionization energy (I_g), which is the energy required to remove an electron from the atom or molecule into the gaseous state; the work function ϕ is defined as the energy required in removing the least tightly bound electron, and is the energy difference between the VL and the Fermi energy as

$$\phi_W = E_{vac} - E_F \quad (3.12.1)$$

where E_{vac} represents the VL. The techniques commonly used in measuring the I_g are UV photoemission spectroscopy (UPS) and photoemission yield spectroscopy (PEYS), for which the UPS is a more powerful technique as it is capable of examining the full details of the interfacial electronic structures including the vacuum level shift at the interface; while in PEYS a common VL is always assumed⁴¹. The value of the A_g is usually determined from the value of I_g and the value of band gap deduced from the optical measurements.

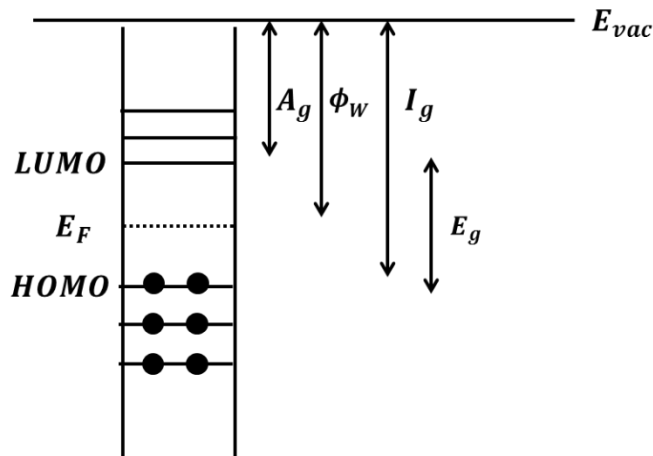


Figure 3-25. Electronic structure in an organic solid for the representation of basic parameters.

Diagram redrawn from Ref. 41⁴¹.

3.12.3 Current Flow at Junction Interfaces

From the discussion in previous sections, the relationship between the quasi-Fermi levels and the carrier density is

$$n = N_C \exp\left(\frac{E_{F_n} - E_C}{k_B T}\right) \quad (3.12.2)$$

$$p = N_V \exp\left(\frac{E_V - E_{F_p}}{k_B T}\right) \quad (3.12.3)$$

If we differentiate on both sides of the two equations we can get the expressions for the gradient of the quasi-Fermi levels as⁹

$$\nabla E_{F_n} = (\nabla E_C - kT \nabla \ln N_C) + \frac{k_B T}{n} \nabla n \quad (3.12.4)$$

$$\nabla E_{F_p} = (\nabla E_V + kT \nabla \ln N_V) - \frac{k_B T}{p} \nabla p \quad (3.12.5)$$

Examining the band structures, the Fermi levels may be rewritten with parameters that can be measured experimentally as V_L , A_g and I_g

$$E_C = E_{vac} - A_g \quad (3.12.6)$$

$$E_V = E_{vac} - I_g \quad (3.12.7)$$

After differentiation on both sides

$$\nabla E_C = \nabla E_{vac} - \nabla A_g \quad (3.12.8)$$

$$\nabla E_V = \nabla E_{vac} - \nabla I_g \quad (3.12.9)$$

Thus, putting the gradient of the conduction energy and valence energy back to Equation (3.12.4) and (3.12.5) the gradient of the quasi-Fermi level may be rewritten as

$$\nabla E_{F_n} = (\nabla E_{vac} - \nabla A_g - kT \nabla \ln N_C) + \frac{k_B T}{n} \nabla n \quad (3.12.10)$$

$$\nabla E_{F_p} = (\nabla E_{vac} - \nabla I_g + kT\nabla \ln N_V) - \frac{k_B T}{p} \nabla p \quad (3.12.11)$$

Placing Equation (3.12.2) and Equation (3.12.3) for electrons and holes into transport equation and then apply the above two equations yields

$$J_n(\mathbf{r}) = \mu_n n \nabla_r E_{F_n} \quad (3.12.12)$$

and

$$J_p(\mathbf{r}) = \mu_p p \nabla_r E_{F_p} \quad (3.12.13)$$

in which μ_n and μ_p are charge motilities for electrons and holes, respectively. The relations between the current flow and the energy band level as well as the electrostatic field are

$$J_n(\mathbf{r}) = \mu_n n (\nabla E_{vac} - \nabla A_g - k_B T \nabla \ln N_C) + q D_n \nabla n \quad (3.12.14)$$

and

$$J_p(\mathbf{r}) = \mu_p p (\nabla E_{vac} - \nabla I_g - k_B T \nabla \ln N_V) - q D_p \nabla p \quad (3.12.15)$$

For which the Einstein relations which relate mobility to the diffusion constant for both carriers have been applied

$$\mu_n = \frac{q D_n}{k_B T} \quad (3.12.16)$$

$$\mu_p = \frac{q D_p}{k_B T} \quad (3.12.17)$$

where D_n and D_p are the diffusion constants for electrons and holes, respectively. Thus the current flow between junctions are expressed using parameters that can be measured directly, the first part of the expression is related to the drift current caused by the electric

field and the second to diffusion current caused by concentration difference. We can see from the equations that at the junction interface, current flow will happen if there is a difference in: 1) vacuum levels of the two junction (or an external electrostatic field is applied); 2) electron affinity (for electrons) /ionization energy (for holes); 3) energy band gap between HOMO and LUMO; 4) charge densities. In conclusion, the electrons will tend to flow to lower energy levels and holes to higher levels.

3.12.4 Organic-Metal Interface

3.12.4.1 The Schottky Contact

3.12.4.1.1 Carrier Density and Band Bending in n-type Semiconductor and Metal

Junction

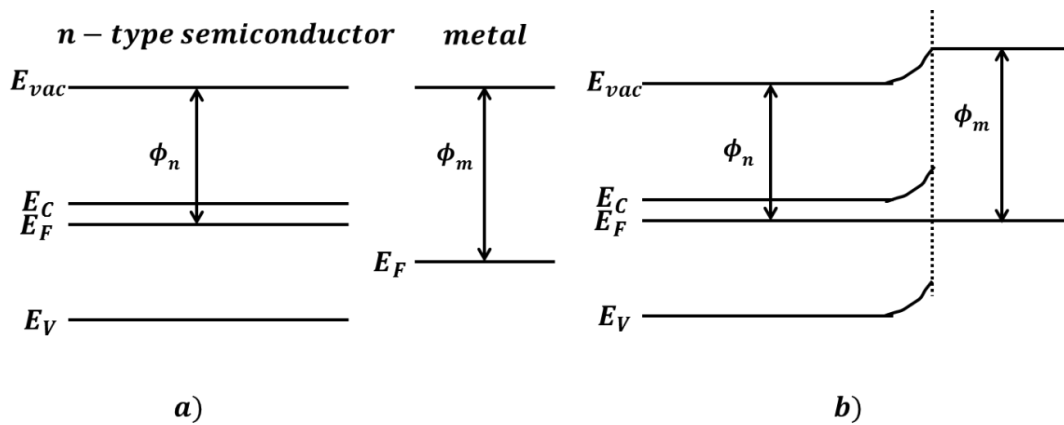


Figure 3-26. a) Band profiles of an n-type semiconductor and a metal in isolation; b) Band profile at the interface of an n-type semiconductor and metal for a Schottky contact. Diagram redrawn from Ref. 9⁹.

When an n-type semiconductor of work function ϕ_n and a metal of work function ϕ_m ($\phi_n < \phi_m$) are brought together, the Fermi levels of the two materials will line up (assuming the charge density in the semiconductor is high enough). At the interface the electrons will drift from the semiconductor to metal, leaving a layer of positive charges in the semiconductor and negative charges close to the metal side. After a dynamic equilibrium is reached, the Fermi levels line up and the VLS between them will have a

difference of $\phi_m - \phi_n$. A charge gradient builds up between the semiconductor and the metal and the band will start to bend in a way to prevent further charge flow.

The electrostatic field between the two neighboring materials, namely the built in voltage V_{bi} is equal to the difference of the VL (ΔE_{vac}) and is achieved by band bending, pointing from semiconductor to metal. As a result of the metal being a much better charge conductor than the semiconductor, most of the band bending due to the fall in potential remains in the semiconductor. The region of this drop in potential is called the space charge region.

The electron density outside the space-charge region is the same as when the semiconductor is electrically neutral; while inside the interface junction, the electron density gradually decreases as it gets closer to the metal, which causes the CB to increase relative to the Fermi level; and the hole density increases along the space charge region, causing the valence energy band to increase relative to the Fermi level. Here an assumption is taken such that the quasi-Fermi level will stay the same since the flow of the minority charge carriers will have little effect on charge densities. The holes in the semiconductor are mainly caused by the ionization of the electrons, and after equilibrium is achieved, the space charge region is depleted of carriers, so it is also called the depletion region.

3.12.4.2 Carrier density and band bending in p-type semiconductor and metal junction

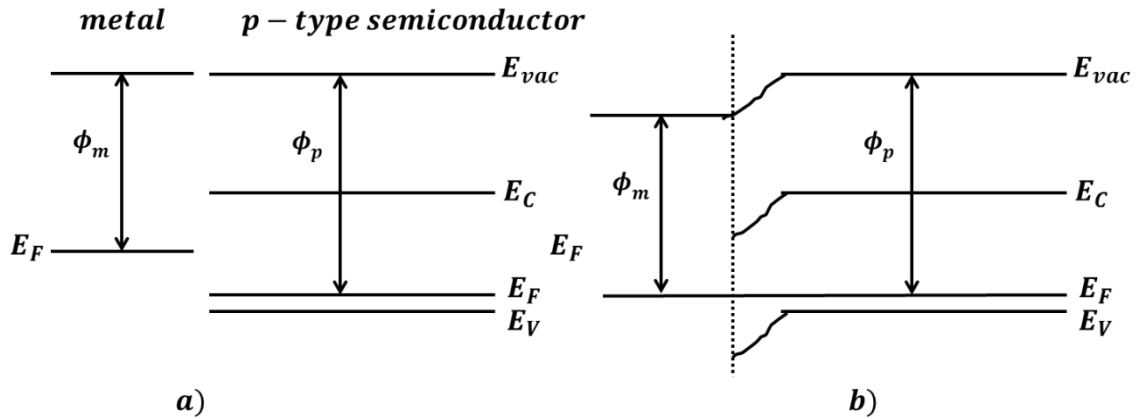


Figure 3-27. a) Band profiles of a metal and a p-type semiconductor in isolation; b) Band profile at the interface of a metal and an p-type semiconductor for a Schottky contact. Diagram redrawn from Ref. 9⁹.

When a p-type semiconductor with the work function of ϕ_p and a metal with the work function of ϕ_m ($\phi_p > \phi_m$) are put together, the situation is analogous with the previous case (assuming that the charge density in semiconductor is high enough). The Fermi-level gradient causes an electron flow in at the interface from metal to semiconductor. The redistribution of the charge carriers causes the band bending of the CB as well as the VB, as can see in Figure 3-27. The build in bias equals to the difference in the VL as well as the difference in work function of the two neighboring materials $\phi_p - \phi_m$.

In both situations discussed above, after the dynamic equilibrium is achieved, the energy bands at the interface bend in such a way that the electric bias encourages the transport of

minority carriers and inhibit the flow of majority carriers. This type of contact is called the Schottky contact.

3.12.4.3 The Ohmic Contact

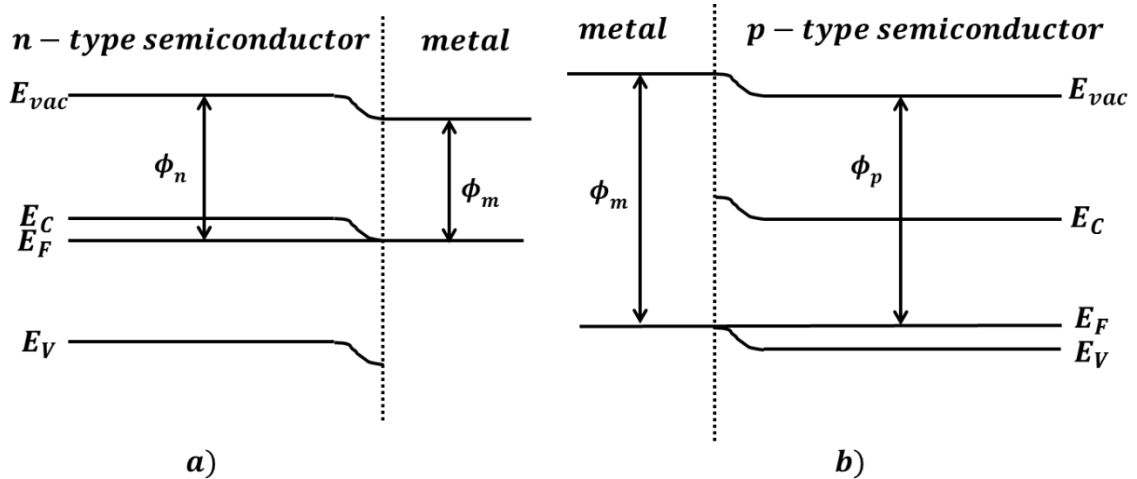


Figure 3-28. Band structure at the interface of a) an n-type semiconductor and a metal and b) a metal and a p-type semiconductor for an Ohmic contact. Diagram redrawn from Ref. 9⁹.

When a metal and n-type semiconductor with $\phi_n > \phi_m$, or if metal and p-type semiconductor with $\phi_p < \phi_m$ are put together, the situation will be different with that in Schottky contact. When equilibrium is reached, the majority carriers will have low resistance traveling across the interface while the minority carriers will be inhibited. The interface will accumulate a large amount of majority charge carriers for an Ohmic contact so the majority charge carriers can pass current easily in either direction. When the built in bias encourages the transport of the majority carries and inhibits the flow of the minority carriers, this type of the contact is called an Ohmic contact as presented in Figure 3-28.

3.12.5 Organic-Organic Interface

3.12.5.1 p-n Junction under Dark at Equilibrium

3.12.5.2 Establishing the Depletion Region

When p-type and n-type semiconductor are put together, the interface between these two types of semiconductor will form a p-n junction. The p-n junction was discovered by the American physicist Russell Ohl of Bell laboratories, and later it becomes the most fundamental and important component in most semiconductor electronic devices as transistors, photovoltaics, light emitting diodes (LED) and integrated circuits.

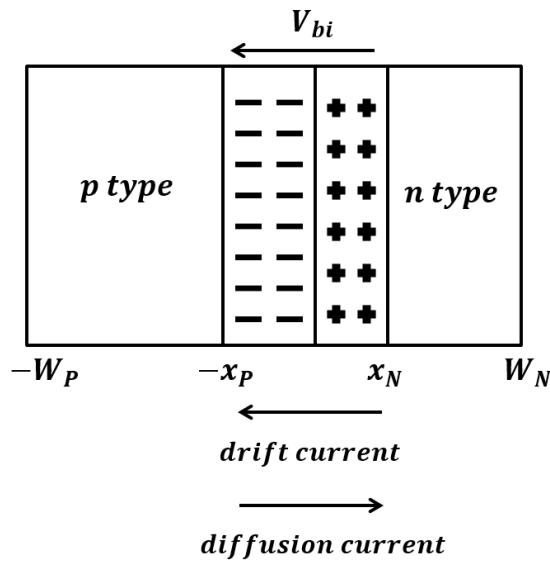


Figure 3-29. Schematic drawing for the formation of depletion region in a p-n junction.

The p-n junction consists of a p-type semiconductor with work function ϕ_p and an n-type semiconductor with the work function of ϕ_n such that $\phi_p > \phi_n$. The electrons will first diffuse from n-type to the p-type semiconductor. After equilibrium is reached, an electric

field is established at the interface junction with the bias $V_{bi} = \phi_p - \phi_n$, pointing from n-type to p-type material as shown in Figure 3-29. The built-in field encourages the flow for minority charges; thus, the electrons from p-type material will flow to n-type material and the holes travel in the opposite direction, and this is called the drift current. At the same time, due to the difference of the charge carrier concentration in these two materials, the majority carriers will diffuse to the low concentrated region overcoming the energy barrier of the built-in bias V_{bi} , and this results in the diffusion current. Due to the charge redistribution at the junction, positive charges will be accumulated on the n material side whilst negative on the p material side. The energy band bending at the p-n junction in both CB and VB can be seen in Figure 3-30.

An electrostatic equilibrium will be reached when carrier diffusion and drift motion balance out and the two Fermi levels in the two materials line up on the same level. This process will create a region with hardly any mobile carriers, called the depletion region. As shown in Figure 3-29, the depletion region extends from $x = -x_p$ to $x = x_n$.

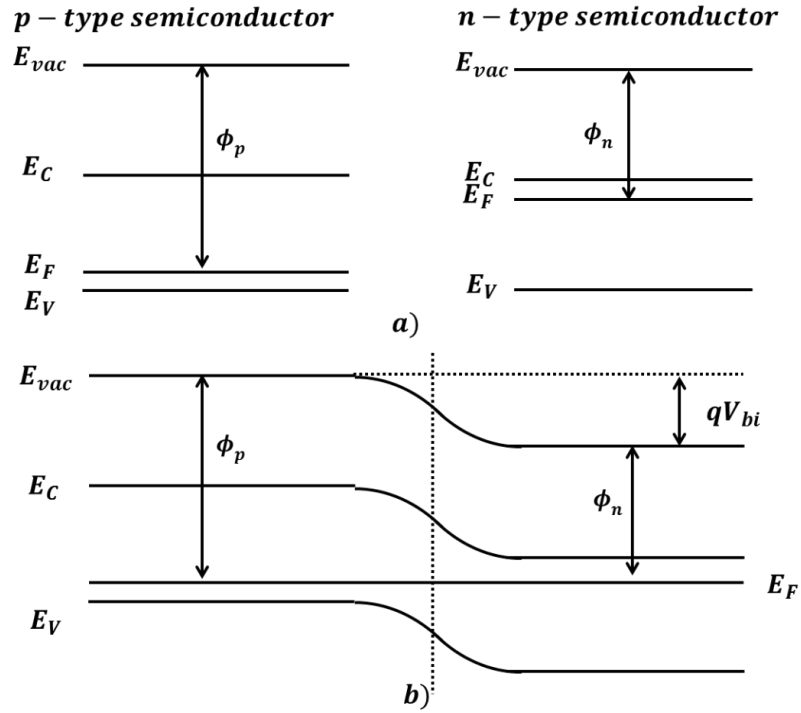


Figure 3-30. a) Band profiles of p-type and n-type semiconductor in isolation; b) Band profile of the p-n junction in equilibrium. Diagram redrawn from Ref. 9⁹.

3.12.5.3 Depletion Width^{9,10}

Using the parameters for the p-n junction structure in Figure 3-29, we apply the Poisson's equation in both types of the semiconductor

$$\frac{d^2\phi}{dx^2} = \frac{q}{\epsilon_p} p \quad \text{for } x < 0 \quad (3.12.18)$$

$$\frac{d^2\phi}{dx^2} = -\frac{q}{\epsilon_n} n \quad \text{for } x > 0 \quad (3.12.19)$$

where ε_p and ε_n are the permittivity for the p and n type semiconductor, respectively.

Using the boundary condition at the edge of the depletion region

$$\left. \frac{d\phi}{dx} \right|_{-w_p, w_n} = 0 \quad (3.12.20)$$

and then integrating on the Poisson's equation we get

$$\frac{d\phi}{dx} = \frac{qp}{\varepsilon_p}(x + w_p) \quad \text{for } -w_p < x < 0 \quad (3.12.21)$$

$$\frac{d\phi}{dx} = -\frac{qn}{\varepsilon_n}(x - w_n) \quad \text{for } 0 < x < w_n \quad (3.12.22)$$

At the edge of the depletion region, we set the electric potential to be 0 in p-material and it will be V_{bi} in the n-material as

$$\phi = 0 \quad \text{for } x = -w_p \quad (3.12.23)$$

$$\phi = V_{bi} \quad \text{for } x = w_n \quad (3.12.24)$$

Using this boundary condition and we integrate again on the one order differential equations above we can get

$$\phi = \frac{p}{2\varepsilon_p}(x + w_p)^2 \quad \text{for } -w_p < x < 0 \quad (3.12.25)$$

$$\phi = -\frac{n}{2\varepsilon_n}(x - w_n)^2 + V_{bi} \quad \text{for } 0 < x < w_n \quad (3.12.26)$$

At $x = 0$ the potential field ϕ and the electric field $-\frac{1}{q}\frac{d\phi}{dx}$ should be continuous, we use

this condition and solve for w_p and w_n as

$$w_p = \sqrt{\frac{2n\varepsilon_p^2 V_{bi}}{p(n\varepsilon_p + \varepsilon_n p)}} \quad (3.12.27)$$

$$w_n = \sqrt{\frac{2p\varepsilon_n^2 V_{bi}}{n(n\varepsilon_p + \varepsilon_n p)}} \quad (3.12.28)$$

Thus, the depletion width will be

$$w = w_p + w_n = \frac{\sqrt{2n^2\varepsilon_p^2 V_{bi}} + \sqrt{2p^2\varepsilon_n^2 V_{bi}}}{\sqrt{np(n\varepsilon_p + \varepsilon_n p)}} \quad (3.12.29)$$

where n and p are the majority carrier densities in the n-type and p-type materials, respectively.

3.12.6 p-n Junction under Forward Bias or under Illumination

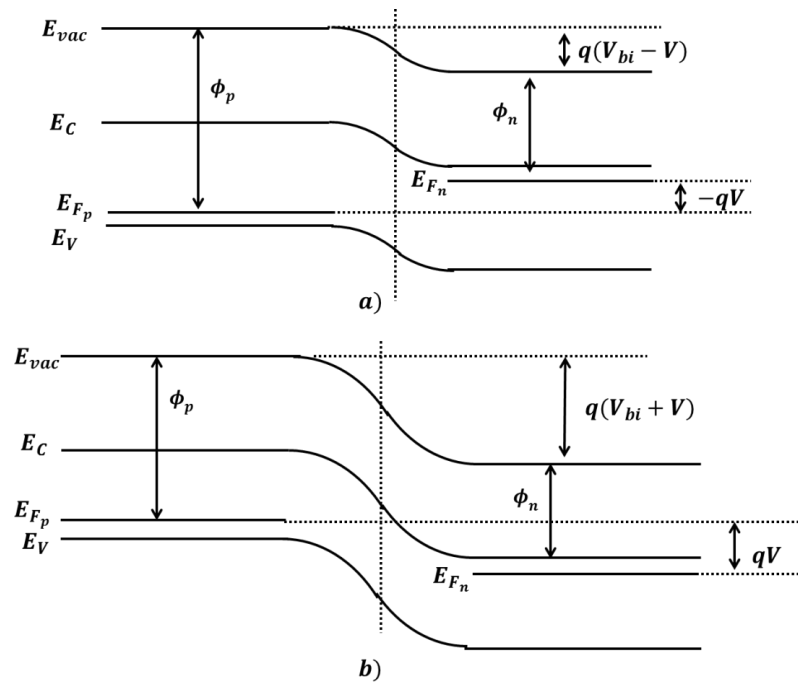


Figure 3-31. Band profile for a p-n junction under a) forward bias and b) reversed bias.

Forward bias is the application of the voltage across the p-n junction so that the electric field at the junction is reduced. If we apply a positive voltage to the p-type semiconductor side and a negative voltage to the n-type side, the direction of the external field (V) will be oppose to the build in voltage (V_{bi}) and the net electric field across the p-n junction is equal to the difference between the existing field in the depletion region and the external field $V_{bi} - V$ as shown in Figure 3-31 (a).

The effect of forward bias is the same as when the semiconductor is under illumination with the photon energies of incident light greater than the band gap E_g . The electron-hole pair generated from light absorption will be separated at the junction interface; the electrons will accumulate in the n-type material and the holes in the p-type side. The injection of a large amount of holes will decrease the hole Fermi energy E_{F_p} in the p-type material while the injection of the electrons will increase the electron quasi-Fermi energy E_{F_n} in the n-type material. The shift of the Fermi levels in the two semiconductors has caused photovoltage across the junction, pointing from p-side to n-side. The total voltage bias will be equal to $V_{bi} - V$, the same as applying an external field with voltage V .

If we define the direction of the forward bias as positive, the net voltage across the junction will be written as

$$V = E_{F_n} - E_{F_p} \quad (3.12.30)$$

Applying Equations (3.2.13) and (3.2.14) for the Fermi energy level yields

$$V = E_C - E_V + kT \ln \frac{np}{N_C N_V} \quad (3.12.31)$$

The newly established voltage decreases the energy barrier for the diffusion of the majority charge carriers, the diffusion current will increase in the forward biased p-n junction, and the drift current will stay essentially unchanged as it mainly depend on the densities of the minority charge carriers when the field is not changing too much.

3.12.7 p-n Junction under Reversed Bias

When an external field with the same direction as the built in field in the junction is applied to the device as shown in Figure 3-31(b), the two fields add up and the total bias across the junction increases. In this scenario, more minority charge carriers are extracted from the semiconductor and the depletion region expands and consequently the energy barrier increases in the junction decreasing diffusion current.

3.13 References

- ¹ D. Leadley.
- ² R. d. L. Kronig and W. G. Penney, Proceedings of The Royal Society of London. Series A, Containing Papers of A Mathematical and Physical Character (1905-1934) **130**, 499 (1931).
- ³ J. Singleton, *Band Theory and Electronic Properties of Solids* (OUP Oxford, 2001).
- ⁴ J. Callaway, Physical Review **97**, 933 (1955).

- 5 N. P. Kovalenko, Y. P. Krasny, and U. Krey, in *Physics of Amorphous Metals*
(Wiley-VCH Verlag GmbH & Co. KGaA, 2005), p. 15.
- 6 J. P. Colinge and C. A. Colinge, *Physics of Semiconductor Devices* (Springer,
2002).
- 7 H. Zimmermann, *Integrated silicon optoelectronics* (Springer-Verlag, 2000).
- 8 R. E. Hummel, *Electronic properties of materials* (Springer New York, 2011).
- 9 J. Nelson, *The Physics of Solar Cells* (ICP, Imperial College Press, 2003).
- 10 V. Zeghbroeck, *Principles of Semiconductor Devices and Heterojunctions*
(Prentice Hall PTR, 2010).
- 11 A. P. Godse and U. A. Bakshi, *Electronic Devices* (Technical Publications, 2009).
- 12 J. E. Lennard-Jones, *Transactions of the Faraday Society* **25**, 668 (1929).
- 13 M. Clugston and R. Flemming, *Advanced Chemistry* (OUP Oxford, 2000).
- 14 C. S. Foote, W. H. Brown, B. L. Iverson, and E. V. Anslyn, *Organic Chemistry*
(BROOKS COLE Publishing Company, 2011).
- 15 T. Kasuya and S. Koide, *Journal of the Physical Society of Japan* **13**, 1287 (1958).
- 16 N. F. Mott, *Journal of Non-Crystalline Solids* **1**, 1 (1968).
- 17 C. J. Brabec, *Organic Photovoltaics: Concepts and Realization* (Springer, 2003).
- 18 L. J. A. Koster, M. Kemerink, M. M. Wienk, K. Maturová, and R. A. J. Janssen,
Advanced Materials **23**, 1670 (2011).
- 19 L. J. A. Koster, V. D. Mihailetschi, and P. W. M. Blom, *Applied Physics Letters*
88 (2006).
- 20 E. V. Anslyn and D. A. Dougherty, *Modern Physical Organic Chemistry*
(University Science Books, 2006).

- 21 J. L. Bredas and G. B. Street, *Accounts of Chemical Research* **18**, 309 (1985).
- 22 V. V. M. Agranovich, G. C. L. Rocca, and S. I. d. Fisica, *Nanostrutture
Organiche: Scienza E Tecnologia* (Ios PressInc, 2002).
- 23 M. Wan, *Conducting Polymers with Micro Or Nanometer Structure* (Tsinghua
University Press, 2008).
- 24 *Advances in polymer science* (Springer-Verlag).
- 25 I. Pelant and J. Valenta, *Luminescence Spectroscopy of Semiconductors* (OUP
Oxford, 2012).
- 26 J. Frenkel, *Physical Review* **37**, 17 (1931).
- 27 E. Kaxiras, *Atomic and Electronic Structure of Solids* (Cambridge University
Press, 2003).
- 28 M. P. a. C. E. Swenberg, *Electronic Processes in Organic Crystals and Polymers,
2nd ed.* (Oxford University Press, New York, 1999).
- 29 D. N. Sathyanarayana, *Electronic Absorption Spectroscopy and Related
Techniques* (Universities Press (India) Pvt. Limited, 2001).
- 30 D. R. Bates and B. Bederson, *ADV IN ATOMIC & MOLECULAR PHYSICS*
(Elsevier Science, 1989).
- 31 p. Jablonski diagram and energy transfer rate.
- 32 J. Daintith, W. Gould, and V. Illingworth, *Astronomy* (Facts On File,
Incorporated, 2009).
- 33 F.-J. Haug, p. The solar spectrum.
- 34 C. S. Solanki, *Solar Photovoltaics : Fundamentals, Technologies and
Applications* (PHI Learning, 2011).

- 35 P. Peumans, A. Yakimov, and S. R. Forrest, *Journal of Applied Physics* **93**, 3693
(2003).
- 36 A. Luque and S. Hegedus, *Handbook of Photovoltaic Science and Engineering*
(Wiley, 2011).
- 37 C. F. Zhang, J. C. Zhang, Y. Hao, Z. H. Lin, and C. X. Zhu, *Journal of Applied*
Physics **110** (2011).
- 38 H. Norde, *Journal of Applied Physics* **50**, 5052 (1979).
- 39 R. C. Dorf, *The Electrical Engineering Handbook* (CRC Press published, 1997).
- 40 L. M. Fraas and L. D. Partain, *Solar Cells and Their Applications* (Wiley, 2010).
- 41 H. Ishii, K. Sugiyama, E. Ito, and K. Seki, *Advanced Materials* **11**, 605 (1999).

4. Interface Study between P3HT:PCBM and ITO/PEDOT:PSS for Organic Photovoltaics

4.1 Introduction

In this chapter, the aim is to investigate how the donor/acceptor interface of OPV devices affects the performance. In the second section of this chapter this effect is studied by using a bi-layer (p-n junction morphology) instead of a blended one, for the photoactive layer. In the fabrication of the p-n junction OPV device, dynamic spin coating is used as a deposition technique. After the first layer of P3HT is spin-coated onto the substrate, PCBM is then deposited using dynamic spin coating. By varying the spin-coating parameters, a device structure of ITO/PEDOT:PSS/P3HT/PCBM/Al with a range of P3HT/PCBM interface morphologies, from low level inter-digitated structure to direct flat contact, is demonstrated. The film thickness and interface morphology of the active layer are determined by AFM. Device *PCEs* are correlated to the film thickness and interface morphology of the active layer.

In the third section, electro-polymerized PEDOT:PSS (EPEDOT:PSS) is described as a replacement for the spin coated PEDOT:PSS (SPEDOT:PSS) HTL. The device performances are compared using different PEDOT:PSS fabrication methods. The degradation study for the devices using EPEDOT:PSS was carried out over a range of 0 to 10 days. Results are compared with the SPEDOT:PSS based devices reported in our

previous study. To correlate the degradation performance with the ITO/PEDOT:PSS interface, XPS measurements were carried out for both the anode junctions and the etching effect of the PEDOT:PSS on ITO was studied.

4.2 The Study of Donor/Acceptor Interface Morphology using P-N Junction Planerized OPVs

4.2.1 Background

In the last few decades great efforts in OPVs have been made¹⁻³, leading to promising successes with power conversion efficiencies (*PCEs*) reaching as high as 8%, most of which are based upon the bulk hetero-junction OPV architecture⁴⁻⁶. This complex blending structure has proved to be critical in solving one of the challenges for OPVs — the short exciton diffusion length (~ 10 nm)⁷. The abundance of significant donor/acceptor interfaces have given rise to a high exciton dissociation efficiency, one of the crucial processes (Figure 4-1) required to efficiently convert light into usable current⁸.

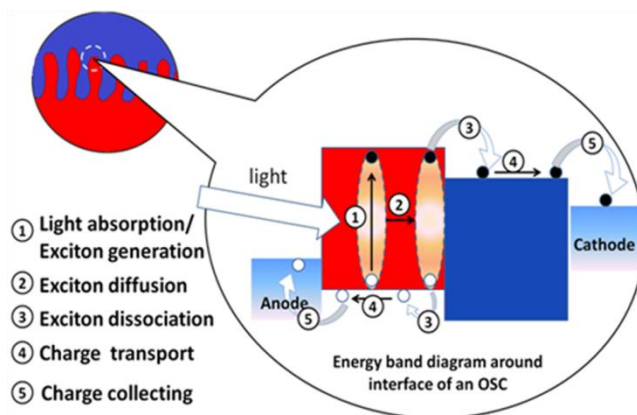


Figure 4-1. Schematic drawing of the five sequential steps converting light into photocurrent.

As research on bulk heterojunction layers has progressed to a significant degree of maturity from its beginning when Sariciftci et al. first demonstrated its effectiveness⁹, additional charge collection improvements become more elusive. Whether marginal changes in morphology through annealing techniques, new photoactive polymers, new device architecture or examining in more detail the interfacial materials¹⁰⁻¹⁴, progress is step-wise and slow. More recently, there has been an increased interest in combining the large phase separation regions in bulk heterojunctions with domains possessing high order percolating paths (Figure 4-2) which has the potential to achieve high charge transport efficiency. In effect, by looking at the interface between the p and n species in a bulk heterojunction, the question arises whether there is a more effective manner in combining both — as in a p-n junction layer structure.

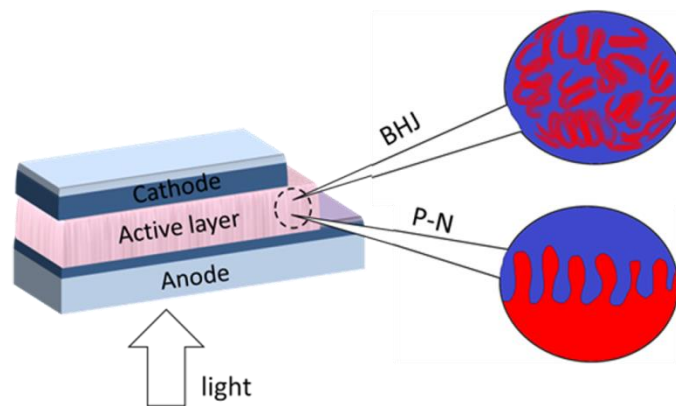


Figure 4-2. Schematic drawings of bulk heterojunction and the p-n junction architecture with a cross finger interface morphology.

Numerous efforts have been made to realize this effective structural combination. Forrest *et al.* believed that by introducing vertical phase separation to obtain a highly

interconnected and entangled interpenetrating network, the series resistance in the organic bulk heterojunction can be reduced, thus impeding carrier extraction. They applied organic vapor phase deposition (OVPD) in fabrication of the photo-generation layer of copper phthalocyanine (CuPc) and C₆₀. The two materials were arranged in a way that when the second layer (C₆₀) was deposited onto the first layer (CuPc), before reaching full coverage, another layer of CuPc would be applied onto C₆₀, so the third layer was also in contact with the first layer. By continuously repeating this process, 3D interpenetrating nanocrystalline networks of CuPc and C₆₀ could be formed. Their device yields a *PCE* of ~ 4.5%¹⁵.

Besides the structure of the interpenetrating multilayer, a bilayer interdigitated morphology as shown in the schematic representation in Figure 4-2 is frequently mentioned as an ideal structure to enhance exciton dissociation and charge extraction simultaneously by optimizing the interface in the p-n junction layer into an ordered bulk heterojunction¹⁶⁻¹⁸. The high aspect ratio of this interdigitated structure can potentially increase device performance by enhancing the delicate balance between phase separation and crystallinity. At present, nanoimprint lithography¹⁷ and glancing angle deposition¹⁹ are typically employed in achieving this structure. Using nanoimprint lithography, He *et al.* fabricated a comb wedge structured cell. A Si mode with a featured pattern size of between 25~200 nm was used to pattern the first film on a suitable substrate, then the patterned first film was used as a mold to imprint the second film, resulting in a double imprinted OPV device. Their device yields a *PCE* of ~2.3%, improving upon their bulkheterojunction control group with a *PCE* of 1.9%¹⁷;

Brett et al., grew CuPc nanocolumns on ITO maintaining diameters of 40 - 50 nm using glancing angle deposition, precise length and width control of the nanorods were explored, aiming to apply this technique as another substitution in realizing the ideal morphology¹⁹.

However, the high cost of vacuum evaporation as well as that of glancing angle deposition limits their application when attempting to scale up to industrial production. Also, the delicate imprinting scale in nanoimprint technique results in a series of crucial problems which are still waiting to be solved. In this case, solution processing will still be the more preferred way to industrial production for its cheap and easy processing. The major issue to be addressed in this method is the difficulty in depositing two uniform polymer layers sequentially for the p-n junction photoactive device.

4.2.2 UV-Visible Absorption Spectroscopy

To understand how the dynamic spin coating deposition method affects the thickness of the photoactive layers, the UV-Visible spectra of films fabricated under the same concentration both for P3HT and PCBM layers (PCBM 5 g/L, P3HT 10 g/L) were investigated. As shown in Figure 4-3, the absorption peak centered at 330 nm indicates the successful deposition of PCBM on the P3HT film²⁰ using this method. According to the Beer-Lambert law which gives a relation between the absorbance and the film thickness, the deep peak density fall of chlorobenzene (b.p. 132 °C) treated film at 330 nm shows that the PCBM layer formed with this high boiling point solvent is notably

thinner than the ones with lower boiling points (di-chlorobenzene (CH_2Cl_2) b.p. $40\text{ }^\circ\text{C}$; chloroform (CHCl_3) b.p. $61\text{ }^\circ\text{C}$). This may be attributed to the higher surface tension of chlorobenzene, which hinders the PCBM solution from building up on top of the P3HT film during dynamic spin coating²¹. During the solvent evaporation of a thin, spin-cast film, the P3HT 1-Dimensional (1-D) polymer chains will self-organize in a lamellar structures, this is called intrachain or π - π^* stacking. The π - π^* stacking will introduce a difference in the UV-visible spectrum between the P3HT solution and dry film: a bathochromic shift in the absorption spectrum towards 515 nm (2.41 eV) can be observed. The three featured vibronic absorption peak due to the P3HT π - π^* transitions are at 515 nm, 550 nm and 600 nm (2.25 and 2.07 eV)²². The peak intensity difference at 515 nm shows that the CH_2Cl_2 solution rarely affected the thickness of P3HT film (absorbance: A-P3HT/ CH_2Cl_2 0.97, pristine P3HT normalized to 1), while CHCl_3 solution washed away about 30% of P3HT film (B-P3HT/ CHCl_3 0.74) and chlorobenzene solution around 50% (C-P3HT/chlorobenzene 0.49).

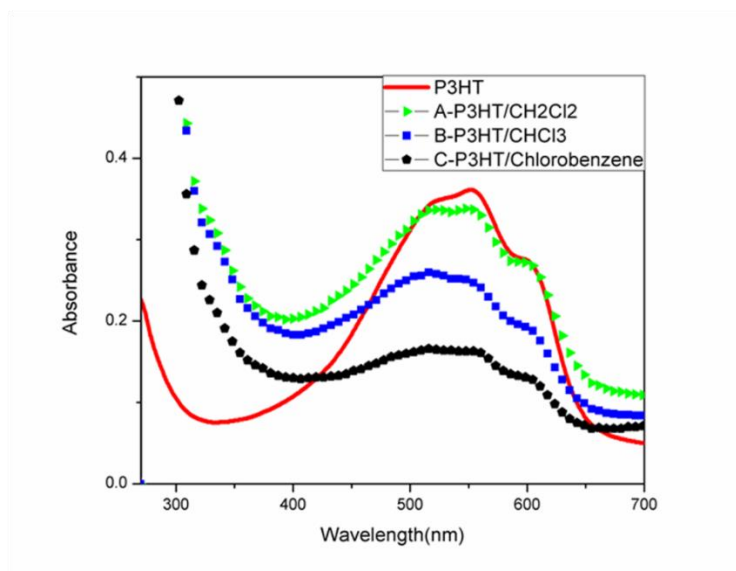


Figure 4-3. Absorption spectra of P3HT film (red line); P3HT film (10 g/L) spin coated with PCBM (5 g/L) in CH₂Cl₂ (green), CHCl₃ (blue) and chlorobenzene (black).

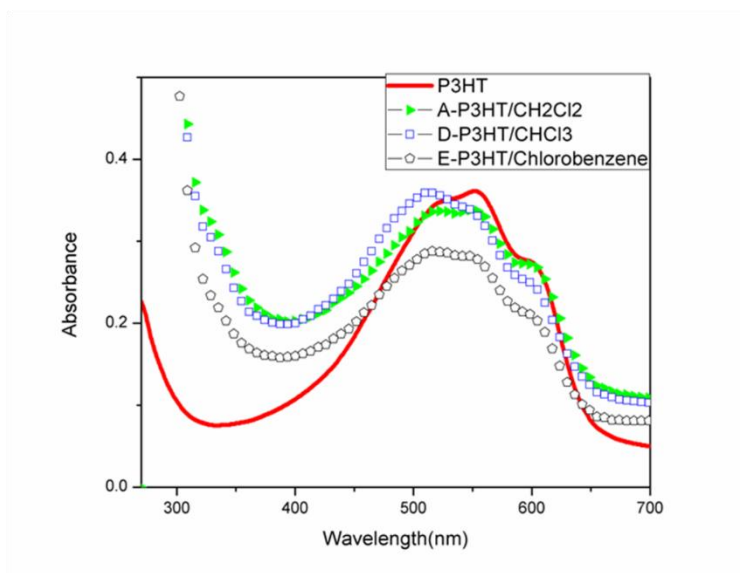


Figure 4-4. Absorption spectra of P3HT (10 g/L) film (red line); P3HT (10 g/L) spin coated with PCBM (5 g/L) in CH₂Cl₂ (green); P3HT (15g/L) with PCBM (5 g/L) in CHCl₃ (blue); P3HT (20 g/L) with PCBM (5 g/L) in chlorobenzene (black).

In order to correlate the cell performance with interface morphology generated by different solvents, we need to exclude the absorbance differences attributed to the P3HT layer. In this case another group with adjusted P3HT concentrations was fabricated and detailed parameters are listed in Table 4-1. Concentrations of P3HT are increased according to the UV-visible spectra. After the adjustment, a group of films with similar absorbance were obtained as shown in Figure 4-4.

	Sample	P3HT conc. (g/L)	Solvent for PCBM	Absorbance	Absorbance after normalizing
Group 1	A- CH ₂ Cl ₂	10	CH ₂ Cl ₂	0.34	0.97
	B- CHCl ₃	10	CHCl ₃	0.26	0.74
	C- chlorobenzene	10	Chlorobenzene	0.17	0.49
Group 2	A- CH ₂ Cl ₂	10	CH ₂ Cl ₂	0.34	0.97
	D- CHCl ₃	15	CHCl ₃	0.36	1.03
	E- chlorobenzene	20	Chlorobenzene	0.29	0.83
	Pristine P3HT	10	Chlorobenzene	0.35	1

Table 4-1. Absorbance at 515 nm of P3HT/PCBM films under different processing conditions.

4.2.3 Atomic Force Microscopy

To develop an understanding of the P3HT/PCBM interface formation by means of the dynamic spin coating method, a simulated P3HT/PCBM interface was constructed by

depositing the corresponding solvents for PCBM solutions on top of the P3HT layer. It is considered a valid simulation of the P3HT/PCBM interface because the interface may only be modified by the solvent and additionally, the concentration of PCBM is very low (5 g/L). AFM was used to probe the surface morphology of the resulting films. Figure 4-5 shows the phase and section analysis images obtained. The boiling point of the solvent used to dissolve PCBM is a critical parameter to form a rough interface by dynamic spin coating. When it is low enough, the solvent evaporates quickly during the dynamic spin coating process, making the P3HT form a roughened surface as it is partially being corroded away. As shown in the AFM image in Figure 4-5a, after spin coating the CH_2Cl_2 on the P3HT film, which is the lowest b.p. solvent used (40°C), the P3HT surface has the roughest morphology. The peak to valley height variation of $\sim 5\text{-}17\text{ nm}$ is of the order of the exciton diffusion length in a P3HT film. As the boiling point of the solvent used increases, the film morphology becomes slightly smoother (CHCl_3 , Figure 4-5b) and then completely smooth (chlorobenzene, Figure 4-5c). Therefore, the roughness of the P3HT/PCBM interface can be modified through the application of different solvents based on their boiling points. It is also possible to achieve a pseudo-interdigitated interface in our p-n junction cell using PCBM in CH_2Cl_2 .

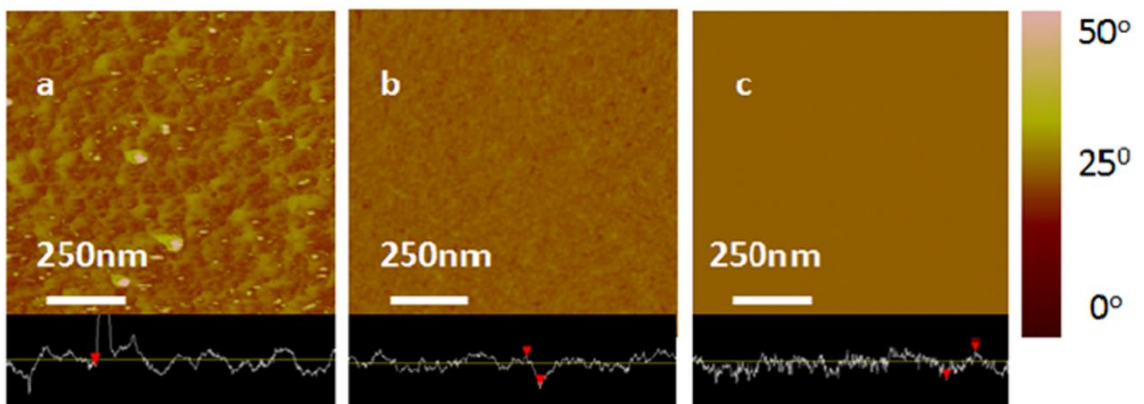


Figure 4-5. AFM phase images of P3HT films after dynamic spin coating with a) CH₂Cl₂; b) CHCl₃; c) chlorobenzene to simulate the P3HT/PCBM interface morphology. The inserts are section analysis images for the corresponding films ($z = -10\sim 10$ nm).

The thickness of the PCBM layer on top of P3HT in the p-n junction was determined by deducting the thickness of P3HT films which were dynamically spin coated with the corresponding solvents from the total thickness of the P3HT/PCBM films (Table 4-2). The uneven nature of the film did not allow the determination of exact values, however, a range was easily obtained. In general the PCBM layer processed from CH₂Cl₂ and CHCl₃ are much thicker (more than 10 nm) than the one obtained from chlorobenzene (~ 3 nm). This observation is consistent with the UV-visible data.

Group 1	Solvent boiling point (°C)	P3HT/PCBM thickness (nm)	P3HT thickness (nm)	PCBM thickness (nm)
A- CH ₂ Cl ₂	40	112.18±6.07	101.81±9.77	10.37±3.7
B- CHCl ₃	61	103.43±3.00	85.84±8.44	17.59±5.45
C- Chlorobenzene	132	79.10±3.56	75.76±6.87	3.5±3.32

Table 4-2. Thickness of the P3HT (PCBM) films under different processing conditions determined by AFM.

4.2.4 Device Performance

Figure 4-6 shows the current density-voltage (J-V) characteristics for the P3HT/PCBM p-n junction solar cells of both groups. All device parameters are summarized in Table 4-3. From the data a decreasing trend of the *PCEs* (A 1.78% > B 1.27% > C 0.15%) and *FF* (A 0.43 > B 0.39 > C 0.32) for Group 1 is observed, it is clear that the lowest boiling point solvent CH₂Cl₂ is the most promising choice for making solution processed p-n junction OPV devices. The large efficiency drop for the chlorobenzene processed device is related to the extremely thin PCBM layer deposited (~3 nm), in which case a consistent interface is difficult to achieve, which in turn reduces both the V_{OC} and short J_{SC} ²³.

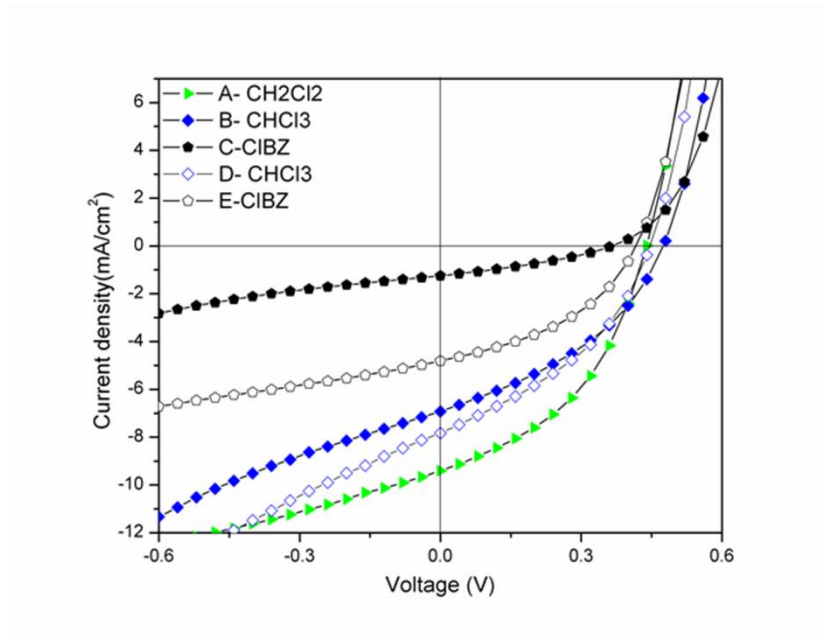


Figure 4-6. J-V characteristics of the P3HT:PCBM p-n junction cells fabricated under dynamic spin coating method for Group 1 (Solid markers) and Group 2 (Hollow markers).

		Best PCE (%)	Average PCE (n=8)	Voc (V)	Jsc (mA/cm ²)	FF
Group 1	A- CH ₂ Cl ₂	1.78	1.50±0.25	0.44	9.40	0.43
	B- CHCl ₃	1.27	0.84±0.32	0.47	6.89	0.39
	C- chlorobenzene	0.15	0.11±0.03	0.37	1.27	0.32
Group 2	A- CH ₂ Cl ₂	1.78	1.50±0.25	0.44	9.40	0.43
	D- CHCl ₃	1.34	0.93±0.27	0.45	7.86	0.38
	E- chlorobenzene	0.83	0.49±0.17	0.42	4.80	0.41

Table 4-3. Summary of device performances of P3HT/PCBM p-n junction photovoltaic devices.

In Group 2, with adjusted P3HT concentration, the P3HT absorbances in CHCl_3 and chlorobenzene processed cell are 1.03 and 0.83 (CH_2Cl_2 processed film 0.97), respectively. Besides the decreasing trend in power efficiency (A 1.78% > D 1.34% > E 0.83%), a decreasing trend is also observed in current density, which is directly correlated with exciton dissociation efficiencies resulting from the difference in interface morphology¹⁸. Given the trend is consistent with the roughness difference in phase images, it is clear that slight change in interface can improve the device performance considerably. The interdigitated morphology obtained through dynamic spin coating successfully resulted in the best device with a *PCE* 1.78 %, V_{OC} 0.44 V, J_{SC} 9.4 mA/cm² and *FF* of 43%, respectively. Table 4-3 summarizes all the characteristics of P3HT/PCBM p-n junction photovoltaic devices.

4.3 Electro-polymerized PEDOT:PSS as Hole Transport Layer

4.3.1 PEDOT:PSS as Hole Transport Layer

It has been observed in the ITO based OPV device that the use of PEDOT:PSS as the HTL can increase the V_{OC} by up to 0.5 V²⁴. In the works by Greczynski *et al.*²⁵ and Kugler *et al.*,²⁶ XPS was used to measure the energy level of all the materials at the contacting interface. Detailed band bending mechanisms were studied and it was discovered that the band bending in PEDOT:PSS is due to rich charge density states that help in matching the work function of ITO (~4.7 eV) with the highest occupied molecular orbital (HOMO) of the donor material in the photoactive layer (~5.1 eV for P3HT). In the presence of PEDOT:PSS the hole transfer barrier between the donor material and the

ITO anode can be reduced to a large extent. Also, the PEDOT:PSS layer can act as a buffer layer between the photo-generation layer and the inorganic electrode, reducing the occurrence of pinhole defects and increase the shunt resistance in the OPV device.

Conversely, the PSS additive that is used to balance with the oxidized state in PEDOT improving solubility, can harm device stability due to its acidic and insulating nature. Using Rutherford backscattering, Jong et al.²⁷; found 0.02% atomic concentration of indium in PEDOT:PSS film immediately after the fabrication. The percentage increased to 1.2 % after 10 days exposure to air at 8 °C. The degradation of the ITO/PEDOT:PSS interface is due to the strong acidic nature of PSS. Therefore in order to reduce the etching in ITO and extend the lifetime of the device, the HTL has to be replaced or the percentage of PSS present must be reduced.

4.3.2 J-V Characteristics of OPV devices with Buffer Layer of SPEDOT:PSS and EPEDOT:PSS

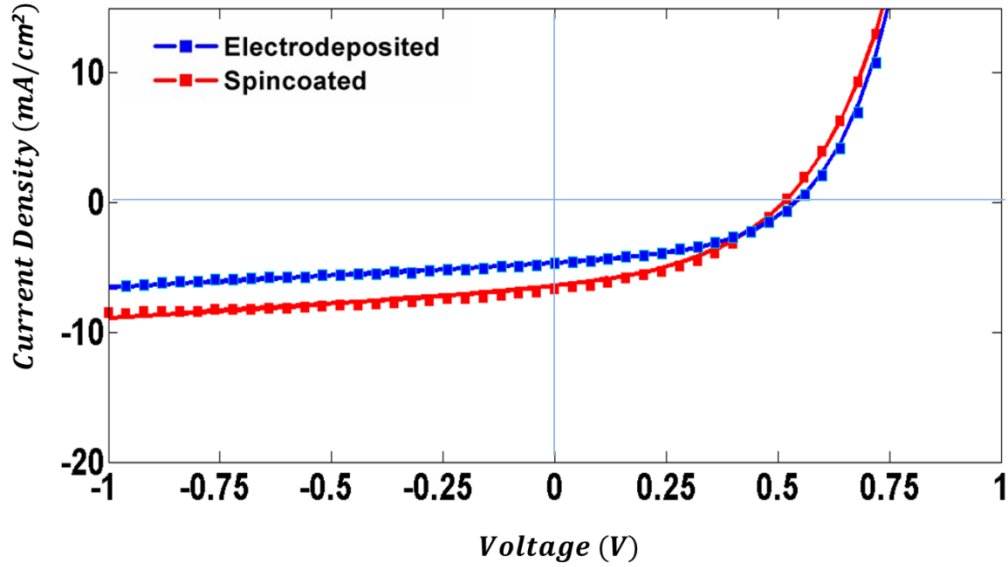


Figure 4-7. J-V curves for OPV devices with electro-polymerized (blue) and spin coated (red) PEDOT:PSS as buffer layer. The data has been simulated (lines) using a model developed by Zhang *et al*²⁹.

In Figure 4-7, the J-V curves for two ITO/PEDOT:PSS/P3HT:PCBM/Al conventional OPV devices are given for a HTL made of either SPEDOT:PSS or EPEDOT:PSS. It can be seen that the performance of the best devices from the two groups are comparable. In the case of spin coated standard device, the *PCE* is 1.43 %, the J_{SC} is 6.71 mA/cm², the V_{OC} is 0.513 V and the *FF* is 41.5 %. For electro-polymerized, these values are 1.11 %, 4.71 mA/cm², 0.539 V and 43.7%, respectively. The V_{OC} of the electro-polymerized OPV is slightly larger than the spin coated one while the J_{SC} is lower. After applying the fitting to the experimental data using the model developed by Zhang *et al*²⁹, the series and shunt

resistance are extracted for both devices. For the standard device with SPEDOT:PSS as buffer layer, the values are 0.0597Ω and 453.4Ω , respectively. While for the EPEDOT:PSS device, the values are similar, 0.3711Ω for series and 545.8Ω for shunt resistance. The lower series resistance in the OPV device with the SPEDOT:PSS indicates a better ITO/SPEDOT:PSS or SPEDOT:PSS/P3HT:PCBM contact or a lower bulk resistance in the bulk SPEDOT:PSS than the electro-polymerized device.

4.3.3 Stability Study of ITO Electrodes with EPEDOT:PSS as HTL

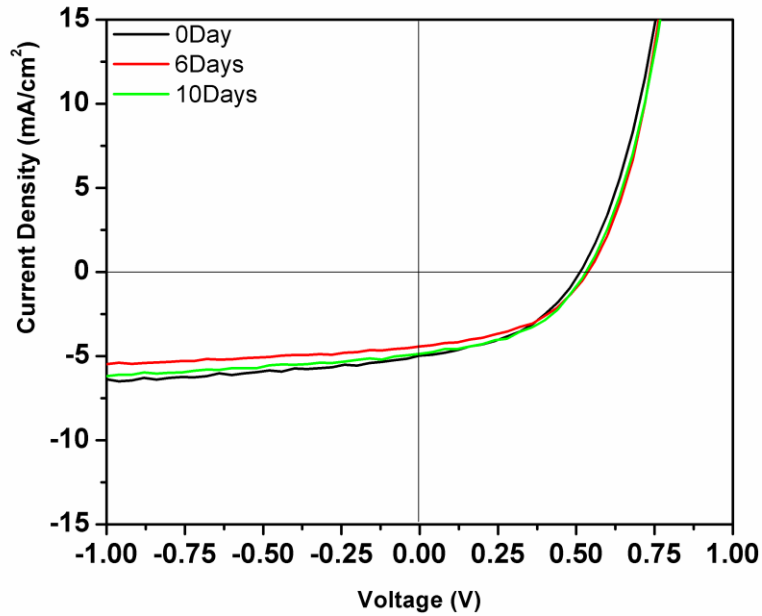


Figure 4-8. J-V curves of OPV devices based on electro-polymerized PEDOT:PSS with different exposure time.

To study the stability of ITO electrode deposited with EPEDOT:PSS, devices of the structure ITO/EPEDOT:PSS/P3HT:PCBM/Al were fabricated. The detailed fabrication

process of the electro-polymerization is described in Chapter 2. The degradation study was carried out by exposing the ITO/EPEDOT:PSS substrates to a sub-ambient condition with a humidity ~90% for a set of time (0 days, 6 days and 10 days). Then the substrates with different exposure time were fabricated into devices and tested at the same time.

Figure 4-8 shows the J-V curves of the highest efficiency ITO/EPEDOT:PSS devices from each of the three degradation. It is a surprise that the curves don't show any deflection over exposure time. The V_{OC} , J_{SC} and the FF which can be seen from the shape of the curves remain unchanged throughout the 10 day degradation study. To have a better comparison, the four principle values obtained from each of the three degradation groups were extracted and averaged over 8 devices from each group, the obtained values and the standard deviations are presented in Figure 4-9. In agreement with the performance of the best devices, the average values also show stable performance of the OPV devices with EPEDOT:PSS. $V_{OC} \sim 0.52V$, the J_{SC} are $\sim 4.5mA/cm^2$, the FF s are $\sim 45\%$ and the PCE s $\sim 1.1\%$.

The degradation study here shows a big improvement in the stability of the OPV device with EPEDOT:PSS than the spin coated device compared with the results obtained in our previous work²⁸. In our past stability study of the OPV devices with SPEDOT:PSS, enormous degradation was observed within 10 days exposure time. The device PCE drops from $\sim 1\%$ to $\sim 0.1\%$, FF from $\sim 40\%$ to $\sim 20\%$ and J_{SC} from ~ 9 to $2 mA/cm^2$.

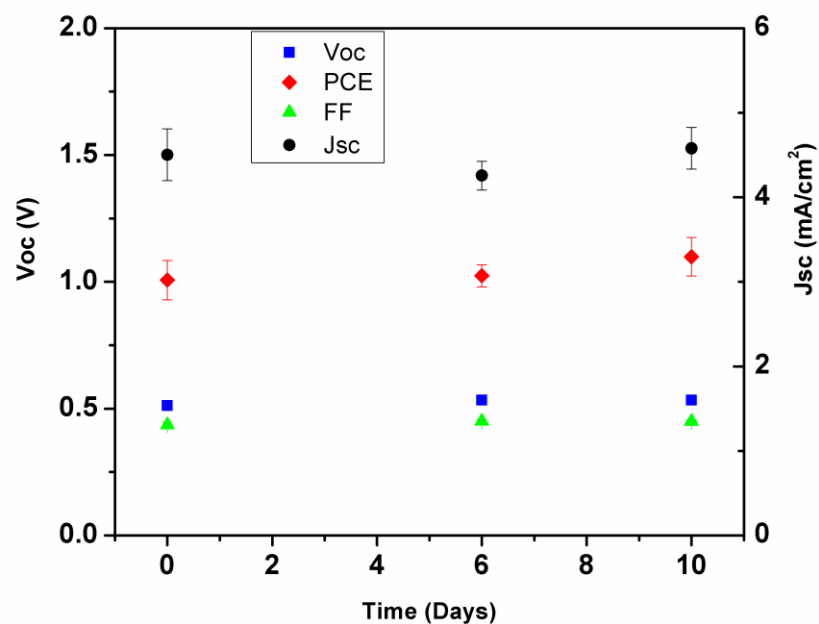


Figure 4-9. *PCE*, *J_{sc}*, *FF* and *V_{oc}* of OPVs using electro-polymerized PEDOT:PSS as HTL with different exposure time for ITO/PEDOT:PSS to ambient condition with humidity ~90%.

4.3.4 XPS study of the Spin Coated and Electro-Polymerized PEDOT:PSS on ITO

In order to have a deeper understanding of how the EPEDOT:PSS improves the OPV stability, a comparative analysis of both SPEDOT and EPEDOT layers on ITO were carried out using XPS. The measurements were taken for durations ranging from 0 to 15 days. Between each measurement the samples were kept in an ambient condition.

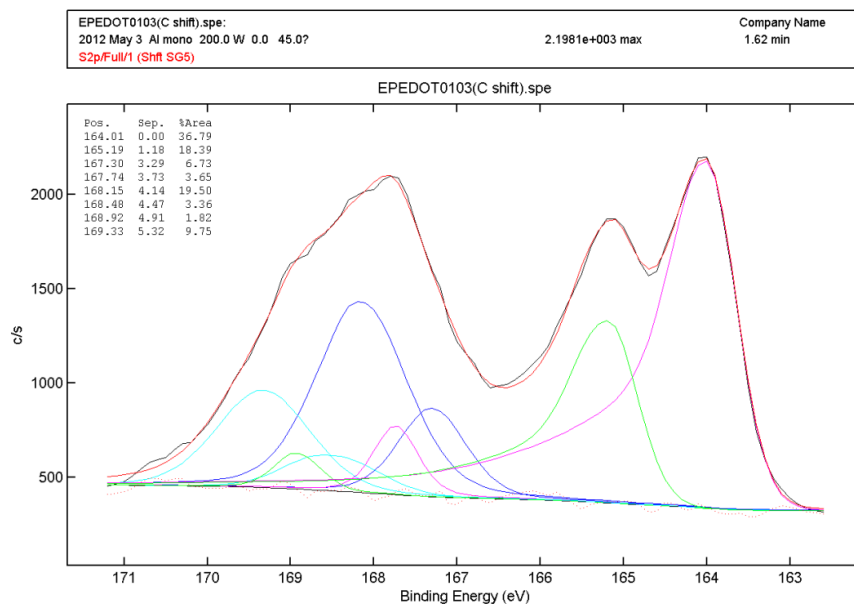


Figure 4-10. The S(2p) signal from electro-polymerized PEDOT:PSS on ITO for 0 Day.

Figure 4-10 shows the deconvoluted S_{2p} XPS signal from the EPEDOT:PSS on ITO on the 0 day after fabrication. The three S doublet states at 167.30 eV, 167.74 eV and 168.15 eV are contributed by the S state in PSS⁻(PEDOT⁺), PSS⁻(Na⁺) and PSS⁻(H⁺), respectively³⁰; whilst the S doublet at 164.01 eV is contributed by the S state in PEDOT^{25,30}. By determining the area under each peak, information regarding the atomic concentration of each constituent can be extrapolated.

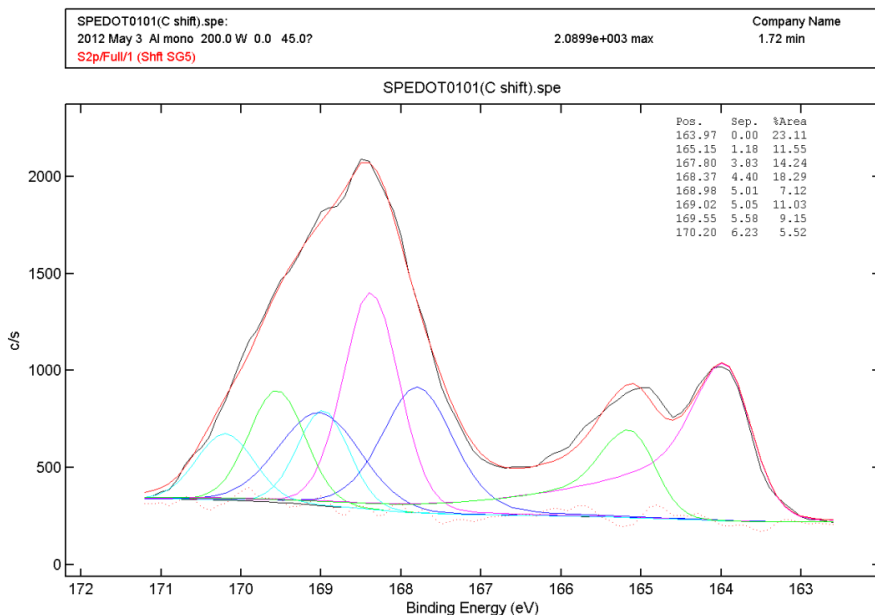


Figure 4-11. The S(2p) signal from spin coated PEDOT:PSS on ITO for 0 Day.

In the S2p XPS signal for the SPEDOT:PSS, there are also four sulfur states as shown in Figure 4-11. It is clearly shown in the graphs that for the EPEDOT:PSS, the sulfur signal intensity from PEDOT (the right peak) is much higher than the one in SPEDOT:PSS film. The detailed portion of each constituent was extracted from each spectrum and summed up in Table 4-4. It is clearly shown from the PEDOT to PSS ratio that by using electro-polymerization, the portion of PSS in PEDOT:PSS can be modified to a lower value than SPEDOT:PSS. As proposed in Tsai et al.³¹ and Yambem et al.²⁸'s works, on the etching mechanism of PEDOT:PSS on ITO, the excess PSS⁻ legands can replace the oxygen atom in In-O and Sn-O bonds after the bonds are protonated by the protons presented in PSS⁻H⁺. Then due to the chelation effect of In-PSS and Sn-PSS the weakened inner In-O and Sn-O bonds will cause the detachment of the ITO layer in the

form of $\text{In}(\text{RSO}_3)_3$ and $\text{Sn}(\text{RSO}_3)_4$ into PEDOT:PSS layer, and further etching can be continued with the presence of water and protons. In this case, it is clear that the high indium concentration in the SPEDOT:PSS (1.86 %) here can be a direct result of the high PSS^- ratio; While in the EPEDOT:PSS, lower PSS^- ratio significantly reduces the indium concentration (0.17 %), which is ~11 times lower than the one in SPEDOT.

	In (%)	S in PEDOT ⁺ (%)	S in PSS ⁻ (%)	In/S (%)	PEDOT/PSS
SPEDOT:PSS	1.86	3.3072	6.2928	0.19375	0.525553
EPEDOT:PSS	0.17	5.4463	4.4228	0.017224	1.231414

Table 4-4. Atomic concentration for different constituents in SPEDOT:PSS and EPEDOT:PSS films on the 0 day after fabrication.

Figure 4-12 shows the indium atomic concentration in PEDOT:PSS over exposure time from 0 day to 15 days in both types of ITO/PEDOT:PSS substrates. It is found that for SPEDOT:PSS on ITO, the indium concentration keeps increasing from 1.86 to 3.08 % while for the EPEDOT:PSS on ITO, the indium concentration increases at a very low rate and remains stable at ~0.4 % after 7 days. The different trends observed in the XPS analysis can be correlated to the device performances of the degradation study. The decreased PSS^- concentration in the EPEDOT:PSS has greatly improved the stability of the OPV devices.

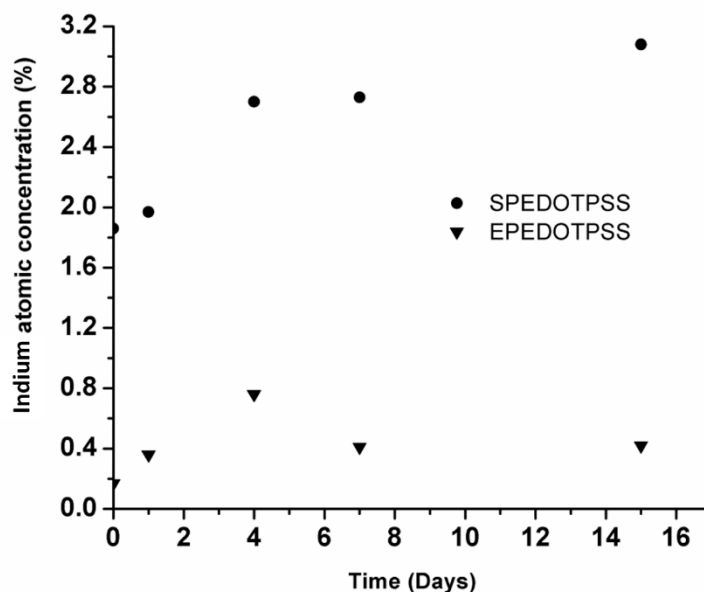


Figure 4-12. Indium atomic concentration within PEDOT:PSS layer over exposure time from 0 to 15 days for both SPEDOT:PSS and EPEDOT:PSS substrates.

4.4 Conclusion

In section 2 the interface between P3HT:PCBM in photoactive layer was studied. p-n junction OPVs with different P3HT:PCBM interface morphology were achieved by selecting the right solvent using dynamic spin coating method. Although the p-n OPV efficiency obtained was not as good as the bulk heterojunction devices, a clear trend of increasing efficiency was observed by modifying the interface morphology from flat to pseudo-interdigitated contact. By AFM measurements of the surface morphology it is clear that the device with higher surface roughness shows higher J_{SC} as well as PCE due to more excitons generated at the donor/acceptor interface. We believe by further

optimizing the interface morphology under p-n junction structure, devices with even better performance can be achieved.

In section 3 the interface between ITO/PEDOT:PSS in anode junction was well studied. In order to reduce the etching effect on ITO caused by PSS⁻ ligands, EPEDOT:PSS was used to replace the spin coated HTL. The XPS study on both ITO/SPEDOT and ITO/EPEDOT showed a reduction of the PSS/PEDOT ratio as well as the indium ratio in the film fabricated by electro-deposition. Over a 0-15 days exposure to air, the indium amount kept increasing in the SPEDOT:PSS film from 1.86 % to 3.08 %, while it remained almost the same at ~0.41 % in the electro-polymerized film after 7 days. The degradation study of the device on a 0 – 10 days base showed a consistent performance with the XPS study, the stability of the OPV device using EPEDOT:PSS can be significantly improved compared to the device using SPEDOT:PSS with ITO.

4.5 Reference

- ¹ S. Curran, S. Roth, A. P. Davey, A. Drury, and W. Blau, *Synthetic Met.* **83**, 239 (1996).
- ² A. Hagfeldt and M. Grätzel, *Accounts Chem. Res.* **33**, 269 (2000).
- ³ Y. Kim, S. Cook, S. M. Tuladhar, S. A. Choulis, J. Nelson, J. R. Durrant, D. D. C. Bradley, M. Giles, I. McCulloch, C.-S. Ha, and M. Ree, *Nat. Mater.* **5**, 197 (2006).
- ⁴ H.-Y. Chen, J. Hou, S. Zhang, Y. Liang, G. Yang, Y. Yang, L. Yu, Y. Wu, and G. Li, *Nat. Photon.* **3**, 649 (2009).
- ⁵ Y. Liang, Z. Xu, J. Xia, S.-T. Tsai, Y. Wu, G. Li, C. Ray, and L. Yu, *Adv. Mater.* **22**, E135 (2010).
- ⁶ J. Y. Kim, K. Lee, N. E. Coates, D. Moses, T.-Q. Nguyen, M. Dante, and A. J. Heeger, *Science* **317**, 222 (2007).
- ⁷ D. E. Markov, E. Amsterdam, P. W. M. Blom, A. B. Sieval, and J. C. Hummelen, *J. Phys. Chem. A* **109**, 5266 (2005).
- ⁸ P. Heremans, D. Cheyons, and B. P. Rand, *Accounts Chem. Res.* **42**, 1740 (2009).
- ⁹ N. S. Sariciftci, L. Smilowitz, A. J. Heeger, and F. Wudl, *Science* **258**, 1474 (1992).
- ¹⁰ J. Peet, M. L. Senatore, A. J. Heeger, and G. C. Bazan, *Adv. Mater.* **21**, 1521 (2009).
- ¹¹ F. G. Brunetti, X. Gong, M. Tong, A. J. Heeger, and F. Wudl, *Angew. Chem. Int. Edit.* **49**, 532 (2010).

- 12 R. Steim, F. R. Kogler, and C. J. Brabec, *J. Mater. Chem.* **20**, 2499 (2010).
- 13 W. T. Wondmagegn and S. A. Curran, *Thin Solid Films* **515**, 2393 (2006).
- 14 S. Curran, J. Talla, S. Dias, and J. Dewald, *J. Appl. Phys.* **104**, 064305 (2008).
- 15 F. Yang, K. Sun, and S. R. Forrest, *Adv. Mater.* **19**, 4166 (2007).
- 16 G. Wei, R. R. Lunt, K. Sun, S. Wang, M. E. Thompson, and S. R. Forrest, *Nano Lett.* **10**, 3555 (2010).
- 17 X. He, F. Gao, G. Tu, D. G. Hasko, S. Hüttner, N. C. Greenham, U. Steiner, R. H. Friend, and W. T. S. Huck, *Adv. Funct. Mater.* **21**, 139 (2011).
- 18 B. P. Rand, J. Genoe, P. Heremans, and J. Poortmans, *Prog. Photovoltaics* **15**, 659 (2007).
- 19 J. G. Van Dijken, M. D. Fleischauer, and M. J. Brett, *J. Mater. Chem.* **21**, 1013 (2011).
- 20 Y.-J. Cheng, S.-H. Yang, and C.-S. Hsu, *Chem. Rev.* **109**, 5868 (2009).
- 21 K. S. Lee, N. Ivanova, V. M. Starov, N. Hilal, and V. Dutschk, *Adv. Colloid Interfac.* **144**, 54 (2008).
- 22 T.-A. Chen, X. Wu, and R. D. Rieke, *J. Am. Chem. Soc.* **117**, 233 (1995).
- 23 K.-S. Liao, S. Dias, N. J. Alley, S. D. Yambem, A. Haldar, and S. A. Curran, *Thin Solid Films* **519**, 3264 (2011).
- 24 T. M. Brown, J. S. Kim, R. H. Friend, F. Cacialli, R. Daik, and W. J. Feast, *Applied Physics Letters* **75**, 1679 (1999).
- 25 G. Greczynski, T. Kugler, M. Keil, W. Osikowicz, M. Fahlman, and W. R. Salaneck, *Journal of Electron Spectroscopy and Related Phenomena* **121**, 1 (2001).

- ²⁶ T. Kugler, W. R. Salaneck, H. Rost, and A. B. Holmes, *Chemical Physics Letters* **310**, 391 (1999).
- ²⁷ M. P. De Jong, L. J. Van Ijzendoorn, and M. J. A. de Voigt, *Applied Physics Letters* **77**, 2255 (2000).
- ²⁸ S. D. Yambem, K.-S. Liao, N. J. Alley, and S. A. Curran, *Journal of Materials Chemistry* **22**, 6894 (2012).
- ²⁹ C. F. Zhang, J. C. Zhang, Y. Hao, Z. H. Lin, and C. X. Zhu, *Journal of Applied Physics* **110** (2011).
- ³⁰ G. Zotti, S. Zecchin, G. Schiavon, F. Louwet, L. Groenendaal, X. Crispin, W. Osikowicz, W. Salaneck, and M. Fahlman, *Macromolecules* **36**, 3337 (2003).
- ³¹ T.-H. Tsai and Y.-F. Wu, *Microelectronic Engineering* **83**, 536 (2006).

5. Investigation of Recombination Dynamics for ITO-free and ITO-based OPVs by Illumination Dependence Study

5.1 Introduction

This chapter deals with the development of ITO-free flexible OPV devices with highly conductive PEDOT:PSS anodes. In the beginning of section 2, the correlation of recombination with the performance of J_{SC} and V_{OC} is detailed. Later in that section, study of the different recombination mechanisms within these two types of devices is carried out by comparing the illumination responses of J_{SC} and V_{OC} . Then, the result is used to explain the varying trend of FF and PCE with respect to the light intensity. The outcome suggests the bimolecular recombination mechanism dominates the ITO-free devices. Section 3 introduces reports concerning the energy level alignment at the contacts between some commonly used materials in an OPV device, correlating the value of V_{OC} with the causes for V_{OC} boost after substituting the ITO with highly conductive PEDOT:PSS.

5.1.1 Background

While acting as a leading role in solar energy field, high efficiency silicon-based photovoltaics (PV) have some significant shortcomings. When performing under indirect

light or diffuse light, solar performance is significantly depleted due to insufficient charge carriers generated for optimum performance. This also attributes to the reason of silicon PV not being well applied in a somewhat flexible manner¹. While for OPVs, the mechanical flexibility of conjugated polymers enables their deployment to be achieved on many different surfaces, regular or irregular. The optically isotropic nature of the photoactive layer promises a power generation much less dependent on the light incidence. Yet the organic nature of the materials promises a low manufacturing cost and much lighter weight property. Contributing to all these merits of conjugated polymer, OPVs makes a superior alternative to traditional silicon PVs under various occasions, from when a highly flexible geometry is required to when the direct sunlight is unavailable.

5.1.2 Issues Associated with using ITO-based Flexible OPV

The need to develop highly flexible OPV devices to compensate for the disadvantages of traditional silicon PV has resulted in numerous works in this field. There have been attempts to use ITO electrode in fabricating flexible OPV devices. For example, Krebs et al. used a slot die coating method to deposit every device layer on ITO coated plastic substrates². They demonstrated their OPVs as functional in the form of a “solar hat” to power small electronic devices such as FM radios. However, even fabricated by all solution processing, the brittleness of thin ITO films can still result in the formation and propagation of cracks during bending or twisting, which restricts the OPVs from being truly flexible. Known from our previous work, a 3-mm curvature bending of the polyethylene terephthalate (PET) based ITO slide will result in a 10-20 times increase in

sheet resistance, from $\sim 10 \text{ } \Omega/\square$ to $\sim 200 \text{ } \Omega/\square$ [ENREF 3](#). Besides, degradation study of PEDOT:PSS on ITO from last chapter has shown that the protonation of the surface ITO due to the excess amount of protons provided by $\text{PSS}\cdot\text{H}^+$ has caused the damage of ITO surface. Therefore, in order to achieve highly flexible devices with good durability, conductive metal oxides, such as ITO, need to be replaced.

5.1.3 The Process in Developing ITO-free Flexible OPV Devices

Flexible OPV devices, with ITO electrode substituted by other conductive materials, have also been developed. Conductive metal such as Ag or Au, when vacuum evaporated to substrates to form semi-transparent ultrathin films, can be used to replace ITO as flexible anode, as in details of our previous work^{3,4}. Moreover, organic based electrode materials with both excellent electrical and optical properties are being widely studied, among which modified PEDOT:PSS with high conductivity has attracted considerable interests⁵⁻⁷, which leads to the development of ITO-free flexible electrodes. Cho et al. have demonstrated a flexible anode with a sheet resistance of $359 \text{ } \Omega/\square$ and a transparency of 89 % by gravure printing of DMSO doped PEDOT:PSS on PET substrates⁸. Their device showed a *PCE* of 2%, compared to the reference cell fabricated on ITO/glass as 3.5%. Although most of the PEDOT:PSS studies have successfully demonstrated the possibility of substituting the ITO with modified PEDOT:PSS, their power generation efficiencies are still less than 2.2%⁹ and no further studies have been carried out to investigate how the anode replacement affects the mechanisms inside the device.

5.2 Recombination Mechanisms in ITO-based Standard and ITO-free Flexible device

5.2.1 Generation and Recombination Mechanisms in OPV

By absorbing incoming light with the photon energy larger than the band gap, the electron is excited from the valence band to the conduction band, generating an exciton. The singlet excitons are represented by strongly bound electron-hole pairs. The binding energy of this electron-hole is usually within the range of 0.4~0.7 eV or even higher¹⁰, much larger than the thermal energy under operating conditions. Thus a favorable energy bias is offered as the band offset between the donor and acceptor material in the photo-generation layer to separate the bounded electron-hole pairs.

Free charges can be generated in two ways¹¹ as shown in Figure 13. In the first method, charge separation from the charge transfer (CT) excitons, which are also known as bound polarons, occurs. The CT excitons are transferred from the singlet excitons and they are still Coulomb bounded¹²; The charge transfer of singlet excitons to the CT excitons must happen at an energetically favorable site such as grain boundaries, donor-acceptor interfaces or dopant sites. After the diffusion of the singlet exciton through Förster resonance energy transfer¹³ to these sites, the charge transfer process will happen very efficiently with a time scale of femtoseconds. In the second method, free charges can be generated directly from the charge separation of the singlet excitons¹⁴. The singlet excitons usually only have short lifetime of typically less than 1 ns, within which time

they have to travel to a donor/acceptor interface for charge separation. Otherwise they will recombine or transfer to triplet excitons.

The singlet excitons and CT excitons can recombine to the ground states with the recombination rate as $R_{rec,S}$ and k_f , respectively (Figure 13). Also the singlet excitons and CT excitons can all transfer to the triplet excitons by intersystem crossing, and eventually to the ground states. The separated charges (also called free polarons) can only recombine back to the bounded polaron states, and then recombine to the ground states or dissociate again. The photocurrent is formed after the extraction of the free polarons to the respective electrodes.

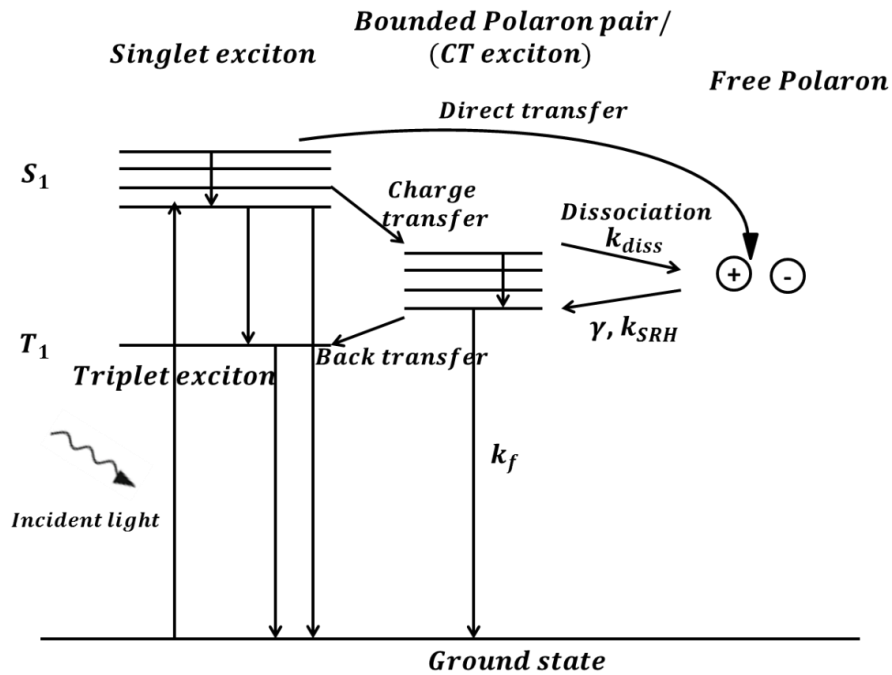


Figure 13. Charge generation and recombination processes found in OPV devices. Diagram redrawn from Ref. 15¹⁵.

This two steps charge generation via an intermediate precursor CT exciton state is first described by Onsager in 1938¹⁶, and then enhanced empirically by Braun in 1984¹⁷. Later the Braun-Onsager model is widely applied to the low mobility system as in OPVs for the description of the charge separation. The separation yield $P(E)$ depends on the electric field E and can be expressed using the CT exciton recombination rate k_f and dissociation rate k_{diss} as

$$P(E) = \frac{k_{diss}(E)}{k_{diss}(E) + k_f} \quad (5.2.1)$$

$k_{diss}(E)$ can be expressed as:

$$k_{diss}(E) = \frac{e\mu}{\varepsilon_r \varepsilon_0} \frac{3}{4\pi a^3} \exp\left(-\frac{E_b}{kT}\right) \cdot \left(1 + b + \frac{b^2}{3} + \frac{b^3}{18} + \dots\right) \quad (5.2.2)$$

in which μ is the sum of the carrier mobilities and ε_r is the dielectric constant; E_b is the binding energy of the CT exciton and equals to $\frac{e^2}{4\pi\varepsilon_r\varepsilon_0 a}$; a is the initial distance of the polaron charges; The last factor in the brackets is the Taylor expansion of a first order Bessel function, with b as the reduced electric field and equals to $\frac{e^3 E}{8\pi\varepsilon_r\varepsilon_0 (kT)^2}$.

5.2.1.1 Geminate Recombination in Low Mobility Semiconductor

The recombination through primary singlet exciton and the bound polaron to the ground state is called the geminate recombination. They are monomolecular recombinations considering that they occur on a bound state where the electron and hole appear in a one to one ratio. The geminate recombination is a first order decay and the recombination rate does not depend on the concentration of the species. The geminate recombination will

usually happen in nanoseconds¹⁸. In annealed blends of P3HT:PCBM, about 5% of singlet excitons cannot reach the donor/acceptor interface and is lost due to geminate recombination¹⁸.

5.2.1.2 Non-geminate Recombination in Low Mobility Semiconductors

The recombination from the free charge carriers to CT exciton states is called non-geminate recombination and the exciton effective lifetime will depend on charge carrier mobilities as well as densities. With respect to different types of non-geminate recombination, the recombination rate will be proportional to different orders of the charge carrier densities. The bimolecular recombination can be expressed by Langevin recombination¹⁹.

5.2.1.3 The Charge Carrier Density and Light Intensity

From the discussion above, we could write out the three continuity equations²⁰ in the charge generation process.

As for singlet exciton we have

$$\frac{dS}{dt} = G_S - R_{rec,S} - D_S \frac{d^2S}{dx^2} \quad (5.2.3)$$

where S is the density of singlet excitons; t is the time scale; G_S is the amount of excitons generated by incident light; $R_{rec,S}$ is the amount of excitons recombines back to the ground state; D_S is the diffusion constant for the singlet excitons and x is the relative position inside the device.

For a bound polaron pair

$$\frac{dP}{dt} = G_X - k_f P - k_{diss} P + \gamma np + \frac{np}{n+p} \quad (5.2.4)$$

where P is the density of bounded polarons; G_X is the amount of bounded polarons generated from singlet excitons; k_f is the recombination rate of bounded polarons into ground state; k_{diss} is the dissociation rate of bounded polarons into free charge carriers; γ is the Langevin prefactor, and $n(p)$ is the carrier density for electrons (holes).

And for charge carrier (hole density is represented here) as

$$\frac{dp}{dt} = k_{diss} P - \gamma np - k_{SRH} \frac{np}{n+p} \quad (5.2.5)$$

in which k_{SRH} is the SRH recombination rate. The second term on the right represents for the bimolecular recombination and the last term represents for the monomolecular recombination.

It can be assumed that after reaching equilibrium under illumination, the concentration of bound polarons and charge carriers should stay stable, thus $\frac{dP}{dt}$ and $\frac{dp}{dt}$ can be set to 0. Also, as being pointed out by Deibel²⁰, the singlet exciton generation and recombination is linearly proportion to the exciton density at low to medium light, only at very high light intensities that the singlet-singlet or singlet polaron quenching will become important. In this case the bounded polaron density can be directly related with the light intensity as

$$G_x = AG \quad (5.2.6)$$

in which G is the light intensity. Combine the two Equations (5.2.4) and (5.2.5), and set the carrier densities as:

$$n = \xi p \quad (5.2.7)$$

where ξ is the difference rate between the electron and hole densities in the system.

When there is only bimolecular recombination in the system, we get

$$p = \sqrt{\frac{Ak_{diss}}{\gamma\xi k_f} G} \quad (5.2.8)$$

and

$$n = \sqrt{\frac{A\xi k_{diss}}{\gamma k_f} G} \quad (5.2.9)$$

for hole and electron density, respectively.

In the case when there is only monomolecular recombination in the system, we have

$$p = \frac{A(1 + \xi)}{\xi} \frac{k_{diss}}{k_{SRH}k_f} G \quad (5.2.10)$$

$$n = A(1 + \xi) \frac{k_{diss}}{k_{SRH}k_f} G \quad (5.2.11)$$

Inserting those expressions for carrier densities into the equation for V_{OC} ²⁰, which will be explained in detail in next chapter (the charge carrier injection barrier is considered to be field dependent lowering only and Richard-Schokley equation was applied), we have

$$V_{OC} = |HOMO_D - LUMO_A| + \frac{kT}{q} \ln \left(\frac{np}{N_V N_C} \right) - \Delta_{low}(E_{c,D}) - \Delta_{low}(E_{c,A}) \quad (5.2.12)$$

in which $HOMO_D$ and $LUMO_A$ are the HOMO level in donor material and LUMO level in acceptor material, respectively; N_V (N_C) is the density of states in donor (acceptor) materials; $\Delta_{low}(E_{c,D})$ is the field dependent barrier lowering at donor/anode interface and $\Delta_{low}(E_{c,A})$ at acceptor/cathode interface.

Thus for monomolecular recombination only system, we get

$$V_{OC} = |HOMO_D - LUMO_A| + 2 \frac{kT}{q} \ln G + \frac{kT}{q} \ln \frac{A^2(1+\xi)^2}{\xi} \left(\frac{k_{diss}}{k_{SRH} k_f} \right)^2 - \Delta_{low}(E_{c,D}) - \Delta_{low}(E_{c,A}) \quad (5.2.13)$$

Thus the light-intensity dependence of V_{OC} for monomolecular recombination is

$$\Delta V_{OC} \sim 2 \frac{kT}{q} \ln \Delta G \quad (5.2.14)$$

For bimolecular recombination only system

$$V_{OC} = |HOMO_D - LUMO_A| + \frac{kT}{q} \ln G + \frac{kT}{q} \ln \frac{A k_{diss}}{\gamma k_f} - \Delta_{low}(E_{c,D}) - \Delta_{low}(E_{c,A}) \quad (5.2.15)$$

Thus the light-intensity dependence of V_{OC} for bimolecular recombination is

$$\Delta V_{OC} \sim \frac{kT}{q} \ln \Delta G \quad (5.2.16)$$

5.2.2 Light Dependence study of ITO-free Flexible Device

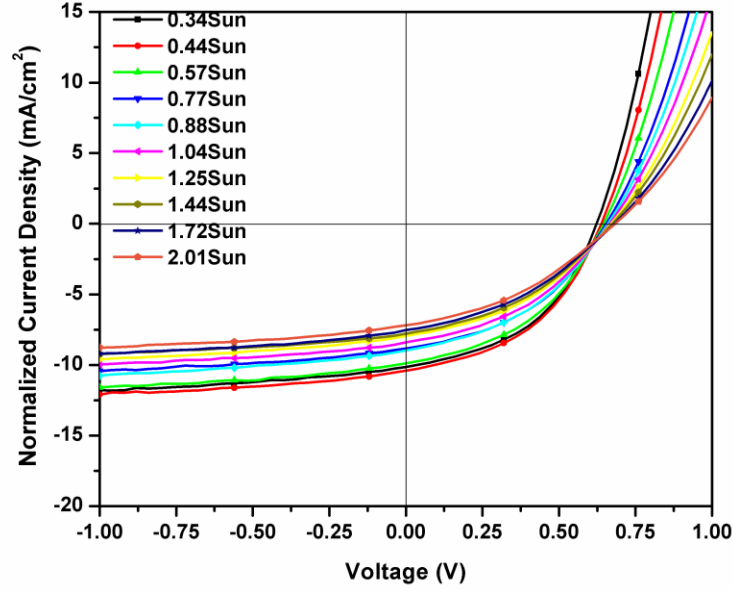


Figure 14. Current density-voltage characteristics for the ITO-free flexible device with a structure of PEN/modified PEDOT:PSS/P3HT:PCBM/Al under different illumination intensity. Here all values of current density were divided by their light intensity, respectively.

The current density-voltage (J-V) characteristics of the ITO-free flexible devices under incident light ranging from 0.34 to 2.01 suns are shown in Figure 14, each current density is divided by the respective light intensity (normalized to 1 sun). As we can see from the trend, the normalized J_{SC} keeps decreasing from 10.3 to 7.16 mA/cm², while V_{OC} increases from 0.625 to 0.684 V, values much higher compared to the V_{OC} of the ITO-based standard devices obtained from our previous work as well as from other groups²¹⁻

²³. The modified PEDOT:PSS has a work function of ~ 5.05 eV, slightly lower than the pristine PEDOT:PSS film of ~ 5.1 eV²⁴. Although it is close to the work function of the ITO substrate ~ 4.7 eV²⁵, the device with the modified PEDOT:PSS shows a higher V_{OC} of ~ 0.1 V, which indicates less voltage loss using the modified PEDOT:PSS/P3HT junction than the ITO/PEDOT:PSS/P3HT:PCBM junction. Under 1 sun illumination intensity, the flexible device exhibits a J_{SC} of 8.38 mA/cm², a V_{OC} of 0.666 V, a FF of 41.1% and a PCE of 2.30% .

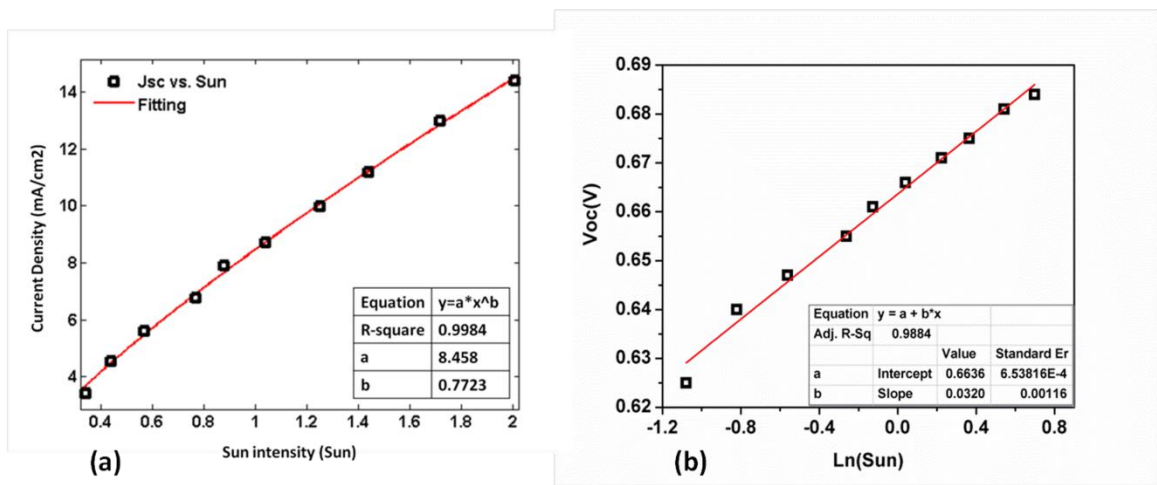


Figure 15. (a) Experimental J_{SC} as a function of light intensity (square symbols); (b) V_{OC} as a function of $\ln(\text{Sun})$ (square symbols) for the ITO-free flexible device with a structure of PEN/modified PEDOT:PSS/P3HT:PCBM/Al. The solid lines denote the fits to the experiment data.

The principal parameters were extracted from the current density-voltage curves of the OPVs and plotted with respect to incident light to study their light dependence properties.

Figure 15(a) shows the photogenerated current density (J_{ph}) under short circuit conditions

as a function of illumination intensity. It is known that for an ideal solar device without any recombination effects, the photogenerated current (I_{ph}) should be linearly proportional to light intensity²⁶ as

$$I_{ph} = A(1 + BT)GS \quad (5.2.17)$$

where G represents the sun intensity; S is the cell area and T is the temperature; A and B are two constant parameters for the PV device. However, in real devices, due to many factors such as the loss from short exciton lifetime, charge carrier mobility mismatch, ineffective band match, isolated phase regions and disordered morphology, photogenerated current follows a power dependence of light intensity (here we assume the electrodes have ideal transport property) of

$$I_{ph} \propto G^\alpha \quad (5.2.18)$$

where α varies from 0.5 to 1 with respect to different recombination processes²⁷⁻³⁰. A power fitting of the experimental data in Figure 15(a) yields $\alpha = 0.7723$, indicating that the losses in the bulk absorber are dominated by bimolecular recombination via free charge carriers or electron-hole pairs. However, a weak contribution of monomolecular recombination can't be excluded.

The light-intensity dependence of V_{OC} also provides independent and complementary information on the recombination details of the PV device. Under short circuit condition, the effective internal electric field reaches a maximum indicating that the highest charge separation efficiency and lowest recombination rate is achieved. While under open circuit conditions, no current is observed and all photogenerated carriers recombine within the

device. In this case the recombination information is equally important in presenting the mechanism details of the device. Figure 15(b) shows a linear relationship between the V_{oc} and the natural logarithm of light intensity with the fitting curve yielding

$$\delta V_{oc} = \beta \frac{k_B T}{q} \ln G \quad (5.2.19)$$

where $\beta = 1.25$, k_B is Boltzmann's constant, T is room temperature (298 K) and q the unit electron charge. As has been interpreted clearly before head, the fit relationship of

$$\delta V_{oc} = 2 \frac{k_B T}{q} \ln G \quad (5.2.20)$$

and

$$\delta V_{oc} = \frac{k_B T}{q} \ln G \quad (5.2.21)$$

are attributed to first-order (monomolecular) and second-order (bimolecular) loss processes, respectively. Correlating with the results from J_{sc} , it is clear that bimolecular recombination dominates the efficiency losses in this ITO-free flexible device, which can be either attributed to the space charge induced by the separated phase region within the device, or to the imbalanced charge carrier collection ability between holes and electrons

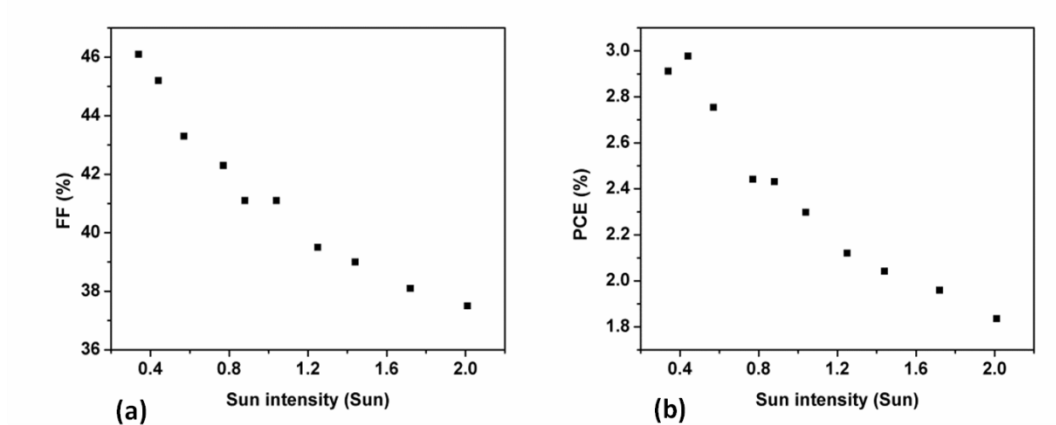


Figure 16. The *FF* (a) and *PCE* (b) as a function of light intensity for the ITO-free flexible solar device with a structure of PEN/modified PEDOT:PSS/ P3HT:PCBM/Al.

As illumination intensity increases, the photo-induced space charge accumulates within the ITO-free device, contributing to an even higher bimolecular recombination rate further impairing device performance. As shown in Figure 16, in accordance with our expected outcome, the *FF* and *PCE* decrease sub-linearly with increasing of illumination intensity. The maximum power output efficiency at the lowest light intensity suggests a potential application of this flexible device under low illumination.

5.2.3 Light Dependence study of ITO-based Standard Device

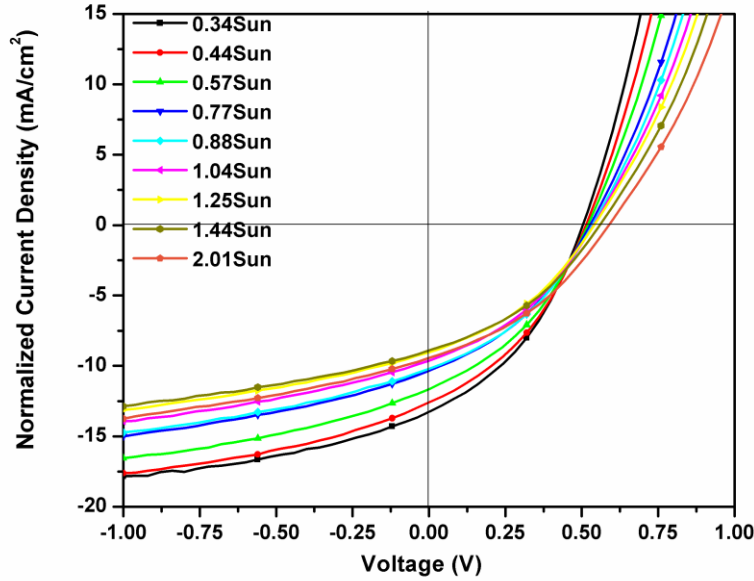


Figure 17. Current density-voltage characteristics for the ITO-based standard device with a structure of ITO/PEDOT:PSS/P3HT:PCBM/Al under different illumination intensity. Here all values of current density were divided by light intensity, respectively.

The J-V characteristics under different illumination intensities for the ITO-based device are shown in Figure 17. The J_{SC} tends to saturate as the light intensity increases. The V_{OC} increases as the intensity of incident light increases but only with a lower value (ranging from 0.506 to 0.589 V) compared to the ITO-free flexible device discussed before. Under 1 sun illumination intensity, the device exhibits a J_{SC} of 9.68 mA/cm², a V_{OC} of 0.540 V, a FF of 36.7 % and a PCE of 1.92 %. Detailed parameters for these two types of devices are listed in Table 5-1 and Table 5-2.

Light Intensity	~1 sun						
	V_{OC} (V)	Normalized J_{SC} (mA/cm ²)	FF (%)	PCE (%)	n	R_s (Ω)	R_{sh} (Ω)
PEDOT:PSS	0.666	8.38	41.1	2.30	6.53	8.84	514.2
ITO	0.54	9.68	36.78	1.92	6.98	7.34	192.2

Table 5-1. Principle parameters for OPVs under light intensity ~1 sun.

Light intensity	0.34-2.01 sun			
	V_{OC} range (V)	J_{SC} range (mA/cm ²)	FF range (%)	PCE range (%)
PEDOT:PSS	0.625-0.684	3.42-14.39	37.5-46.1	1.84-2.91
ITO	0.506-0.589	4.5-19.02	36.42-38.21	2.03-2.56

Table 5-2. Principle parameters for OPVs under the light intensity of 0.34-2.01 sun.

Figure 18 shows the dependence of J_{SC} and V_{OC} for the ITO-based device on illumination intensity. Using the same fitting procedure as for the ITO-free device resulted in values of $\alpha = 0.8442$ and $\beta = 1.60$, indicating that monomolecular recombination due to defects, impurities or even space charges dominate the efficiency losses in the ITO-based standard device compared to the ITO-free device.

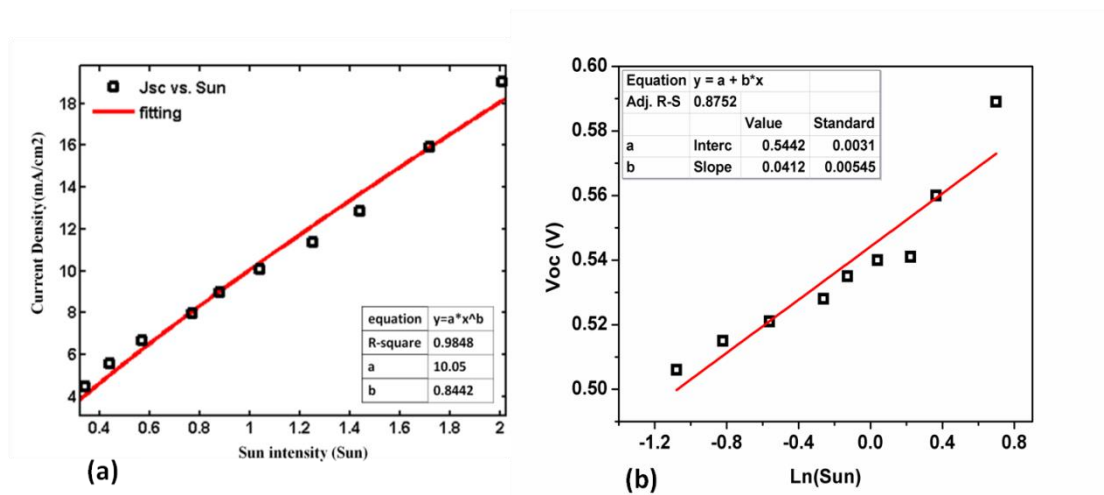


Figure 18. (a) J_{sc} as a function of light intensity (square symbols); (b) V_{oc} as a function of $\ln(\text{Sun})$ (square symbols) for the ITO-based solar device with a structure of ITO/PEDOT:PSS/ P3HT:PCBM/Al. The solid lines denote the fits to the experiment data.

Comparing this set of fitting parameter with the that for the ITO-free device, we can see that by substituting the ITO electrode with modified PEDOT:PSS, more bimolecular recombination is introduced to the system, which can be attributed to the relatively poor electrical transport properties of modified PEDOT:PSS to that of ITO. The modified PEDOT:PSS has a conductivity near 1000 S/cm^{-1} , which is much lower than ITO $\sim 10^4 \text{ S/cm}^{-1}$ ²⁶, and could cause more imbalanced charge carrier transport, increasing the bimolecular recombination. As light intensity increases, the FF and PCE (Figure 19) of the ITO-based device first decrease then remain steady at a constant value, which is in accordance with the monomolecular recombination loss mechanism²⁷, indicating more balanced charge separation and collection in the ITO-based device.

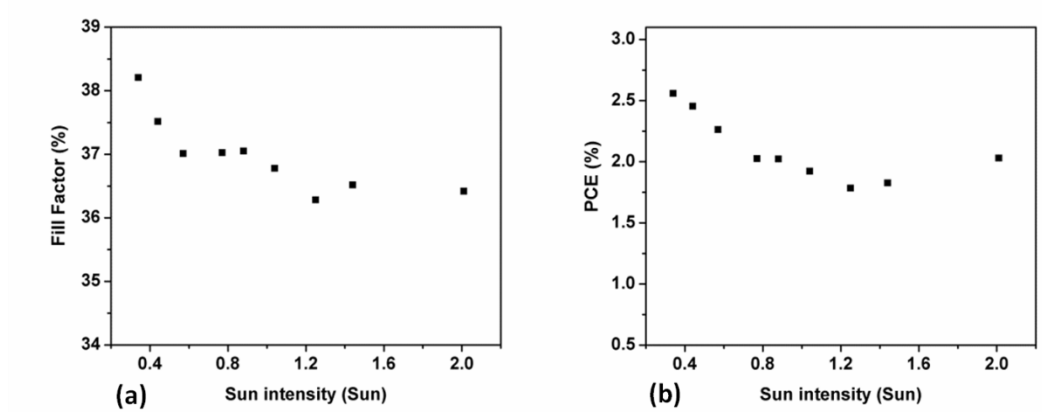


Figure 19. (a) The *FF* and (b) *PCE* as a function of light intensity for the ITO-based solar device with a structure of ITO/PEDOT:PSS/P3HT:PCBM/Al.

5.3 Discussion of Voc Comparison in ITO-based Standard and ITO-free Flexible Device

5.3.1 Energy Shift in Vacuum Level

There are two kinds of vacuum levels illustrating the surface energy level of the conducting/semiconducting material. The vacuum level for an electron stays at a distance infinitely away from the system (vacuum level at infinite distance), denoted as $VL(\infty)$; while the vacuum level for an electron at rest just outside the solid which will be called the vacuum level at surface, denoted as $VL(s)$; Generally, the vacuum level at the surface will be different compared with the vacuum level at a distance infinitely away from the system, resulting from vacuum level shifting either upward or downward at the contact interface.

Considering the contact between a metal and semiconductor, in which the semiconductor is a good insulator. There are only few charge carriers that will be involved in the charge transfer at the contact. In this case Fermi energy alignment cannot be achieved and the vacuum level of the two materials will align.

When both of the two contacting materials have a high enough density of charge carriers, such as between PEDOT:PSS and metal., while they are at a distance x away where no interaction happens between them, the vacuum levels should line at $V_L(\infty)$. As they get closer, the electrons will start to flow from the higher Fermi level (metal) to the lower side. The charge flow will stop after electrostatic equilibrium is reached. At this time the Fermi levels line up on the same level, and the charge diffusion layer which mainly falls in the semiconductor will cause a downward shift of the vacuum level.

The Fermi level alignment is a combination effect of surface dipole and charge transfer. There are various factors that will cause the surface dipole, such as the forming of new bonds by chemical interaction or the rearrangement of the surface adsorption layer. The vacuum level shift by these types of charge redistribution and surface dipole will also need to be taken into the consideration while calculating the charge injection barrier and the direction of the vacuum shift will depend on the case.

5.3.2 Energy Level Alignment at ITO/PEDOT:PSS/Organic Interface

In the work of Greczynski et al. and the work of Kugler et al.³², the effect of PEDOT:PSS on the energy level alignment between ITO and the polymer semiconductors was studied and similar results are found in their works. Without PEDOT:PSS, it was observed that the distance between the vacuum level of the polymer semiconductor and the Fermi level of the ITO, represented by the parameter E_F^{VAC} , increased monotonically upon increasing the ITO substrate work function from 4.4 – 4.8 eV. By plotting the E_F^{VAC} with respect to ITO work function, the slope of $S = \delta E_F^{VAC} / \delta \phi_{ITO}$ was found to approach unity (The shottky-Mott limit), which indicates that the vacuum level alignment holds at the interface regardless of the ITO work function as shown in Figure 20a. Because the voltage loss ΔV_b at the vacuum level is very small, usually less than 0.2 eV on average and is independent of the substrate work function, the hole injection from bis-poly(2-dimethyloctylsilyl-1,4-phenylenevinylene) (DMOS-PPV) to ITO will have an energy loss as

$$\phi_{b,p} \approx \phi_{PEDOT:PSS} - \phi_{ITO} \quad (5.3.1)$$

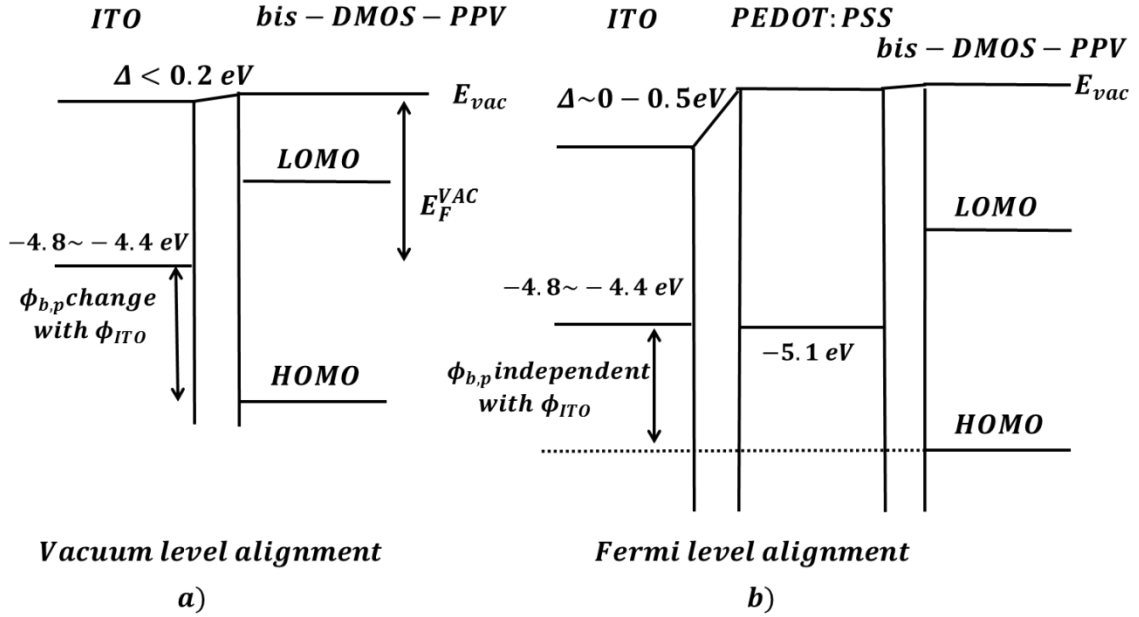


Figure 20. Interfacial energy level at a) ITO/bis-DMOS-PPV and b) ITO/PEDOT:PSS/bis-DMOS-PPV contact. Diagram is drawn according to the information from ref³².

After the insertion of the PEDOT:PSS layer, the slope S is observed to approach 0 (referred as the Bardeen limit), which is an indication that unlike the contact between the polymer donor semiconductor such as PFO or bis-DMOS-PPV with ITO, the PEDOT:PSS always aligns to the Fermi level of the ITO with the potential drop at the vacuum level (Figure 20b). This is due to the high charge density states in PEDOT:PSS, enough charge transfer can be reached to have Fermi level alignment. The energy offset at vacuum level Δ between the ITO and PEDOT:PSS changes from 0-0.5 eV according to the work function of ITO, which could be a result from the formation of a surface dipole layer. The special property of PEDOT:PSS accounts for the general improvement in the

device performance while being used as the interfacial layer between the ITO anode and the polymer layer. The hole injection barrier from PEDOT:PSS to ITO in this case is

$$\phi_{b,p} = \phi_{PEDOT:PSS} - \phi_{ITO} - \Delta \quad (5.3.2)$$

Although the PEDOT:PSS/bis-DMOS-PPV contact was not discussed in detail, it was inferred that the difference between the Fermi level of ITO and the HOMO level for bis-DMOS-PPV always stays at 1.0 eV with no respect to the work function of ITO. It was also noted in Greczynski et al.'s work³³ that the bis-DMOS-PPV lines at the vacuum level with PEDOT:PSS, thus the donor material should be selected to have the similar HOMO level as the Fermi level of PEDOT:PSS in order to minimize the voltage loss or hole transport barrier.

5.3.3 Energy Level Alignment at P3HT:PCBM/Cathode Interface

If a metal is in an intimate contact with P3HT:PCBM, and the Fermi level of the semiconductor and the metal line up after equilibrium, in the situation when the work function of the metal is larger than the Fermi level of the PCBM, there will be an upward shift of the vacuum level in the metal pointing downward into the PCBM due to the lining up of the Fermi levels. Taking vacuum level shift into account, the electron energy loss $\phi_{b,n}$ from PCBM to the cathode will not necessarily be the Fermi level bias $\varphi_{PCBM} - \varphi_{Cathode}$, instead it has the relationship of

$$\phi_{b,n} + \phi_d = |LUMO_{PCBM}| - \phi_{Cathode} \quad (5.3.3)$$

The surface dipole will be positive if the energy level is pointing upward from PCBM to the cathode. In the work of Mihailetchi et al.³⁴, cathode dependence of the V_{OC} was

studied as shown in Figure 21. Au (5.1 eV) and Ag (4.6 eV) were used to make contact with PCBM (3.7 eV in their work). It was found that the PCBM can form a strong interface dipole with the contacting metal, which lowers the electron energy loss at PCBM/Au interface from 1.4 eV to 0.76 eV, and PCBM/Ag from 0.9 to 0.65 eV.

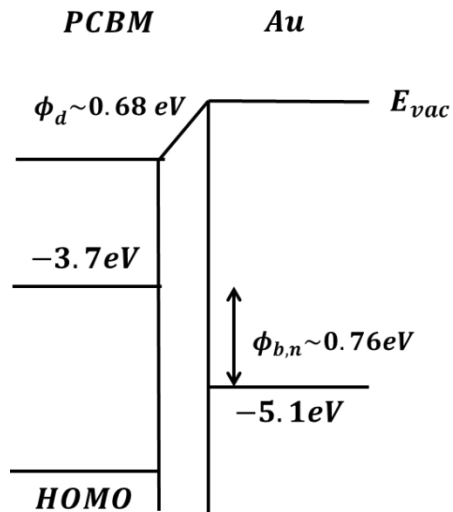


Figure 21. Interfacial energy level at PCMB/Au contact. Diagram is drawn according to the information from Ref 34³⁴.

5.3.4 Voc Comparison in ITO-based Standard and ITO-free Flexible Device

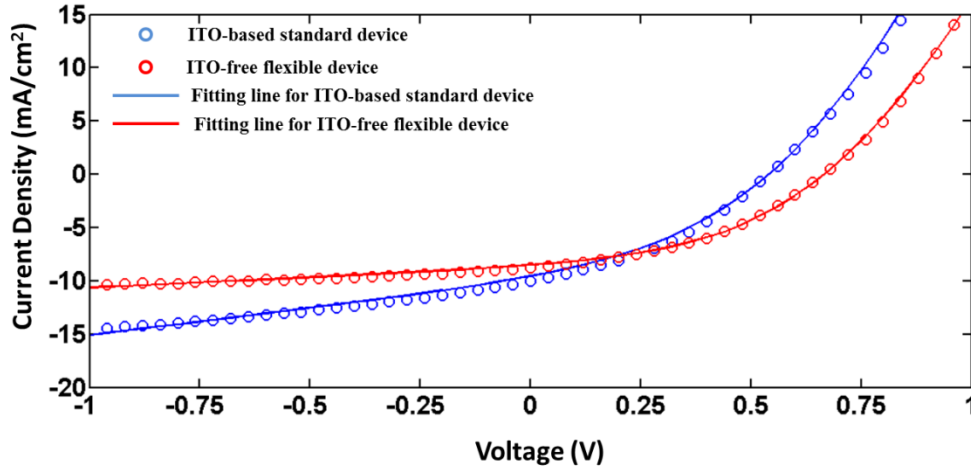


Figure 22. Least square fitting of the current density-voltage curves for both ITO-based standard (blue) and ITO-free flexible (red) devices under ~ 1 sun. The fitting method is the same as in ref³⁵.

In order to have a better understanding of the V_{OC} difference, a fitting model was applied to the J-V curves for both of the devices under ~ 1 sun as shown in Fig. 7. The diode ideality factor (n), R_s and R_{sh} are listed in Table 1. The fitting results clearly show that the two devices have a similar ideality factor and series resistance, whereas the ITO device exhibits a much lower shunt resistance. The lower shunt resistance for ITO-based standard device is due to a higher leakage current and in turn lowers V_{OC} . Besides the structural reason that could have caused the variance in V_{OC} , the work function

modification on PEDOT:PSS by the addition of DMSO may also be an explanation. The hole injection barrier at the ITO/PEDOT:PSS/P3HT junction only depends on the difference between the work functions of PEDOT:PSS and HOMO of P3HT²⁸, and as the work function of modified PEDOT:PSS (~5.0 eV) is ~ 0.1 eV lower than that of the pristine PEDOT:PSS (~5.1 eV)²⁹, this may have resulted in a change of V_{OC} .

5.4 Conclusion

Flexible OPVs were fabricated using modified PEDOT:PSS as anodes resulting in a 20% higher PCE when compared with ITO-based standard devices. In order to study the dynamic process of the photovoltaic devices, a light-intensity study was carried out from 0.34 to 2.01 suns. Light dependence analyses of J_{SC} and V_{OC} suggest PCE losses can principally be attributed to the bimolecular recombination for the ITO-free flexible devices, while losses due to monomolecular recombination are dominant for ITO-based devices. The recombination process is in agreement to the trend for FF and PCE with respect to light intensity in both devices. The values of V_{OC} for flexible devices are higher than the ones in ITO-based devices. The highest efficiency is achieved at the lowest light intensity when the impact of light induced recombination is less dramatic. This suggests the potential for the ITO-free flexible OPVs to operate under low intensity or diffuse light is promising. The absence of the ITO anode makes it easier to fabricate OPVs with lower cost and greater flexibility. The flexibility of the ITO free device makes it more feasible for new and more “unconventional” energy applications.

5.5 Reference

- ¹ S. J. Pearton, *Advanced Materials* **4**, 306 (1992).
- ² F. C. Krebs, M. Jorgensen, K. Norrman, O. Hagemann, J. Alstrup, T. D. Nielsen, J. Fyenbo, K. Larsen, and J. Kristensen, *Solar Energy Materials and Solar Cells* **93**, 422 (2009).
- ³ S. D. Yambem, K.-S. Liao, and S. A. Curran, *Solar Energy Materials and Solar Cells* **95**, 3060 (2011).
- ⁴ S. D. Yambem, A. Haldar, K.-S. Liao, E. P. Dillon, A. R. Barron, and S. A. Curran, *Solar Energy Materials and Solar Cells* **95**, 2424 (2011).
- ⁵ A. M. Nardes, M. Kemerink, M. M. de Kok, E. Vinken, K. Maturova, and R. A. J. Janssen, *Organic Electronics* **9**, 727 (2008).
- ⁶ S.-I. Na, G. Wang, S.-S. Kim, T.-W. Kim, S.-H. Oh, B.-K. Yu, T. Lee, and D.-Y. Kim, *Journal of Materials Chemistry* **19** (2009).
- ⁷ Z. Hu, J. Zhang, Z. Hao, and Y. Zhao, *Solar Energy Materials and Solar Cells* **95**, 2763 (2011).
- ⁸ C. K. Cho, W. J. Hwang, K. Eun, S. H. Choa, S. I. Na, and H. K. Kim, *Solar Energy Materials and Solar Cells* **95**, 3269 (2011).
- ⁹ Y. Zhou, F. Zhang, K. Tvingstedt, S. Barrau, F. Li, W. Tian, and O. Inganas, *Applied Physics Letters* **92**, 233308 (2008).
- ¹⁰ E. M. Conwell and H. A. Mizes, *Physical Review B* **51**, 6953 (1995).
- ¹¹ D. Carsten and D. Vladimir, *Reports on Progress in Physics* **73**, 096401 (2010).

- 12 R. Kersting, U. Lemmer, M. Deussen, H. J. Bakker, R. F. Mahrt, H. Kurz, V. I.
Arkhipov, H. Bässler, and E. O. Göbel, *Physical Review Letters* **73**, 1440 (1994).
- 13 T. Förster, *Annalen der Physik* **437**, 55 (1948).
- 14 D. Moses, A. Dogariu, and A. J. Heeger, *Physical Review B* **61**, 9373 (2000).
- 15 U. Würfel, E. R. Weber, and M. Thorwart, *Quantum Efficiency in Complex
Systems: Organic Solar Cells: From Molecular Aggregates to Organic Solar
Cells* (Elsevier Science Serials, 2011).
- 16 L. Onsager, *Physical Review* **54**, 554 (1938).
- 17 C. L. Braun, *The Journal of Chemical Physics* **80**, 4157 (1984).
- 18 I. A. Howard, R. Mauer, M. Meister, and F. Laquai, *Journal of the American
Chemical Society* **132**, 14866 (2010).
- 19 M. P. a. C. E. Swenberg, *Electronic Processes in Organic Crystals and Polymers,
2nd ed.* (Oxford University Press, New York, 1999).
- 20 D. Cheyns, J. Poortmans, P. Heremans, C. Deibel, S. Verlaak, B. P. Rand, and J.
Genoe, *Physical Review B* **77**, 165332 (2008).
- 21 M. C. Tria, K.-S. Liao, N. Alley, S. Curran, and R. Advincula, *Journal of
Materials Chemistry* **21**, 10261 (2011).
- 22 D. H. Wang, H. K. Lee, D.-G. Choi, J. H. Park, and O. O. Park, *Applied Physics
Letters* **95**, 043505 (2009).
- 23 T. Yamanari, T. Taima, K. Hara, and K. Saito, *Journal of Photochemistry and
Photobiology A: Chemistry* **182**, 269 (2006).
- 24 T. Easwarakhanthan, J. Bottin, A. Ellassi, S. Ravelet, and R. Ravelet, *Solar Cells*
17, 383 (1986).

- 25 D. Gebeyehu, M. Pfeiffer, B. Maennig, J. Drechsel, A. Werner, and K. Leo, *Thin Solid Films* **451–452**, 29 (2004).
- 26 V. Dyakonov, *Thin Solid Films* **451–452**, 493 (2004).
- 27 I. Riedel, N. Martin, F. Giacalone, J. L. Segura, D. Chirvase, J. Parisi, and V. Dyakonov, *Thin Solid Films* **451–452**, 43 (2004).
- 28 S. R. Cowan, N. Banerji, W. L. Leong, and A. J. Heeger, *Advanced Functional Materials* **22**, 1116 (2012).
- 29 S. R. Cowan, A. Roy, and A. J. Heeger, *Physical Review B* **82**, 245207 (2010).
- 30 L. J. A. Koster, V. D. Mihailetschi, H. Xie, and P. W. M. Blom, *Applied Physics Letters* **87**, 203502 (2005).
- 31 H. Ishii, K. Sugiyama, E. Ito, and K. Seki, *Advanced Materials* **11**, 605 (1999).
- 32 T. Kugler, W. R. Salaneck, H. Rost, and A. B. Holmes, *Chemical Physics Letters* **310**, 391 (1999).
- 33 G. Greczynski, T. Kugler, M. Keil, W. Osikowicz, M. Fahlman, and W. R. Salaneck, *Journal of Electron Spectroscopy and Related Phenomena* **121**, 1 (2001).
- 34 V. D. Mihailetschi, P. W. M. Blom, J. C. Hummelen, and M. T. Rispens, *Journal of Applied Physics* **94**, 6849 (2003).
- 35 C. F. Zhang, J. C. Zhang, Y. Hao, Z. H. Lin, and C. X. Zhu, *Journal of Applied Physics* **110** (2011).

6. Anode Conductivity Dependence Study of ITO-free Flexible OPVs under Space-Charge-Limited-Current Condition

6.1 Introduction

In the previous chapter, ITO-free flexible OPV devices were presented and the recombination mechanism within the devices was compared with the ITO-based standard device using a light-intensity study. As a result of the layer structures and materials used in the anode of the two types of devices being different, the devices will be distinct in electrode conductivity, contact resistance and band alignment at the anode electrode junction. It was not certain of how each factor can affect the principle parameters in the device.

In this chapter, a simpler situation is presented. The conductivity of the anode was designed to be the only difference between the two ITO-free flexible devices being compared. By changing the thickness of the highly conductive PEDOT:PSS film, the transport property within the film can be varied. The devices with different anode thicknesses with a device structure of PEDOT:PSS/P3HT:PCBM/Al were fabricated and tested under different light intensities ranging from 0.37 to 2.0 sun. The V_{OC} variance between the devices as well as their changing trends to light intensity in each device was

modeled and explained using the band bending level under different anode conductivity. The other principle parameters were also explained with respect to the changing light intensity. The second section of this chapter introduces the theory of space-charge-limited current (SCLC) which will later be applied to the fitting of J_{SC} vs. light intensity and used to determine the space-charge-limited state in the devices in section 4. Section 3 presents optical, transport and electronic properties of the highly conductive PEDOT:PSS film and it is from there that the parameters are referenced. Section 4 is the discussion of the changing trends in device principle parameters with respect to different light intensity.

6.2 Space-Charge-Limited Current

6.2.1 Space charge and Space-Charge-Limited Current

Space charge is excess electric charge distributed over a region of space, usually occurring in dielectric media such as in a semiconductor material or even vacuum. When the transport properties of the conductive medium or the external field used to extract the charges cannot meet the generation of the charge carriers, space charge accumulates. The presence of the negative or positive space charge in a particular material will also affect the electric field.

In the arrangement¹ of a vacuum diode inserted between a cathode and anode, as shown in Figure 6-1(a), the cathode is heated for sufficient electron emission and an external electric field V is applied between the two electrodes. If the cathode is kept at a low

temperature T_1 then the emitted electrons can all be efficiently collected by the anode, the potential distribution between the cathode and anode is uniform and can be represented by a straight line as shown in Figure 6-1(b). As the temperature of the cathode is increased to T_2 , some electron emission occurs and if it exceeds the rate at which the electrons can be collected by the anode, space charges build up. The negative charge of the electrons depresses the potential in the diode and the potential distribution will be represented by the curve in Figure 6-1(b) instead of a straight line in this case. At this moment the existing potential can still drive the electrons from the cathode to anode. As the cathode temperature is further increased, the space charge will keep accumulating and the potential field will bend even more. At a point of T_3 when the slope of the potential distribution curve at the cathode is zero, a SCLC condition is reached. Part of the generated electrons in the cathode will not be able to be transferred to the anode side by the applied field. With a further rise of the cathode temperature to T_4 , a stage is reached when any emitted electron will not be attracted by the anode. The excess electrons gather in front of the cathode and the electric field at the cathode is reversed.

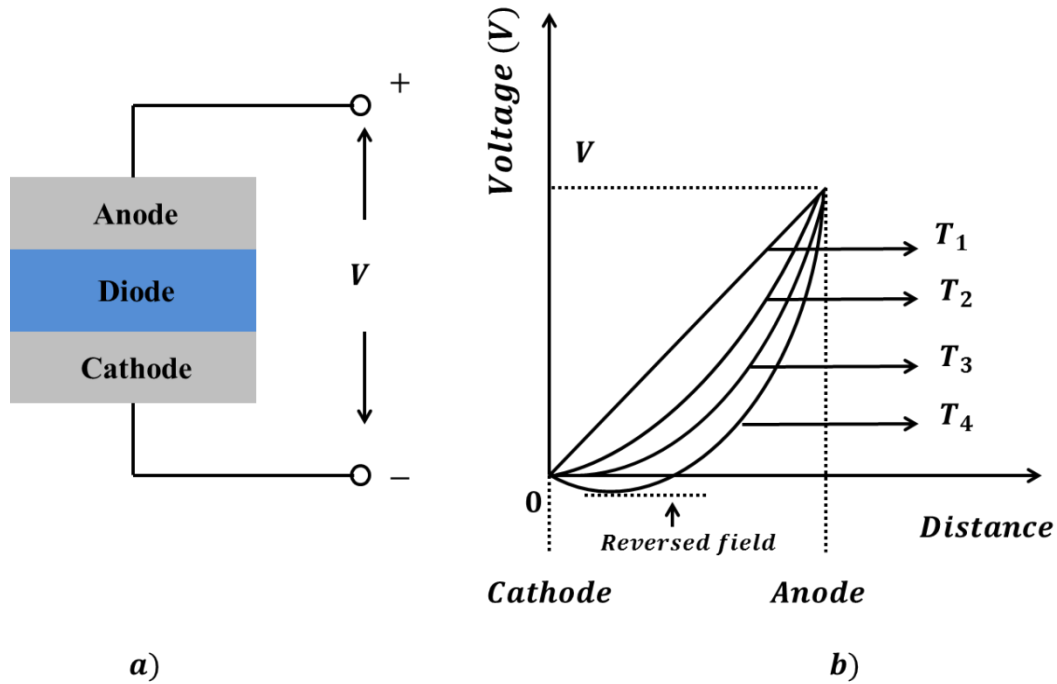


Figure 6-1. a) Schematic draw of a vacuum diode inserted between two parallel electrodes. b) Potential distribution in the diode under difference cathode temperature. Diagrams rearranged from ¹.

For a plane parallel diode with a thickness d , the SCLC inside the diode as a function of the applied external voltage is given by the Child's law² of

$$J_{SCL} = \frac{9}{8} \varepsilon_0 \varepsilon_r \mu \frac{V^2}{d^3} \quad (6.2.1)$$

where ε_0 and ε_r are the dielectric permittivity in the vacuum and in the diode material, respectively; μ is the mobility of the charge carrier; V is the applied external voltage and d is the thickness of the material.

6.2.2 Characteristics of Space-Charge-Limited Current in OPVs

In the OPV devices, the free electron-hole pairs are photogenerated uniformly throughout the specimen. If the charge transport is strongly imbalanced, meaning that either the electron or hole drift length is shorter than the average distance from charge generation sites to the electrode, or one of the drift lengths is much shorter than the other, the electrons or holes will accumulate in the device. Goodman and Rose noted that the photocurrent generated in the ideal OPV devices can be represented as ³:

$$J_{ph} = qGL \quad (6.2.2)$$

where G is the light intensity and L the thickness of the photo-generating layer. They also pointed out that a fundamental limit to the buildup of the space charge in a semiconductor will be reached when the photocurrent generated in this region equals to the SCLC given by

$$J_{SCL} = \frac{9}{8} \varepsilon_0 \varepsilon_r \mu \frac{V^2}{L^3} \quad (6.2.3)$$

where μ represents for the slower charge carrier mobility. Setting Equation (6.2.2) to be equal to equation (6.2.3), we have

$$L = \left(\frac{9\varepsilon_0 \varepsilon_r \mu}{8qG} \right)^{1/4} V^{1/2} \quad (6.2.4)$$

Putting this expression back into the Equation (6.2.2) yields⁴

$$J_{ph} = q \left(\frac{9\varepsilon_0 \varepsilon_r \mu}{8q} \right)^{1/4} G^{3/4} V^{1/2} \quad (6.2.5)$$

It can be seen from Equation (6.2.5) that the value of the SCLC in the OPV device scales with the production of light intensity G to the power of 0.75 and the applied voltage to the power of 0.5 and is governed by the slowest charge carrier mobility.

6.3 Optical, Transport, and Electronic Properties of Modified PEDOT:PSS

6.3.1 UV-visible Spectra of Pristine and Modified PEDOT:PSS

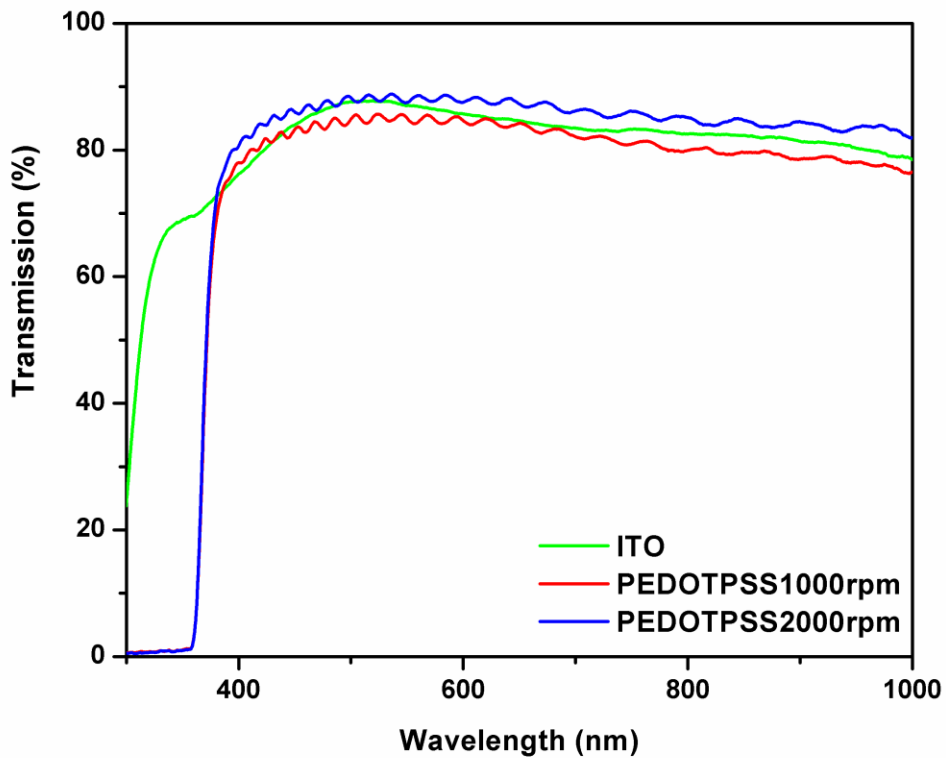


Figure 6-2. UV-visible transmission spectra for ITO slides, modified PEDOT:PSS electrode spin coated on PEN film under the spin speed of 1000 rpm and 2000 rpm.

The characteristic transmission spectra for an ITO slide and modified PEDOT:PSS films fabricated with different spin speeds on PEN substrates are shown in Figure 6-2. The three films show a similar transmission feature for wavelengths larger than 400 nm. The PEDOT:PSS film deposited using a 2000 rpm spin speed demonstrates a transmission ~5% lower than a film fabricated using a 1000 rpm spin speed. Both of them are almost transparent to visible light considering that the PEN film has absorption of around 10%. The modulation fringes on the spectra arise because of an adhesive coating on the PEN film which has been observed earlier¹¹.

6.3.2 Conductivity of Modified PEDOT:PSS with Different Thicknesses

6.3.2.1 The Sheet Resistivity Measured from Experiments

The conductivity measurement was carried out by a two-point-probe picoammeter (Keithley 6487). The sheet resistance of pristine PEDOT:PSS, modified highly conductive PEDOT:PSS spin coated under difference spin speeds and ITO substrate were measured. Each group has been provided with three samples for the data acquisition, the average of the data as well as the standard deviation is given in Table 6-1.

	Pristine PEDOT:PSS	Modified PEDOT:PSS		ITO
Spin Speed	1000 rpm	1000 rpm	2000 rpm	
Sheet resistivity (Ω/\square)	557187	164	286	13
Standard deviation	30855.6	10.8	47.5	0.6

Table 6-1. Sheet resistivity for different conductive films used in the experiment.

The sheet resistivity for ITO slides measured here is very close to the data given by the supplier ($\sim 12 \text{ } \Omega/\text{sq}$). From the data, the pristine PEDOT:PSS film will not be able to be used as an electrode due to its high resistivity, however, the modified PEDOT:PSS under the same spin speed has a resistivity of about 3 orders of magnitude lower than the pristine one and will be conductive enough to extract charge carriers. However, it is still ten times less conductive than an ITO slide, thus the device performance using the modified PEDOT:PSS will be inferior to one based on ITO. Modified PEDOT:PSS films prepared under different spin coating speeds will have different thicknesses thus a different sheet resistance - the thinner the film, the higher the resistivity will be. Devices based upon these films were prepared and studied.

6.3.2.2 The Conductivity Value Used in the analysis

The conductivity of the ITO¹² slides is $\sim 10^6 \text{ S/m}$, the exact value will vary for different preparation methods, temperature and treatment. The conductivity of pristine PEDOT:PSS is $\sim 10^2 \text{ S/m}$, and the conductivity for the modified PEDOT:PSS (Clevios PH 1000) can reach up to 10^5 S/m . Although there is only approximately twice the difference in the sheet resistance between the modified PEDOT:PSS spin coated at 1000 rpm and 2000 rpm, their bulk resistance could have a much higher difference than that of the sheet resistance due to the change in the thickness which can affect the amount of charges it may carry. The conductivity of the cathode material aluminum¹³ is $\sim 3.5 \times 10^7 \text{ S/m}$.

6.3.3 Work Function of Pristine and Modified PEDOT:PSS

The work function of the conductive material can be measured by UV photoemission spectroscopy (UPS)¹⁴ and Kelvin probe methods¹⁵. In the work by Na *et al.*¹⁶, DMSO was also applied as an additive to the PEDOT:PSS (Clevios PH 510), with a concentration range from 0% to 11%. The Kelvin probe method was applied to measure the work function of all the PEDOT:PSS films prepared. Their results are presented in Table 6-2.

	ITO	Modified PEDOT:PSS with different concentration of DMSO			
		0%	3%	7%	11%
Work function (eV)	4.75	5.05	5.03	5.00	4.99

Table 6-2. Work function for ITO and modified PEDOT:PSS. Table arranged from¹⁶.

The work function of the modified PEDOT:PSS decreases almost linearly with respect to the DMSO concentration. Na *et al.* attributed this to the reduced PSS-to-PEDOT ratio at the surface, which lead to an increase in the density of filled states close to the Fermi level^{17,18}. As referenced to work function values from their work, work functions of the pristine, the modified PEDOT:PSS modified by 5 % DMSO and ITO are be ~5.1, ~5.0eV and ~4.8eV, respectively.

6.4 Light-Intensity Study of OPVs under the Effect of Space-Charge-Limited Current

6.4.1 J-V Characteristics of the Flexible OPV Device with Different Thicknesses of Modified PEDOT:PSS Anode

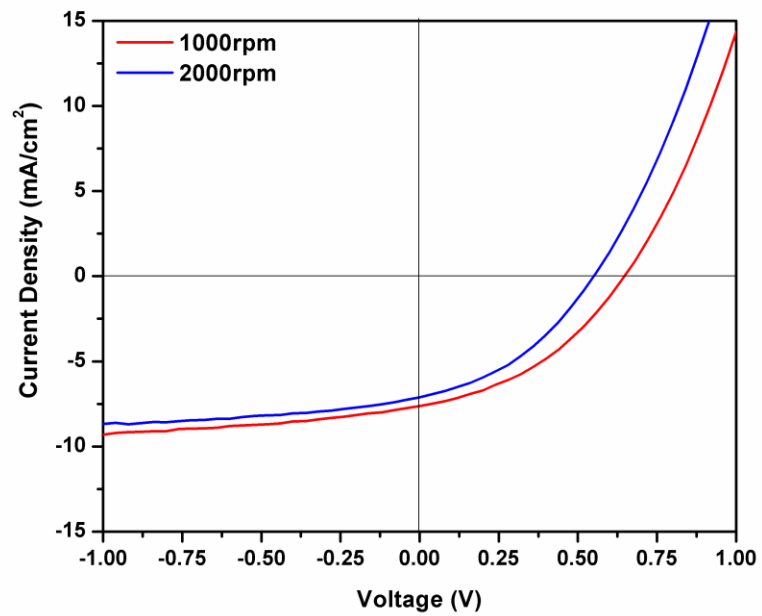


Figure 6-3. J-V characteristics under 1.05 sun for the OPV devices with different thickness of the modified PEDOT:PSS based anodes: 1000 rpm(red) and 2000 rpm(blue line).

The current density-voltage characteristics of the ITO-free flexible devices under ~1 sun with the modified PEDOT:PSS anode are shown in Figure 6-3, also the principle parameters of V_{OC} , J_{SC} , FF and PCE for the two devices under ~1sun are listed in **Table 6-3**. The PEDOT:PSS anodes were spin coated under two different spin speeds (1000 rpm and 2000 rpm). The V_{OC} of the two devices are inversely proportional to the film spin speed: the V_{OC} of the 2000 rpm device has a 14.6% decrease compared to that of the device fabricated using a 1000 rpm spin speed. The device with a less conductive anode also shows a 22.7% decrease in PCE and a slight decrease in J_{SC} and FF . The performance difference is attributed to the transport property of the anode — the only difference between the two devices. In order to understand how the conductivity affects the device different light intensities were applied to these two devices. This enabled the investigation of the dependence of the principle parameters on illumination intensity. In **Table 6-4** all principle parameters for both devices under different light intensities are listed.

	V_{OC} (V)	J_{SC} (mA/cm ²)	FF (%)	PCE (%)
1000 rpm	0.645	7.62	39.47	1.85
2000 rpm	0.551	7.09	38.40	1.43

Table 6-3. Principle parameters for the ITO-free flexible devices with the modified PEDOT:PSS anode under ~1 sun.

	1000 rpm				2000 rpm			
Light intensity (Sun)	Voc (V)	Jsc (mA/cm ²)	FF (%)	PCE/P ⁰ (%)	Voc (V)	Jsc (mA/cm ²)	FF (%)	PCE/P ⁰ (%)
0.37	0.604	3.43	42.96	2.41	0.559	3.42	43.94	2.27
0.58	0.618	4.83	41.54	2.14	0.557	4.73	40.99	1.86
0.72	0.625	5.79	40.62	2.04	0.555	5.91	39.63	1.81
0.91	0.635	6.7	39.72	1.86	0.555	6.31	39.12	1.51
1.05	0.645	7.62	39.47	1.85	0.551	7.09	38.40	1.43
1.22	0.648	8.39	38.63	1.72	0.545	7.55	37.67	1.27
1.43	0.654	10.02	37.54	1.72	0.542	9.58	36.59	1.33
1.68	0.657	10.6	37.48	1.55	N/A	N/A	N/A	N/A
2	0.665	12.86	36.02	1.54	0.529	11.81	34.57	1.08

Table 6-4. Principle parameters for the two devices under different light intensity.

6.4.2 Light-Intensity Study of the OPV Device under Short Circuit Current Condition

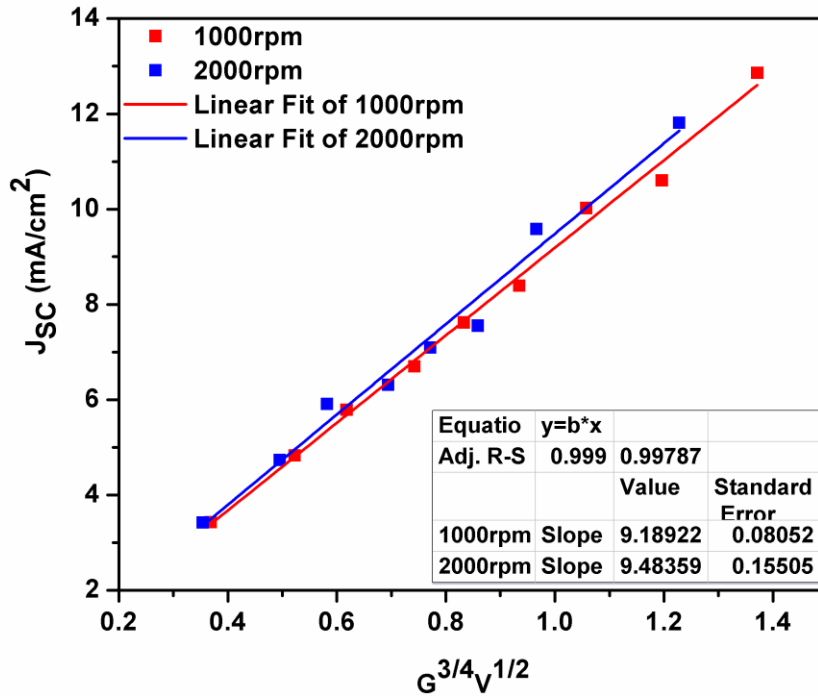


Figure 6-4. The short current density as a function of light intensity and build in effective voltage for the OPV devices with different thickness of the modified PEDOT:PSS based anodes: 1000 rpm (red square) and 2000 rpm (blue square).

The light dependence study of the flexible device was carried out by varying the light intensity from 0.34 sun to 2 sun, which gives a current density range of 3.43 - 12.86 mA/cm² for the 1000 rpm group and 3.42 - 11.81 mA/cm² for the 2000 rpm group, and generally the current densities for the device with less conductive anode are slightly smaller. The power fitting of current density to the light intensity of $J \sim G^\alpha$ was also

applied. The scaling exponent factors are 0.7826 for the 1000 rpm group and 0.7433 for the 2000 rpm group, which are close to the value of $\alpha = 0.75$, a featured value indicating the existence of SCLC¹⁹. Introduced at the beginning of this chapter, when space limited current is reached in the OPV device, the current density has a linear dependence on the production of $G^{3/4}$ and $V^{1/2}$ as expressed by⁴:

$$J_{ph} = q \left(\frac{9\varepsilon_0\varepsilon_r\mu}{8q} \right)^{1/4} G^{3/4} V^{1/2} \quad (6.4.1)$$

where ε_0 and ε_r are the dielectric permittivity in the vacuum and in the diode material, respectively; and μ represents for the slower charge carrier mobility; V is the effective internal voltage. A plot of the current densities for the two devices as a function of $G^{3/4}V^{1/2}$ is shown in Figure 6-4. A linear relationship between the two parameters is found for both devices with a similar fitting value.

The linear fitting of the current density to $G^{3/4}V^{1/2}$ indicates that the SCLC is reached even in the device with a relatively higher conductive anode. In the metal-diode-metal system used in the space-charge effect study introduced previously, after reaching SCLC, the excess injection electrons will start to form a reversed potential near the injection side which will prevent the electrons from traveling to the cathode. Thus for the fabricated OPV devices, when more charge carriers are generated over the SCLC, the charge extraction efficiency is lowered, resulting in a relatively smaller value of current density/Sun intensity. As seen in Table 6-4, at low light intensities when the photogenerated charge densities are still low, the difference in current densities between

the two devices is small; while as the light intensity increases, the charge densities begin to increase and give a larger J_{SC} difference.

6.4.3 Light-Intensity Study of the OPV Devices under Open Circuit Voltage Condition

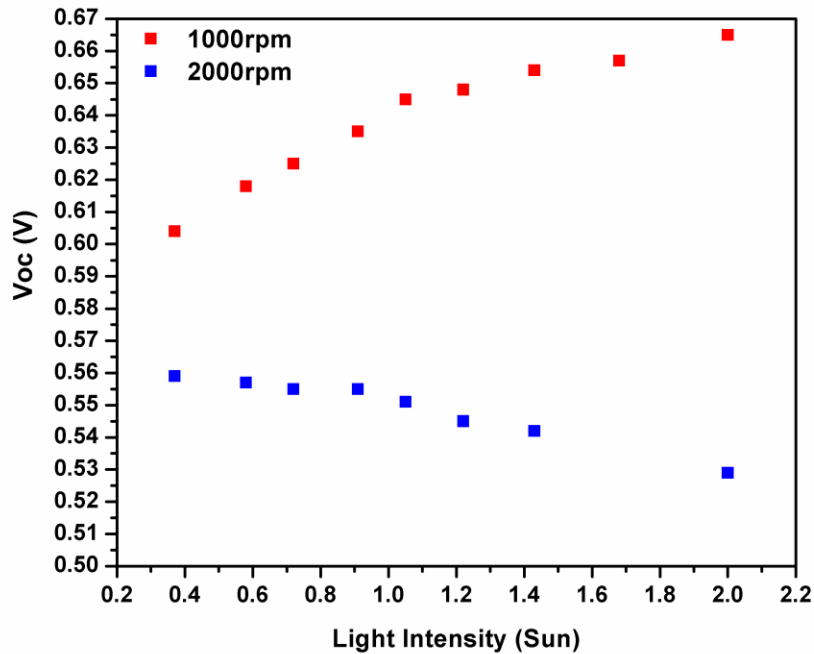


Figure 6-5. The V_{OC} as a function of light intensity for the OPV devices with different thickness of the modified PEDOT:PSS based anodes: 1000 rpm (red square) and 2000 rpm(blue square).

The V_{OC} for the two devices were extracted and plotted out over light intensity in Figure 6-5. Starting from a higher value at the lowest light intensity of 0.37 sun, the ITO-flexible device with the anode spin coated under 1000 rpm shows an increase in the V_{OC} as the

light intensity increases, from 0.604 to 0.665 V; while for the device spin coated under 2000 rpm, the V_{OC} decreases as light intensity increases, dropping from 0.559 V to 0.529 V.

Since the only effective difference designed into the two groups of devices is the conductivity of the two modified PEDOT:PSS anodes, the variance in transport properties must have given a different charge carrier distribution in the two devices.

A modified planarized model for OPV devices by Cheyns et al.¹⁰ was applied to explain the V_{OC} changing trend here. As seen in Figure 6-6, a carrier will be generated at the interface of donor and acceptor material, the distribution of the charge carriers along the device causes bending of the electrostatic potential — BB_D in the donor and BB_A in the acceptor. At the anode/donor contacts, the combination effect of interface dipole (or pinning effect) and the potential offset between the anode work function with the organic energy level will result in the potential difference $\Delta\phi_D$. At the acceptor/cathode contact that value is $\Delta\phi_A$. Note that Δ is the potential difference of right to left, and a positive sign will lead to a loss in energy during charge transfer to electrodes, and a negative sign means gains in energy.

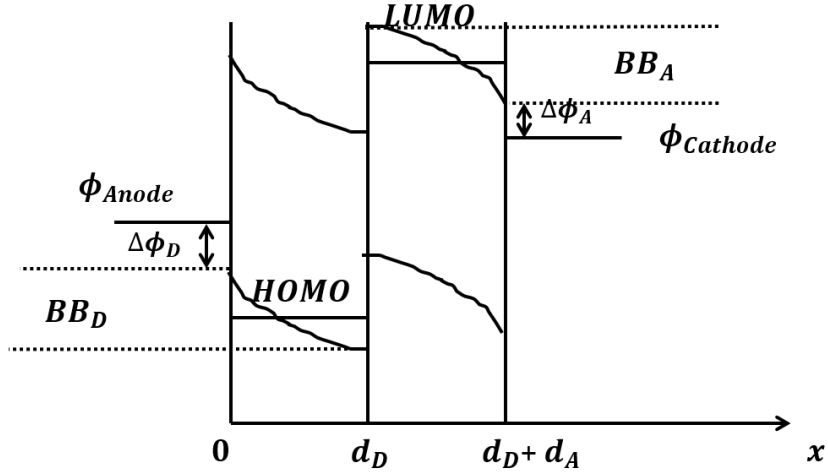


Figure 6-6. Schematic energy diagram of a planar heterojunction solar cell in the work from¹⁰.

The expression of the V_{OC} is

$$V_{OC} = |HOMO_D - LUMO_A| - BB_D - BB_A - \Delta\phi_D - \Delta\phi_A \quad (6.4.2)$$

where $|HOMO_D|$ is the HOMO level of the donor material, $|LUMO_A|$ is the LUMO level of the acceptor material. Applying the transport equation under electro-static equilibrium ($J_p = 0$) we get¹⁰

$$\begin{aligned} BB_D &= V_i - V_D \\ &= - \int_0^{d_D} E(x) dx \\ &= - \int_{p_c}^{p_i} \frac{k_B T}{q p} dp = \frac{kT}{q} \ln\left(\frac{p_c}{p_i}\right) \end{aligned} \quad (6.4.3)$$

where k_B is the boltzman constant; T is the temperature; q is the elementary charge unit; p_i is the hole density at the donor/acceptor interface for a planarized OPV, and p_C is the hole density at the anode/P3HT contact. Similarly we can get the expression for BB_A

$$BB_A = \frac{kT}{q} \ln \left(\frac{n_C}{n_i} \right) \quad (6.4.4)$$

Thus

$$BB_D + BB_A = \frac{kT}{q} \ln \left(\frac{p_C n_C}{p_i n_i} \right) \quad (6.4.5)$$

Putting Equation (6.4.5) back to (6.4.2) we can write

$$V_{OC} = (|HOMO_D - LUMO_A|) + \frac{kT}{q} \ln \left(\frac{p_i n_i}{p_C n_C} \right) - \Delta\phi_D - \Delta\phi_A \quad (6.4.6)$$

	HOMO (eV)	LUMO (eV)
P3HT ^a	-5.1	-3.2
PCBM ^a	-6	-4.2
	Work function	
Modified PEDOT:PSS ^b	-5.0	
Al ^a	-4.3	

Table 6-5. Parameters for the flexible OPV device. ^a The values are from ²⁰. ^b The value is from ¹⁶, ^c The values are from ^{20,21} .

In order to use this model to explain the V_{OC} trend in our experiment, a few observations are required:

1. As a result of the Fermi level of the modified PEDOT:PSS (~ -5.0 eV from Table 6-5) is very close to the HOMO level of P3HT (~ -5.1 eV from Table 6-5) an Ohmic contact can be formed between the two materials²². The density of charge carriers in PEDOT:PSS is relatively high to allow enough charge transfer with the contacting material, thus when the hole density in the P3HT material is relatively high, the PEDOT:PSS can always establish energy alignment with the P3HT at the contacting interface^{23,24}. It is also assumed here that the potential loss $\Delta\phi_D$ at PEDOT:PSS/P3HT contact stays as a constant even if the energy level of P3HT changes.
2. Similarly because the Fermi level of Aluminium cathode (~ -4.2 eV from Table 6-5) is very close to the LUMO level of PCBM (~ -4.3 eV from Table 6-5), and additionally PCBM has a high tendency to form a strong dipole with the contacting metal²², it is assumed that the energy level of aluminum can always line up with that of the PCBM at interface, so the $\Delta\phi_A$ can be considered as a constant.
3. It has been explained in the previous section that if there only is bimolecular recombination in the device, the charge carrier density at the generation interface is proportional to the square root of light intensity G as²⁵

$$n_i = p_i \propto (G)^{1/2} \quad (6.4.7)$$

If there only is monomolecular recombination, the carrier density should be linearly proportional to the light intensity as²⁵

$$n_i = p_i \propto G \quad (6.4.8)$$

Thus the production of the hole and electron density should have a power dependence of light intensity with an exponent scale α such that

$$n_i * p_i \propto (\sqrt{G})^\alpha, \quad 2 < \alpha < 4 \quad (6.4.9)$$

The value of α will depend on the recombination mechanism in the device.

4. Considering the deficiency in the charge transport which causes the SCLC, it is assumed that the carrier densities at the electrode/organic contact are proportional to the power law of light intensity as:

$$n_D * p_D \propto \sqrt{G}^\beta, \quad \beta > 0 \quad (6.4.10)$$

The scale value β will depend on the transport properties of the specific device, for which higher value indicates a less efficient charge extraction to the electrodes.

Taking into account these factors, it is possible to simplify Equation (6.4.6) as:

$$V_{OC} = |HOMO_D - LUMO_A| + \frac{kT(\alpha - \beta)}{2q} \ln(\kappa G) - C \quad (6.4.11)$$

Using the parameters from Table 6-5, and taking the energy loss C to be 0.3 eV at the lowest light intensity we have the final expression

$$V_{OC} = 0.6 + \frac{kT(\alpha - \beta)}{2q} \ln(\kappa G) \quad (6.4.12)$$

κ is an adjustment coefficient here. Figure 6-7 shows a simulation of V_{OC} versus light intensity, the κ value is fixed to 10. The different curves correspond to different $\alpha - \beta$ values. It can be seen that when $\alpha - \beta > 0$, V_{OC} increases as light intensity increases; while $\alpha - \beta < 0$, V_{OC} decreases.

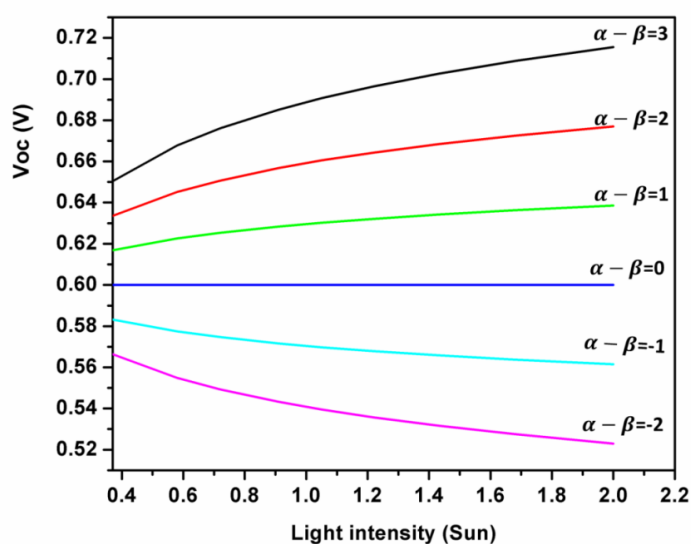


Figure 6-7. Modeled V_{OC} vs. light intensity under the effect of different value of $\alpha - \beta$.

Observing these curves it may be evident that when the speed of the charge collection at the electrode/organic interface is slower than the generation of the charge carriers, space charge will be accumulated at the contacts. In this case there will be a potential drop ΔV_s caused by the space charges at the contact, also if the light intensity increases, there will be a potential increase ΔV_p resulting from the increasing of the photogenerated charge

carriers. When $\alpha - \beta > 0$ which means that net potential change across the device $\Delta V_{OC} = \Delta V_S + \Delta V_p$ is a positive value, V_{OC} increases as we increase the light intensity; When $\alpha - \beta < 0$, the increase in the potential $|\Delta V_p|$ cannot overcome the potential drop $|\Delta V_S|$ due to the accumulation of the space charge, the net change in ΔV_{OC} will be a negative value thus the V_{OC} will be decrease with the increase of the light intensity, as seen in Figure 6-8.

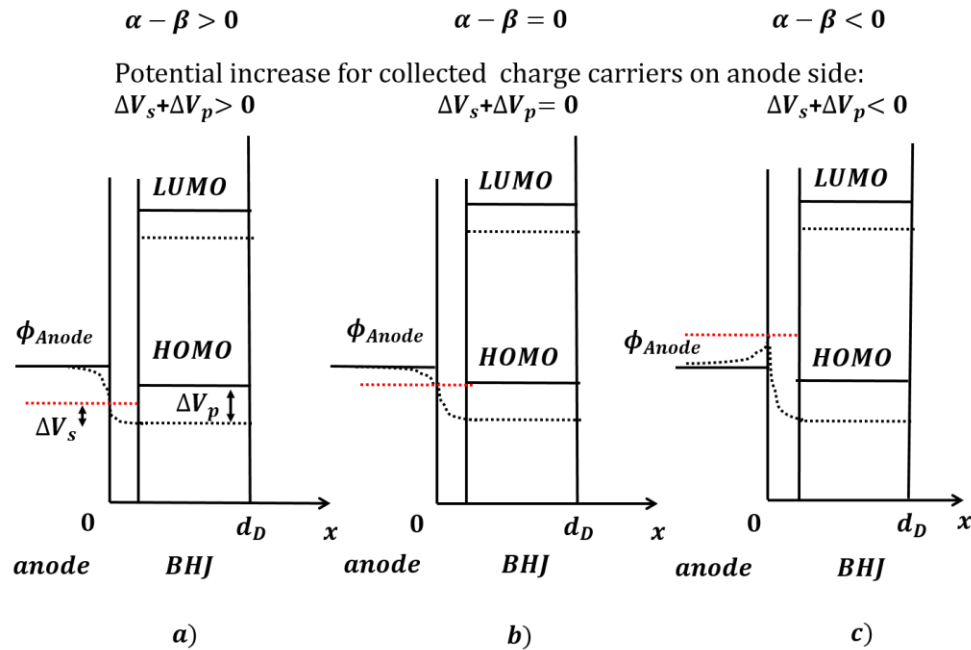


Figure 6-8. Energy band bending within devices with a) $\alpha - \beta > 0$ and b) $\alpha - \beta < 0$. In the diagram, dashed curves represent for the energy levels under a higher light intensity and solid curves for a lower light intensity; ΔV_S is the potential drop if photogenerated holes flow through the inversed potential barriers at anode contact caused by the space charges, ΔV_p is the potential increase caused by the increase amount of photogenerated charge carriers from increasing light intensity. Here we assume the HOMO band is uniform inside the photoactive layer.

As a result of the two flexible OPVs having different anode transport abilities, they should have different values for $\alpha - \beta$ and k . Here k will only decide the y position of the whole $V_{OC} \sim G$ curve under the same value of $\alpha - \beta$, thus we only consider it as a minor fitting parameter for a particular device. Applying this model to the two flexible OPV devices, the fitting results obtained are shown in Figure 6-9. It is clearly shown that the model fits the experimental data very well. The device with a less conductive anode has a negative $\alpha - \beta$ value ($\alpha - \beta = -1.3176$), which indicates a more unbalanced charge transport ability over charge generation property. Also when under the same light intensity, the V_{OC} will be lower for device with less conductive anode. The $\alpha - \beta$ value for the other device ($\alpha - \beta = 2.8865$) is a positive value, which means the increase in the potential caused by the generation of the charge carriers can still overcome the energy loss from the space-charge accumulation.

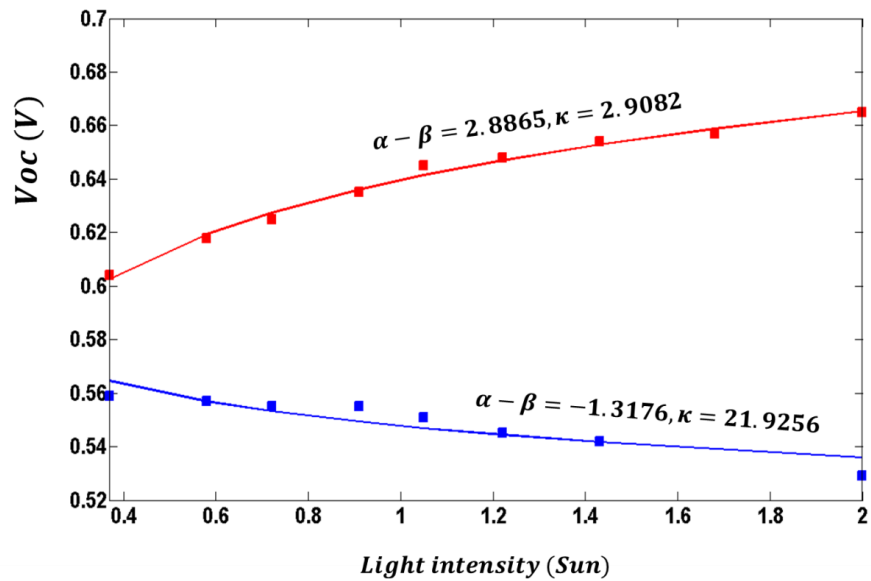


Figure 6-9. V_{oc} versus light intensity for the flexible device with the anode of modified PEDOT:PSS spin coated under 1000 rpm (red) and 2000 rpm (blue). Square: experiment data; Line: fitting curve.

6.4.4 Light-Intensity Study of the OPV Devices for Fill Factor and Efficiency

The trends of FF and PCE over light intensity are in agreement of our previous analysis. For both devices, the increasing light intensity will result in the decreasing of the FF and PCE ; As light intensity increases, more charge carriers will accumulate in the device which has already reached a space-charge-limited condition, thus more detriments will be introduced by higher charge recombination, resulting in a decreasing FF and PCE . Also, comparing between the two types device, the device with higher anode conductivity performs better due to a more efficient transport capability as shown in Figure 6-10.

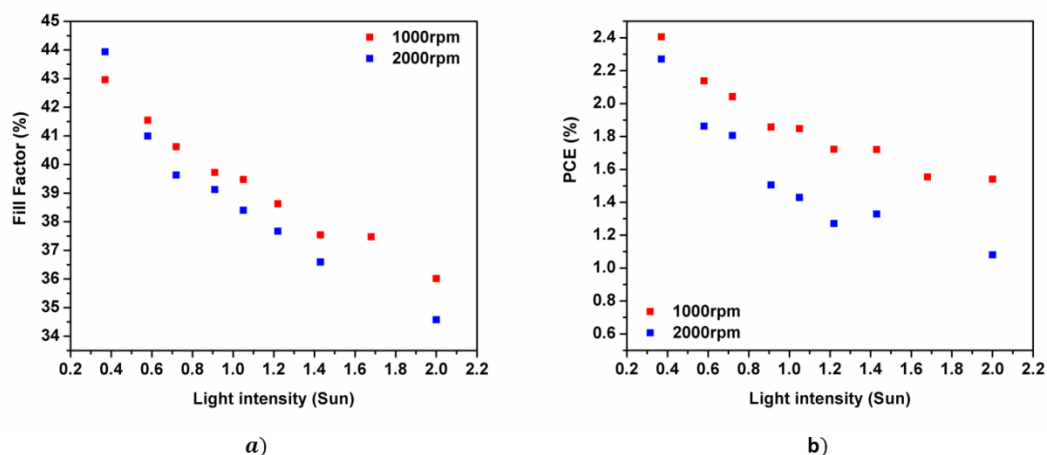


Figure 6-10. a) *FF* and b) *PCE* versus light intensity.

6.5 Conclusion

ITO-free flexible OPV devices with a structure of PEDOT:PSS/P3HT:PCBM/Al were fabricated using highly conductive PEDOT:PSS films with different thickness. Under 1 sun the device with PEDOT:PSS spin coated at 1000 rpm showed a V_{OC} of 0.645 V, J_{SC} 7.62 mA/cm², *FF* 39.47 % and *PCE* 1.85 %. The device with PEDOT:PSS spin coated at 2000 rpm showed a slightly degraded performance, with V_{OC} of 0.551 V, J_{SC} 7.09 mA/cm², *FF* 38.4 % and *PCE* 1.43 %. It is clear that the conductivity mainly affects the V_{OC} of the device. In order to have a deeper understanding of the change in device performance introduced by the anode conductivity variance, light-intensity study was carried out from 0.37 to 2.0 suns. Light dependent analysis of J_{SC} suggests that SCLC condition is reached in both devices. The energy band bending due to the excess space charge carrier explains the V_{OC} variance between the two devices. It also explains their

different responses to changes in the light intensity. The decreasing trend of FF and PCE with respect to light intensity is explained by the lower charge collection to generation rate in both devices.

6.6 References

- ¹ D. Chattopadhyay, *Electronics (fundamentals And Applications)* (New Age International (P) Limited, 2006).
- ² C. D. Child, *Physical Review (Series I)* **32**, 492 (1911).
- ³ A. M. Goodman and A. Rose, *Journal of Applied Physics* **42**, 2823 (1971).
- ⁴ V. D. Mihailetschi, J. Wildeman, and P. W. M. Blom, *Physical Review Letters* **94**, 126602 (2005).
- ⁵ H. Antoniadis, B. R. Hsieh, M. A. Abkowitz, S. A. Jenekhe, and M. Stolka, *Synthetic Metals* **62**, 265 (1994).
- ⁶ C. J. Brabec, A. Cravino, D. Meissner, N. S. Sariciftci, T. Fromherz, M. T. Rispens, L. Sanchez, and J. C. Hummelen, *Advanced Functional Materials* **11**, 374 (2001).
- ⁷ A. Gadisa, M. Svensson, M. R. Andersson, and O. Inganäs, *Applied Physics Letters* **84**, 1609 (2004).
- ⁸ M. C. Scharber, D. Mühlbacher, M. Koppe, P. Denk, C. Waldauf, A. J. Heeger, and C. J. Brabec, *Advanced Materials* **18**, 789 (2006).
- ⁹ J. Liu, Y. Shi, and Y. Yang, *Advanced Functional Materials* **11**, 420 (2001).
- ¹⁰ D. Cheyns, J. Poortmans, P. Heremans, C. Deibel, S. Verlaak, B. P. Rand, and J. Genoe, *Physical Review B* **77**, 165332 (2008).
- ¹¹ S. J. Wakeham, M. J. Thwaites, B. W. Holton, C. Tsakonas, W. M. Cranton, D. C. Koutsogeorgis, and R. Ranson, *Thin Solid Films* **518**, 1355 (2009).

- ¹² H. Izumi, T. Ishihara, H. Yoshioka, and M. Motoyama, *Thin Solid Films* **411**, 32 (2002).
- ¹³ R. A. Serway, *Principles of Physics* (Saunders College Publishing, 1998).
- ¹⁴ L. Apker, E. Taft, and J. Dickey, *Physical Review* **74**, 1462 (1948).
- ¹⁵ D. P. Woodruff and T. A. Delchar, *Modern Techniques of Surface Science* (Cambridge University Press, 1994).
- ¹⁶ S.-I. Na, G. Wang, S.-S. Kim, T.-W. Kim, S.-H. Oh, B.-K. Yu, T. Lee, and D.-Y. Kim, *Journal of Materials Chemistry* **19** (2009).
- ¹⁷ T.-W. Lee and Y. Chung, *Advanced Functional Materials* **18**, 2246 (2008).
- ¹⁸ S.-I. Na, G. Wang, S.-S. Kim, T.-W. Kim, S.-H. Oh, B.-K. Yu, T. Lee, and D.-Y. Kim, *Journal of Materials Chemistry* **19**, 9045 (2009).
- ¹⁹ L. J. A. Koster, M. Kemerink, M. M. Wienk, K. Maturová, and R. A. J. Janssen, *Advanced Materials* **23**, 1670 (2011).
- ²⁰ T. Oku, S. Nagaoka, A. Suzuki, K. Kikuchi, Y. Hayashi, H. Inukai, H. Sakuragi, and T. Soga, *Journal of Physics and Chemistry of Solids* **69**, 1276 (2008).
- ²¹ L. J. A. Koster, V. D. Mihailetschi, and P. W. M. Blom, *Applied Physics Letters* **88** (2006).
- ²² V. D. Mihailetschi, P. W. M. Blom, J. C. Hummelen, and M. T. Rispens, *Journal of Applied Physics* **94**, 6849 (2003).
- ²³ T. M. Brown, J. S. Kim, R. H. Friend, F. Cacialli, R. Daik, and W. J. Feast, *Applied Physics Letters* **75**, 1679 (1999).

- ²⁴ G. Greczynski, T. Kugler, M. Keil, W. Osikowicz, M. Fahlman, and W. R. Salaneck, *Journal of Electron Spectroscopy and Related Phenomena* **121**, 1 (2001).
- ²⁵ A. M. Nardes, M. Kemerink, M. M. de Kok, E. Vinken, K. Maturova, and R. A. J. Janssen, *Organic Electronics* **9**, 727 (2008).

7. Conclusions

This dissertation aims to investigate alterations both in the structure and materials used in standard OPV devices and study how the changing parameters affect the physics and performance of the device.

7.1 P3HT:PCBM Interfaces

The donor/acceptor interface is a very critical parameter in OPV devices as it is the location where excitons must diffuse to in order to be separated into free electrons and holes. In this dissertation, the effects of modifying the structure of the P3HT/PCBM interfacial were investigated¹. A p-n junction structure was fabricated using a dynamic spin coating deposition step. The interfacial morphology was controlled by using solvents for PCBM with different boiling points. AFM measurements were studied for the p-n junction interfaces and a morphological change from a low level inter-digitated structure to flat contact was achieved. During deposition of the PCBM layer, the solution with the lower boiling point evaporates more quickly creating craters in the P3HT layer before dissolving and removing too much of the original P3HT surface. The device performance is strongly correlated with the P3HT/PCBM interface morphology. A slight increase in the interface roughness can result in a significant increase in the performance of the p-n junction device. This was particularly evident in the J_{SC} , which can be a direct result of more excitons generated at the donor/acceptor interface. Unlike in the bulk-heterojunction OPV, device performance can be improved more systematically in a p-n

junction device by increasing the donor/acceptor interface area without sacrificing the charge collection efficiency. In future work, studies focusing on increasing the diffusion length through modeling and selection of new molecules as well as modifying the interface contact in a p-n junction OPV device may yield some significant improvements.

7.2 Replacement and Modification of the Anode and Hole Transport Layer

7.2.1 Replacement with Electropolymerized PEDOT:PSS

The degradation study on ITO /spin coated PEDOT:PSS anode junctions has been carried out in our previous works². OPV devices using SPEDOT:PSS as a HTL has been shown to have poor stability. A 10 day exposure time to air for the ITO/SPEDOT:PSS junction resulted in a 90 % drop in *PCE*. The acidic nature of PSS is considered as the main cause of degradation of the ITO electrodes. In this dissertation, electro-polymerization was used to deposit the PEDOT:PSS instead of spin coating³, and EPEDOT:PSS was shown to have an increase by a factor of 2.34 in the PEDOT:PSS ratio compared to that of the SPEDOT:PSS verified by XPS studies. The performance of the 0 day devices after fabrication between the two types of device are comparable and very similar. However, stability is significantly improved for the 10 day degradation study. The EPEDOT:PSS based device showed no change in the performance. The XPS results for a 15 day degradation study group of EPEDOT:PSS/ITO junction were consistent with the device performance. The atomic concentration of indium atomic ion in the EPEDOT:PSS layer remained below 0.45 % and thus is considered stable after 7 days exposure to air. This

confirms that the decrease of the PSS amount is the reason for the stability improvement. EPDOT:PSS is demonstrated as a very good substitution and a technique for fabricating a suitable HTL.

7.2.2 Replacement with Highly Conductive PEDOT:PSS

Highly conductive PEDOT:PSS was used to replace the ITO/PEDOT:PSS anode junction for OPV devices as the ITO-free device can eliminate the inherent problems associated with ITO including brittleness and lack of stability⁴, additionally it may also simplify device structure and fabrication process. 5% DMSO was added into the aqueous PEDOT:PSS solution before deposition and the sheet resistance of the modified PEDOT:PSS film was decreased by 3 orders of magnitude compared to that of a pristine one. Both the ITO-based standard and ITO-free flexible devices were fabricated. The *PCE* of the ITO-free device (2.30 %) is slightly higher than the standard device (1.92 %) even with a decrease in J_{SC} , and this is mainly due to a boost in the V_{OC} from 0.54 V for the ITO-based to 0.666 V for the ITO-free device. In order to have a better understanding of how the replacement of the anode junction affects the device performance, a light dependence study was carried out for intensities ranging from 0.34 – 2.01 sun. Fitting of the J_{SC} and V_{OC} to light intensity shows a higher bimolecular recombination rate in the flexible device than the standard one, which explains the trend in *FF* and *PCE* as a function of light intensity. The *FF* and *PCE* keep decreasing in the ITO-free device while in the ITO-based device they remain more stable after an initial drop as the light intensity increases. The decreasing trend in the two parameters indicates more unbalanced transport in the ITO-free OPVs and in turn a higher bimolecular recombination rate,

which can be the direct reason for the lower current density compared to the ITO-based standard device. The boost in V_{OC} for the flexible device can be caused by two reasons, structurally or electronically. The lower R_s extracted from the I-V curve indicates lower contact resistance in the flexible device compared to standard device and a higher R_{sh} indicates less pinhole defect, which could be the reason for the improvement of V_{OC} . However, the modification of the PEDOT:PSS work function as well as the anode conductivity difference can't be excluded.

7.3 Space-Charge effects in OPV's

In order to have a clearer view of how the anode transport property affects the device performance, more controlled set of experiments were designed⁵. ITO-free flexible devices were fabricated with two different thicknesses of PEDOT:PSS layer which gives a variation in anode transport properties. The device with a less conductive anode shows a slight decrease in J_{SC} , FF and PCE and a clear drop in V_{OC} from 0.645 V to 0.551 V. The fitting of the J_{SC} to light intensity indicates that the bound of SCLC has been reached in both devices, which means that the hole and electron extraction abilities are strongly unbalanced and highly concentrated space charge accumulates in the devices. While the V_{OC} for the device with higher anode conductivity shows an increasing trend to light intensity, the device with the lower anode conductivity experiences a decrease in V_{OC} immediately as the light intensity increases, which was rarely observed from past work published. A model involving the effect of the energy alignment at the contact as well as band bending caused by charge carriers in the bulk of the device was applied to fit the different trends for the response of V_{OC} to light intensity in the two devices. Fitting the

curve revealed that when the charge density in the anode increases to a certain amount, the V_{OC} response to light intensity can revert from increasing to decreasing. This critical point is depend on whether the potential increase from the increasing of the photogenerated charge densities can overcome the potential drop caused by the space charge accumulation. Upon analysis and fitting the experimental data the result is consistent with the anode conductivity variation designed into the experiment. The FF and PCE trends to light intensity are the same for both devices with the values for the device comprising a less conductive anode being slightly lower than the comparison device.

7.4 References

- ¹ X. Zhang, K.-S. Liao, S. D. Yambem, N. J. Alley, and S. A. Curran, *Synthetic Metals* **161**, 2798 (2012).
- ² S. D. Yambem, K.-S. Liao, N. J. Alley, and S. A. Curran, *Journal of Materials Chemistry* **22**, 6894 (2012).
- ³ E. Andreoli, X. Zhang, K.-S. Liao, and S. Curran, (Manuscript under preparation).
- ⁴ X. Zhang, K.-S. Liao, A. Haldar, N. J. Alley, and S. A. Curran, (Manuscript accepted by APL in June 2013).
- ⁵ X. Zhang, K.-S. Liao, and S. A. Curran, (Manuscript under preparation).